



MONASH University

**Influence of Binary Microstructures on Mechanical Properties of
Selective Laser Melted Ti-6Al- 4V Alloys**

Yue Zhao

Master of Research

A thesis submitted for the degree of *Master* at

Monash University in 2018

Department of Mechanical and Aerospace Engineering

Copyright notice

© The author (2018).

I certify that I have made all reasonable efforts to secure copyright permissions for third-party content included in this thesis and have not knowingly added copyright content to my work without the owner's permission.

Abstract

As a promising structural material for complex shape parts in medical and aerospace engineering, selective laser melted (SLM) Ti-6Al-4V has been studied widely on its properties and control of quality. Furthermore, microstructures, which can be tailored by altering processing parameters, will dominate material properties. Hence, in order to improve the material properties to meet some specific requirements of applications, the relationship of microstructures and properties is worth studying.

In this study, the influence of microstructures occurred in SLMed Ti64 alloys on mechanical properties was investigated. Simulation of various microstructures by finite element analysis (FEA) was carried out to predict the behavior of SLMed Ti64, and experimental tests were carried out to validate the predictions.

Among scanning strategies in SLM, cross-hatch scanning strategy has been commonly applied to lower material anisotropy. As consequence, a featured microstructure “chessboard” occurs in the cross-section perpendicular to the building direction. This pattern contains two types of microstructures of different martensite sizes. The microstructures and the geometry of the “chessboard” pattern determines the mechanical properties of the SLMed Ti64 at macroscopic scale.

The influence of the “chessboard” microstructures on the mechanical properties of the SLMed Ti64 was investigated using the representative volume element (RVE) established from the “chessboard” mesostructure. The finite element method was applied to predict the averaged Young’s modulus and yield strength of the RVE. A parametric study was conducted to understand the key parameters which form the RVE on the mechanical properties of the SLMed Ti64 at macroscopic scale. The yield strength of the material was predicted to be decided by several parameters of the mesostructure: the size and yield strength of the interfacial/matrix area and the hatch angle. On the other hand, initial characterization of binary microstructures was carried out by nanoindentation, in which Young’s modulus and hardness were measured to be very close in both areas. Microscopic characterization of the material provided the lamellar width which can explain the similarity by Hall-Petch effect.

Declaration

This thesis contains no material which has been accepted for the award of any other degree or diploma at any university or equivalent institution and that, to the best of my knowledge and belief, this thesis contains no material previously published or written by another person, except where due reference is made in the text of the thesis.

Signature:.....

Print Name:Yue Zhao.....

Date:28/September/2018.....

Publications during enrolment

Zhao, Y., Davies, C., Wu, X., Yan, W. (2017), 'Influence of "Chessboard" Microstructure on Mechanical Properties in Selective Laser Melted Ti-6Al-4V' Proceeding of 1st International Conference on Mineral Engineering and Materials Science, 978-0-6480147-7-5, 20th-28th November 2017, Sydney, Australia.

Zhao, Y., Kan, Q., Cao, S., Davies, C., Wu., X., Yan, W. (2018), 'Mechanical Properties of Binary Microstructures in Selective Laser Melted Ti-6Al-4V', to be submitted to Materials Express.

Acknowledgements

I will like to express my great thanks to my supervisors Wenyi Yan, Xinhua Wu and Chris Davies for their guidance throughout the project. Special thanks to Tom Jarvis and Sheng Cao from MCAM for their help on samples. Special thanks to Qianhua Kan providing nanoindentation instrument and instructions. Special thanks to Brandon Kakoschke offered his help. Special thanks to Xiya Fang, Renji pan from MCEM and provided training and assistance on SEM instrument operation. Thanks to all my group members.

Contents

Copyright notice.....	II
Abstract.....	III
Declaration.....	IV
Publications during enrolment	V
Acknowledgements.....	VI
List of Figures.....	IX
List of Tables	XIV
1.Introduction.....	1
2. Literature Review.....	4
2.1. Additive Manufacturing.....	4
2.2. Selective Laser Melting	6
2.3. Ti-6Al-4V alloys.....	7
2.3.1. Crystal Lattice Structure	7
2.3.2. Elastic Properties.....	8
2.3.3. Phase Transformation	9
2.4. Microstructures of Ti alloys.....	13
2.4.1. Classification of General Microstructures in $\alpha+\beta$ Ti alloys.....	13
2.4.2. Typical Microstructures and Mechanical Properties of Selective Laser Melted Ti-6Al-4V.....	16
2.5. Scanning Strategies and Microstructures	26
2.5.1. Common Scanning Strategies	26
2.5.2. Influence of Scanning Strategy on Microstructures.....	28
2.5.3. Generation of Mesostructures	30
2.6. Finite Element Analysis	33
2.7. Nanoindentation.....	35
2.8. Summary	37
3. Characteristics of Microstructures in Binary Areas.....	38
3.1 Introduction.....	38
3.2 Methodology and Materials	39
3.3 Results and Discussion	40
3.4 Summary.....	46
4. 2D Finite Element Analysis.....	47
4.1 Introduction.....	47

4.2 Methodology and Materials	47
4.3 Results and Discussion	54
4.3.2 Influence of Matrix Area.....	57
4.3.3. Influence of Material Strength	62
4.3.4 Influence of Hatch Angles	65
4.4 Summary	69
5.Binary Microstructures Properties Measurement	70
5.1 Introduction.....	70
5.2 Methodology and Materials	71
5.2.1 Sample preparation	71
5.2.2 Microscopy characterisation	71
5.2.3 Nanoindentation test	71
5.2.4 Microhardness test	74
5.2.5 Nanoindents Positions.....	74
5.3 Modulus and Hardness Results	77
5.4 Microhardness.....	81
5.5 Influence of Lamellar Width, Indentation Depth and Residual Stress.....	82
5.5.1 Lamellar width effect	82
5.5.2 Indention depth effect	83
5.5.3 Residual stress effect.....	84
5.6 Summary	85
6.Conclusion	86
References.....	88

List of Figures

Figure 2-1 Summary of metal additive manufacturing processes, along with their commercial machine supplier names.....	5
Figure 2-2 schematic flow chart of SLM processing.....	5
Figure 2-4 Unit cell of a) alpha phase and b) beta phase.	7
Figure 2-5 Modulus of elasticity E of α titanium single crystals as a function of declination angle γ	8
Figure 2-6 Slip planes and slip directions in the hexagonal α phase.....	8
Figure 2-7 “Acicular” martensite in Ti-6Al-4V quenched from the β phase field: (a) Light Microscopy (b) TEM.....	10
Figure 2-8 Schematical representation of the crystallographic relationship between α plates and β	11
Figure 2-9 Schematic processing route for lamellar microstructures of $\alpha+\beta$ titanium alloys.	12
Figure 2-9 Schematic processing route for lamellar microstructures of $\alpha+\beta$ titanium alloys..	12
Figure 2-11 Schematic processing route for bi-modal microstructures of $\alpha+\beta$ titanium alloys.....	13
Figure 2-12 Bi-modal microstructures of the IMI 834 alloy cooled differently from the β phase field in step I of the processing route, Light Microscopy: (a) Bi-modal 1, slow cooling rate (b) Bi-modal 2, fast cooling rate...15	15
Figure 2-13 Fine grained, fully equiaxed microstructure of the Ti-6Al-4V alloy recrystallized at 800°C: (a) LM (b) TEM.....	15
Figure 2-14 (a) Optical micrograph from the frontal xz-plane, (b) lateral yz-plane, and (c) horizontal xy-plane of an as-deposited cubic component. Prior β columnar grain boundaries and α' lath appear in the microstructure. The vector g^* shows the β grain growth direction.....	15
Figure 2-15 Microstructures of the supertransus solution treatment 1323 K (1050 °C/1 h WQ): (a) optical micrograph showing the grain morphology and (b) SEM micrograph in the SE mode showing the α' needles.....	17

Figure 2-16 Microstructures of the subtransus solution treatment 1223 K (950°C/1 h WQ): (a) optical micrograph showing the grain morphology and (b) SEM micrograph in the SE mode showing the α , α' and β phases.....	18
Figure 2-17 CT scan of a 3 mm diameter cylinder showing porosity (blue coloured) and distribution, where a) HIP, b) as-built. a) After the HIP process the porosity was below the resolution limit of 3 μ m. c) is enlargement of b) to show the pore orientation and distribution.....	19
Figure 2-18 (a) EBSD α' orientation map and the corresponding color scheme of a specimen taken from the frontal xz-plane of an as-deposited component (the black arrow indicates the building direction); (b) corresponding (0001) α' and (11 20) α' contour pole figures; (c) orientation map of the reconstructed β phase. (d) the corresponding (110), (111), (100) contour pole figures; (e) (0001) α' and (1120) α' contour pole figures of the α' data set (f) (110), (111), (100) contour pole figures of the corresponding rotated β phase.....	20
Figure 2-19 (a) α' and corresponding reconstructed β orientation maps from the horizontal xy-plane; (b) and (c) discrete pole figures of the α' variants and their parent β grain.....	22
Figure 2-20 Three different scanning strategies, namely identical scanned layers using zigzag (left) or unidirectional scan vectors (centre) and the cross-hatching technique using the zigzag scan vectors (right)....	23
Figure 2-21 The 'islands' scanning strategy on the Concept Laser M2 Cusing SLM system, and the typical chessboard morphology on the surface of a Ti-64 rectangular build.....	24
Figure 2-22 Overview of the scanning strategy used for the different samples. The building (BD), scanning (SD) and transverse direction (TD) are indicated.....	24
Figure 2-23 SEM images of SLMed Ti-6Al-4V cuboid samples on XOY section; (b) and (c) are the magnifications of the areas indicated by the white boxes in (a).....	24
Figure 2-24 From left to right: top-view microstructures of unidirectional scanning strategy, cross-hatching scanning strategy, zigzag scanning strategy.....	25
Figure 2-25 Optical microscopy images of the crack, highlighting the preferential path along the prior β grain boundaries a) Oscillation deposition strategy b) Oscillation deposition strategy higher magnification c) Parallel deposition strategy d) Grade 23 wire.....	26
Figure 2-26 a) 3D representative microstructure of Ti64 samples. b) Schematic representation of the scan rotation of 90° between each successive layer, where B represents the plane normal to building direction, S	

represents the plane parallel to building direction, as shown. c) Microstructure of B-plane. d) Microstructure of S-plane.....	27
Figure 2-27 (a) Representative temperature contour and (b) melt pool geometry.....	28
Figure 2-28 Finite element model of periodic polycrystal.....	29
Figure 2-29 Comparison of model simulation of stress–strain curve with experimental results for Ti–6Al–4V at room temperature, for the uniaxial strain history with constant strain rate and with no hold periods.....	29
Figure 2-30 A schematic representation of a section through an indentation.....	31
Figure 2-31 A schematic representation of load versus indenter displacement showing quantities used in the analysis as well as a graphical interpretation of the contact depth.....	31
Figure 3-1 Optical microstructures of SLM (a) and EBM (b) samples produced using optimum process parameters. Note the presence of α phase (grain boundary α) on prior β grain boundaries in (b)	33
Figure 3-2 Optical microscopy of lateral view of SLMed Ti64.....	35
Figure 3-3 BSE images of lateral view of SLMed Ti64: 1) overall view, 2) near bottom and 3) near top. Prior β grain highlighted in red contour shape and, building direction indicated by black arrow.....	36
Figure 3-4 EBSD image and pole figure of top view of SLMed Ti64.....	37
Figure 3-5 Sketch of overlaps of melt pools in the direction parallel to building direction.....	38
Figure 3-6 EBSD map of 3D-view of SLMed Ti64 (elongated prior β grains contained).....	39
Figure 4-1 Schematic sketch of idealized periodic microstructures and RVE for FEA.....	41
Figure 4-2 BSE image of 67°hatch angle scanned (left) and simplified outline (right).....	41
Figure 4-3 Trapezoidal and parallelogram pattern "chessboard" RVE generation.....	42
Figure 4-4 Example deformed RVE in FEA.....	43
Figure 4-5 Example deformed RVE under x (left) and y (right) direction loading.....	45
Figure 4-6 RVE's Young's modulus changes with interface thickness b (hatch angle=90°).....	46
Figure 4-7 RVE's yield strength changes with interface thickness b (hatch angle =90°).....	47

Figure 4-8 RVE's yield strength changes with interface thickness b under x-axis loading (Average RVE angle =75.458°).....	47
Figure 4-9 RVE's yield strength changes with interface thickness b under y-axis loading (Average RVE angle =75.458°).....	48
Figure 4-10 RVE's Young's modulus E changes with matrix side length a (hatch angle=90°).....	49
Figure 4-11 RVE's yield strength changes with matrix side length a (hatch angle =90°)....	50
Figure 4-12 Yield stress for alternating matrix width under x-axis loading (Average RVE angle =75.458°).....	50
Figure 4-13 Yield stress for alternating matrix width under y-axis loading (Average RVE angle =75.458°)....	50
Figure 4-14 Yield strength for alternating matrix length under x-axis loading (Average RVE angle =75.458°)....	51
Figure 4-15 Yield strength for alternating matrix length under y-axis loading (Average RVE angle =75.458°)..	51
Figure 4-16 RVE's yield Strength of composites changes with yield strength of Material B when a=150μm, b=18μm.....	53
Figure 4-17 RVE's yield strength of composites changes with yield strength of Material A when a=150μm, b=18μm.....	53
Figure 4-18 RVE's yield strength of composites changes with yield strength of Material B when a=150μm, b=55μm.....	54
Figure 4-19 RVE's yield strength of composites changes with yield strength of Material A when a=150μm, b=55μm.....	54
Figure 4-20 Min. angle 57.604° RVE model with x-axis (left) and y-axis (right) loading.....	55
Figure 4-21 Max. angle 88.21° RVE model with x-axis (left) and y-axis (right) loading.....	56
Figure 4-22 Yield strength for changing hatch angle with y-axis loading.....	57
Figure 4-23 Yield strength for changing hatch angle with x-axis loading.....	58
Figure 5-1 Load-Indentation depth curve in Oliver-Pharr method.....	61
Figure 5-2 EBSD IPF-X map of 1000 nm nanoindentation on vertical sample surface (Interfacial area indicated by arrow) Magnified images of indentation areas are indicated by red arrows. (phase composition: Ti-hex 98%).....	64

Figure 5-3 EBSD IPF-X map of 1000 nm nanoindentation on horizontal sample surface (Interfacial area is indicated right above and matrix area is shown right below) Magnified images of indentation areas are indicated by red arrows. (phase composition: Ti-hex 98%).....64

Figure 5-4 EBSD IPF-X map of 200 nm nanoindentation on horizontal sample surface in interfacial (a) and matrix (b) area; (c) legend for all EBSD IPF-X map. (phase composition: Ti-hex 95%).....64

Figure 5-5 EBSD image of EBSD IPF-X map of 1000 nm nanoindentation on horizontal stress relieved sample surface. (Phase composition: Ti-hex 98%).....65

Figure 5-6 EBSD IPF-X map of 1000 nm nanoindentation on stress relieved vertical sample surface. (phase composition: Ti-hex 97%).....65

Figure 5-7 hardness-displacement curve for two indents in different area.....68

List of Tables

Table 2-1 Slip systems in the hexagonal α phase.....	9
Table 2-2 Tensile results for SLM-produced and EBM-produced Ti64 alloy samples.	14
Table 2-3 Summary of different procedures for rapid manufacturing of Ti-6Al-4V.....	14
Table 2-4 Influence of heat treatment conditions on Ultimate tensile strength, 0.2% offset yield strength and elongation at failure.....	19
Table 4-1 Parameters range in 90°hatch scanned model.....	44
Table 4-2 Parameters range in 67°hatch scanned model.....	44
Table 4-3 Yield stress values for change in interface thickness.....	48
Table 4-4 Young's modulus values for change in interface thickness.....	48
Table 4-5 Yield strength values due to change in width of matrix.....	52
Table 4-6 Young's modulus values due to change in width of matrix.....	53
Table 4-7 Yield strength values due to change in length of matrix.....	53
Table 4-8 Young's modulus values due to change in length of matrix.....	53
Table 4-8 Yield strength values for change in angle.....	57
Table 4-9 Young's modulus values for change in angle.....	57
Table 5-1 Elastic modulus calculated from nanoindentation using Olive-Pharr model (AB: as-built; SR: stress relieved).....	66
Table 5-2 Hardness calculated from nanoindentation using Olive-Pharr model (AB: as-built; SR: stress relieved).....	67
Table 5-3 Comparison of average microhardness at different plane with/without stress relief treatment.....	69

1. Introduction

Additive manufactured metallic materials have been widely applied in various industries for its capability for complex structures [1]. Among those, titanium alloy is one kind of promising commercial material because it is lightweight and economical for automotive or aviation engineering [2], also good biocompatibility in human body for printed implants [3, 4].

Different from conventionally processed material such as by casting or forging, SLMed Ti-6Al-4V has better performance resulting from a more rapid process with almost 100% yield, high flexibility in geometrical details of parts as well as in production batch. SLMed Ti64 can be made into any shape without the use of any moulds which are generally expensive and hard to build. As a consequence, some advanced engineering applies some important parts made of SLMed Ti64 such as turbines, engines [5].

However, the rapid heating with laser can result in local high temperature and uneven heat conduction history among the material; hence, the microstructure will get much more inhomogeneous than conventional built parts. This results in some drawbacks in mechanical properties such as anisotropy and low fatigue resistance especially in building direction [6, 7]. Correspondingly, researchers have conducted to a great number of works. Effort has been put into studies such as the relationship of microstructures and mechanical properties in SLMed Ti64, the influence of processing parameters and post-treatment on microstructures and mechanical performance, and how to tailor the microstructures by altering processing parameters as well as post-treatments [8, 9].

Microstructure has been regarded as the key to improvement of SLMed Ti64. One of the microstructural findings in SLMed Ti64 is the featured microstructures, as a result of laser scanning, which is called the binary microstructures as described in this study. To be specific, under the commonly applied cross-hatch scanning strategy, the microstructures occur periodically

and appear in a “chessboard” pattern accordingly [10]. The term “binary” refers to the different microstructural morphology from two kinds of area within the periodic structure. The microstructures were found as a typical phenomenon in SLMed Ti64 [10, 11, 12]. However, there is a lack of either quantified study to evaluate their influence on performance of SLMed Ti64, or detailed characterization of the binary microstructures.

It is important for this study to specify the binary microstructures, achieve quantified relationship between microstructure and mechanical properties, and make it possible to tailor the microstructure of SLMed Ti64 to meet the industrial requirements. Overall, this master study will focus on distinguishing the properties of the featured binary microstructures of SLMed Ti64 and investigating the influence of the binary microstructures on mechanical properties of SLMed Ti64.

In order to determine the influence of the binary microstructures on the SLMed Ti64, this study uses cross-hatch scanned SLMed Ti64. With morphology characterised, a grid-like mesostructure can be observed where the matrix area inner grid of the binary microstructures and the interfacial area among them are distinguished. Furthermore, their morphological and mechanical properties are measured and quantified. In addition, the influence of the “chessboard” pattern as well as the binary microstructures on the material is predicted and quantified using simulation. To achieve this, following objectives are conducted.

- To characterize the microstructures in “chessboard” pattern, and to quantify the grain size (laminar width) of the microstructures.
- To understand the influence of binary microstructure on the mechanical properties including Young’s modulus and yield strength of SLMed 64 by using finite element method and use

Representative Volume Elements (RVE) to simulate the periodic mesostructured: “chessboard”.

- To evaluate mechanical properties including Young’s modulus and yield strength of SLMed Ti64 by using finite elements analysis (FEA). To understand the influence of different SLM scanning strategies, hatch distance and local mechanical properties of interfacial/matrix area in the perspective of microstructures on the overall performance of the material.
- To characterize the mechanical properties such as Youngs modulus and hardness of the interfacial area and matrix area within the binary microstructures by using nanoindentation. Furthermore, the yield strength will also be derived using Hall-Petch equation.

The layout of the whole study is in the order of objectives planned. Chapter 1 provides the background to this study. Chapter 2 reviews relevant studies in the field. The study of objectives as well as the methodology is described sequentially in following chapters. This study is divided into 3 stages which are outlined in Chapter 3, 4, 5. Chapter 3 notes the characterisation of the binary microstructures morphology using electronic microscopy. Chapter 4 records the simulation of the “chessboard” mesostructure and the influence on material’s mechanical properties. Chapter 5 contains the characterisation of the local mechanical properties of the interfacial/matrix area such as nanohardness and Young’s modulus using nanoindentation. Corresponding results analysis and discussion are also included in each chapter. At last, the conclusion of key findings lies in the Chapter 6.

2. Literature Review

2.1. Additive Manufacturing

The general idea of additive manufacturing is that a component model, which is generated by three-dimensional Computer-Aided Design, will be directly built without any mould-involved process planning needed. Complex three-dimensional parts hence can be fabricated directly via simplified process by using Additive Manufacturing (AM) instead of a detailed and complicated means about tools or procedures in order to complete all features as required [13].

The present production of metals can benefit from various advantages of AM. Firstly the time of the whole processing as well as the interpretation of design can be saved significantly. Secondly, seamless products from AM processes will be seen in terms of the increase of quality of parts and reduction of steps. Molding process as well as time can be saved, consequently, the cost of energy and raw material are reduced in AM. Hence, AM is regarded as a highly cost-effective, versatile and streamlined way to fabricate a variety of parts [13].

There are a number of available AMs on metal processing, which can be classified by heating sources, such as laser, electron beam and arc, or differentiated by materials input: either powder or wire [14] . Fig. 2-1 lists some current major AM techniques with heating source such as selective laser melting (SLM), direct metal laser melting (DMLM), and direct metal deposition (DMD) in

two major categories of powder bed fusion and directed energy deposition.

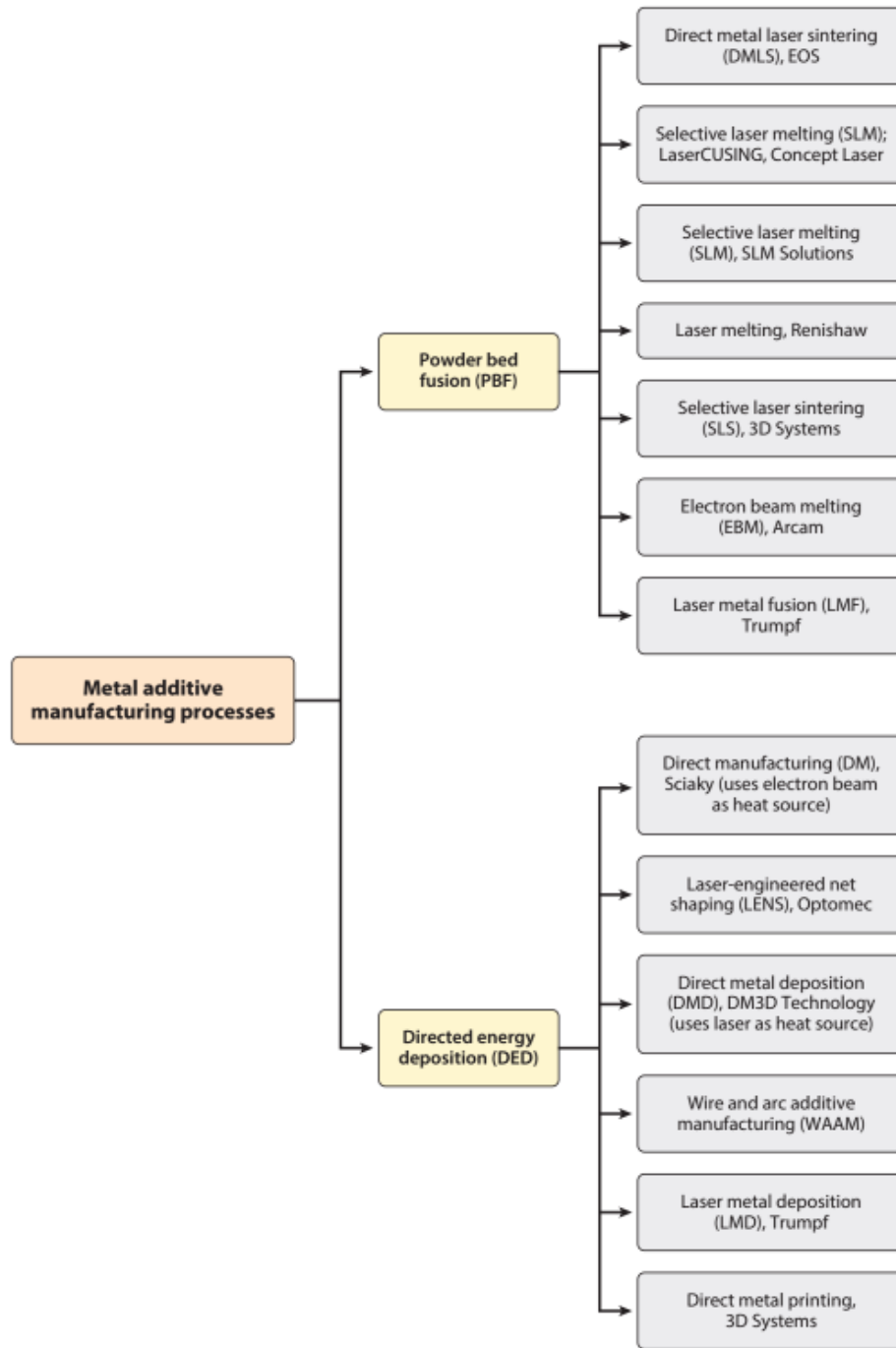


Figure 2-1 Summary of metal additive manufacturing processes, along with their commercial machine supplier names [14].

2.2. Selective Laser Melting

As one of the most employed AM technologies on industrial alloys such as titanium, steel and aluminum, selective laser melting has been developed and applied in some industries for single or small batch fabrication such as dental replacement [15]. In order to advance applications of SLM in other industries such as space industry, the product quality should be maintained as required; furthermore, the quality needs to be controllable, and the output matches prediction.

As illustrated in Fig.2-2, the sequence of SLM process can be divided into several steps. First of all, the 3D-CAD model will be separated into layers for analysis in computer and then it will be transferred to the machine. Next, the raw material (atomized metal) will be applied in layer deposited on substrate. Laser beam will subsequently scan powder and realise the geometrical characteristics in this layer within the inert atmosphere. Then, the repetition for each layer building will be started again by lowering the platform for one layer thickness, and be circulated till all layers have been completed [5].

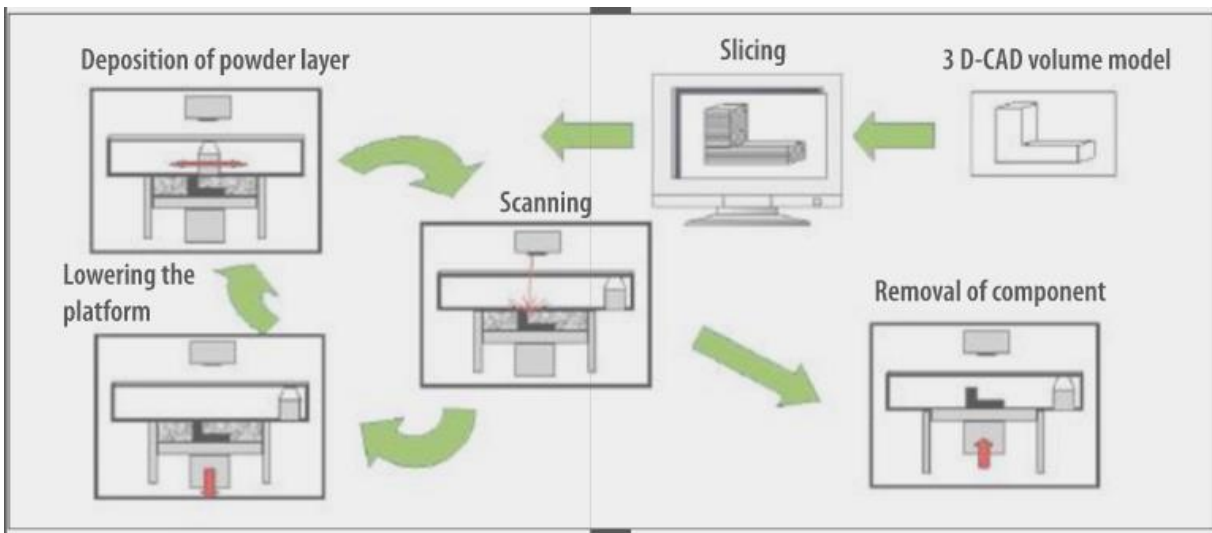


Figure 2-2 schematic flow chart of SLM processing [5].

During the laser scanning process, the scanning strategy is an essential factor which will dominate

the thermal history of the process; as a consequence, the microstructures and properties such as density and residual stress will be affected. It has been proven that alternating scanning strategy can increase the density of product in that a relative density of 99.9% was reached in Thijs's study [11].

2.3. Ti-6Al-4V alloys

As one of the mostly commercially applied titanium alloys, Ti-6Al-4V (Ti64) can be processed by a wide range of methods such as forging, casting, rolling, and be applied for corresponding uses such as medical implants or aircraft engine.

2.3.1. Crystal Lattice Structure

For most titanium alloys, there are usually two kinds of possible phases: alpha (α) and beta (β). In pure titanium, the allotropic transformation temperature between these two phases is about 882°C. Thereinto, β phase has got a body-centred cubic (BCC) crystal structure which is stable at high temperatures while α phase is hexagonal close-packed (HCP) crystal structure which is stable at low temperatures [16]. The transus temperature of Ti alloy depends on alloy elements and their contents, specifically in Ti64, and the transus temperature is reported around 980°C [17].

Table 2-1 Thermal properties of annealed Ti-6Al-4V [17]

THERMAL PROPERTIES			
MELTING POINT	1.61E+03	-	1.66E+03 °C
MAXIMUM SERVICE TEMPERATURE	350	-	420 °C
MINIMUM SERVICE TEMPERATURE	-273		°C
THERMAL CONDUCTIVITY	7.1	-	7.3 W/m.°C
SPECIFIC HEAT CAPACITY	528	-	548 J/kg.°C
THERMAL EXPANSION COEFFICIENT	8.7	-	9.1 μ strain/°C
LATENT HEAT OF FUSION	360	-	370 kJ/kg

There is a great structural difference between α phase and β phase; hence, their properties are

different. Generally, α phase is higher in strength while β phase is more ductile. As illustrated in Fig. 2-4, α phase crystal cube in pure Ti under room temperature is a typical HCP structure with lattice parameters $a=0.295$ nm and $c=0.468$ nm. The consequent c/a ratio of pure titanium is 1.587. As marked as dark planes in Fig.2-4 (a), three kinds of most densely packed planes are basal plane (0002), three pyramidal planes (10-10) and six pyramidal planes (10-1-1). Also, along a_1 , a_2 and a_3 axes are close-packed directions of $\langle 11\bar{2}0 \rangle$. On the other hand, the unit cell of β phase is a BCC structure, as shown in Fig.2-4 (b), with (110) planes as most densely packed planes when close-packed directions are four $\langle 111 \rangle$ directions, and the lattice parameter $a=0.332$ nm in pure β at 900°C .

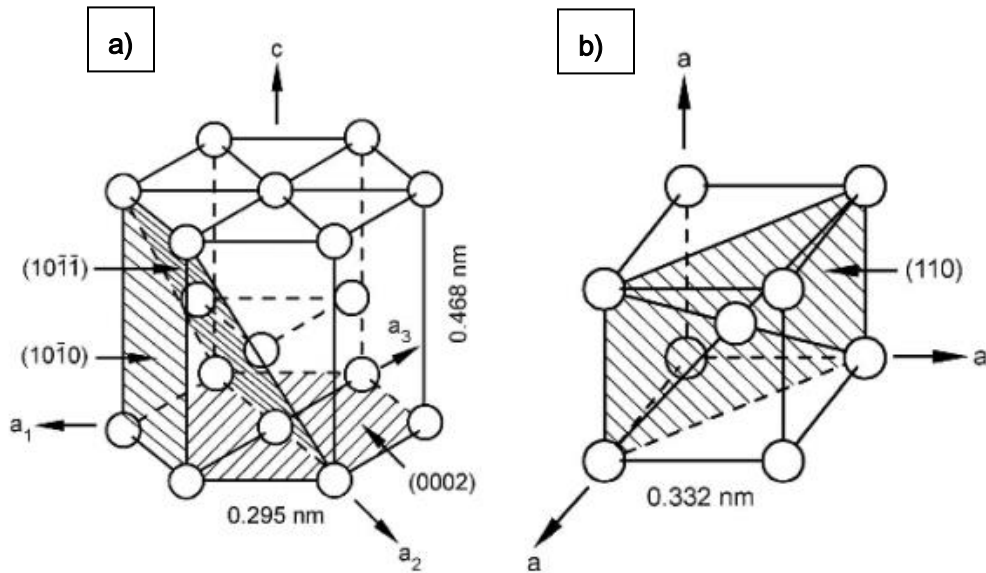


Figure 2-4 Unit cell of a) alpha phase and b) beta phase [16].

2.3.2. Elastic Properties

The anisotropy of HCP α dominates anisotropic properties in titanium alloys. To be specific, the elastic modulus varies between 145 GPa and 100 GPa in pure single crystal α at room temperature as a function of the stress angle from c-axis of cell, as shown in Fig.2-5. Besides, temperature is

another factor which will affect elastic properties of titanium alloys [18].

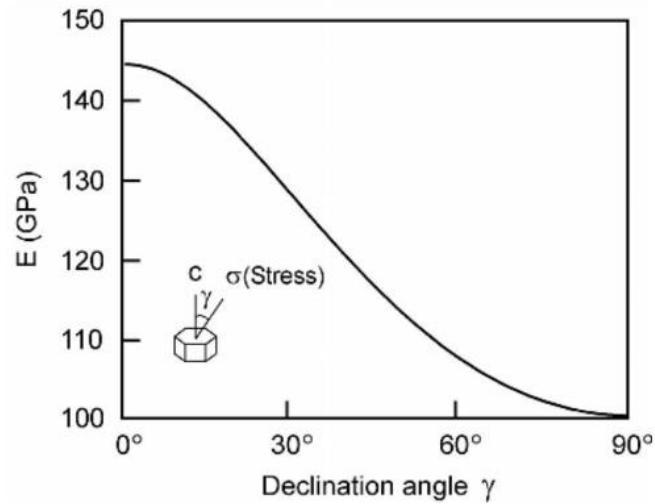


Figure 2-5 Modulus of elasticity E of α titanium single crystals as a function of declination angle γ [18].

2.3.3. Phase Transformation

2.3.3.1. Slip systems

Variants of slip planes and slip directions are illustrated in the Fig. 2-6 and their 12 combined slip systems are listed in table 2-1. The primary slip directions are three $\langle 11-20 \rangle$ close-packed directions; when the slip planes are (0002) , three of $\{10-10\}$, six of $\{10-11\}$.

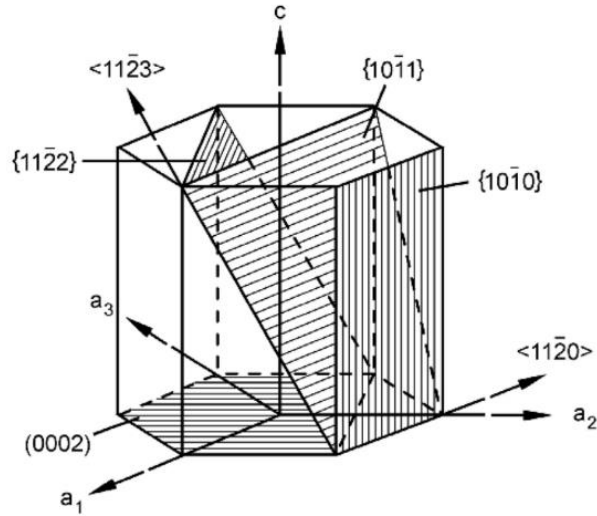


Figure 2-6 Slip planes and slip directions in the hexagonal α phase [19, 20].

Table 2-1 Slip systems in the hexagonal α phase [19, 20]

Slip system type	Burgers Vector type	Slip direction	Slip plane	Num. of slip systems	
				Total	Independent
1	\vec{a}	$\langle 11-20 \rangle$	(0002)	3	2
2	\vec{a}	$\langle 11-20 \rangle$	{10-10}	3	2
3	\vec{a}	$\langle 11-20 \rangle$	{10-11}	6	4
4	$\vec{c} + \vec{a}$	$\langle 11-23 \rangle$	{11-22}	6	5

In fact, the slip systems have only four types as Type 1 and 2 listed above make the shape change to be the same as Type 3. Therefore, since assumed von Mises criterion requires at least five independent slip systems for a homogeneous plastic deformation in polycrystals, one of the slip systems with a non-basal Burgers vector should be activated, both the \vec{c} type with the slip direction [0001] or the $\vec{c} + \vec{a}$ type with the slip direction $\langle 11-23 \rangle$. According to possible slip

planes from the dislocations with $\vec{c} + \vec{a}$ Burgers vectors, the slip planes {10-10} cannot be activated since the stress direction is parallel to them. What's more, other possible slip planes {11-22} are closer to higher Schmidt factor 45° than {10-11} as illustrated in Fig.2-6. To balance, the most likely slip system in α phase with non-basal Burgers vector should be Type 4 if the critical resolved shear stresses (CRSS) are the same for each slip plane. The absolute CRSS values rely on alloy elements and temperatures. In β phase, the slip systems are {110}, {112} and {123} planes with Burgers vector $\langle 111 \rangle$.

2.3.3.2. Martensite Transformation (non-diffusion)

There is crystallographic orientation relationship between two phases which is called Burgers relationship:

$$(110)\beta \parallel (0002)\alpha;$$

$$[1-11]\beta \parallel [11-20]\alpha$$

According to this, one bcc β crystal can have 12 possible HCP α variants.

Transformation without enough time for alloy atom diffusion will result in martensite formation, i.e. a bcc structure microscopically homogeneously transforms to a hcp lattice over given volume by cooperative atoms shear type movement. The shear systems which are activated to carry out the transformation are: $[111]\beta$ $(11-2)\beta$ and $[111]\beta$ $(-101)\beta$; or in HCP: $[2-1-13]\alpha$ $(-2112)\alpha$ and $[2-1-13]\alpha$ $(-1011)\alpha$. In most alloys with high solute content and low martensitic transformation temperature, acicular grains are the normal shape of formed martensite [21].

As illustrated in Fig. 2-7, acicular martensite is gathered up by compact α plates, in which each has got an individual variant in Burgers relationship. Normally, martensite is an unstable metaphase, which has got high content of dislocations. Since hexagonal martensite α' is supersaturated in β stabilizer element, when temperature is heated upon transus like during annealing, martensite will decompose to $\alpha+\beta$, nucleating β phase at dislocations or grain boundaries.

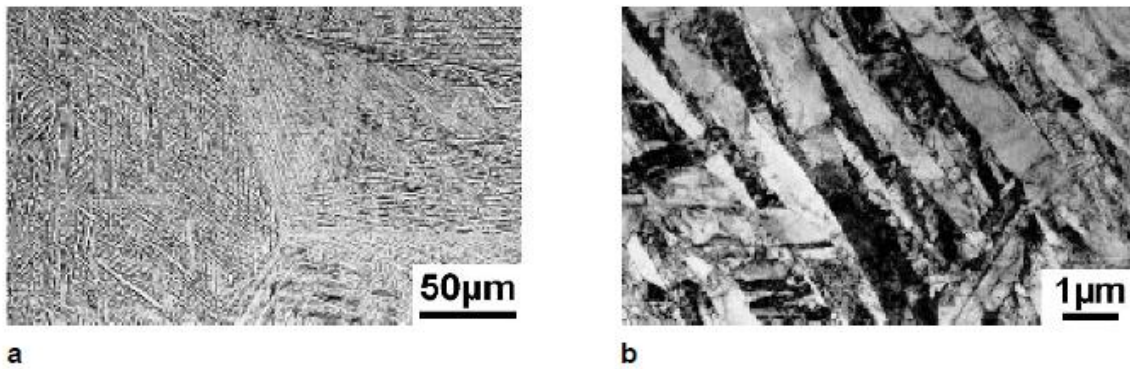


Figure 2-7 “Acicular” martensite in Ti-6Al-4V quenched from the β phase field: (a) Light Microscopy (b) TEM [16]

2.3.3.3. Diffusional Phase Transformation

If the cooling rate from β phase region to $\alpha+\beta$ phase region is low enough to allow alloy atoms diffusion, there will be α grains nucleating preferentially at grain boundaries; hence, continuous α layer will form along β grain boundaries. After nucleation of α at interfaces or grain boundaries, α plates can continuously grow into β grains as parallel colony within the same Burgers variant. This process and corresponding α and β relationship in crystallography is described in Fig. 2-8. The growth of colonies will not stop till they meet other colonies from different boundaries.

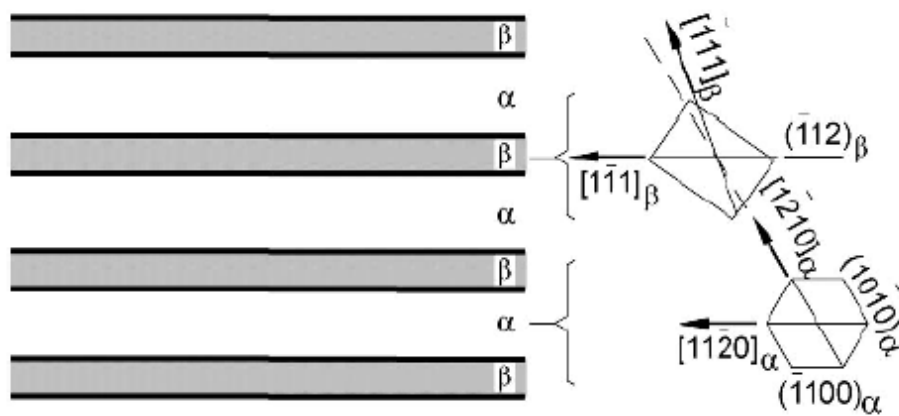


Figure 2-8 Schematical representation of the crystallographic relationship between α plates and β [16].

2.4. Microstructures of Ti alloys

2.4.1. Classification of General Microstructures in $\alpha+\beta$ Ti alloys

2.4.1.1. Fully Lamellar Microstructures

Annealing treatment at β phase which will contain recrystallization in β can result in lamellar $\alpha+\beta$ microstructure. As Fig. 2-9 illustrates, recrystallization will follow the deformation process such as forging, rolling in β temperature or $\alpha+\beta$ temperature region. The temperature of recrystallization treatment is important to be controlled above β temperature but low enough to avoid coarse grains. Fig. 2-10 shows the coarse grains and fine grains under different temperature treatments. Usually, β grain size of this fully lamellar microstructures will be controlled to about 600 μm . It is the cooling rate in recrystallization that will decide the lamellar microstructure characteristics such as the α plates size, colony size, layer thickness, as shown in Figure 2-10.

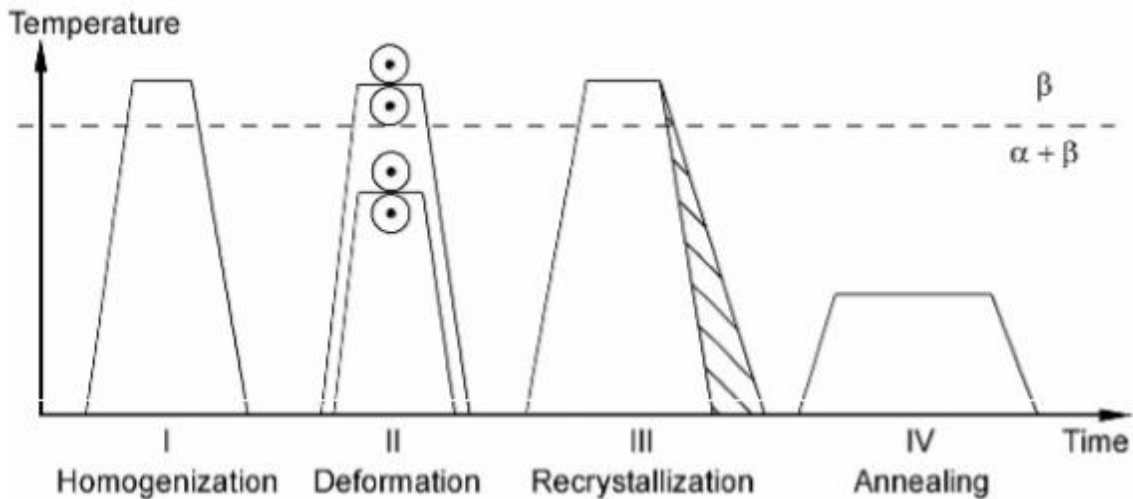


Figure 2-9 Schematic processing route for lamellar microstructures of $\alpha+\beta$ titanium alloys [22].

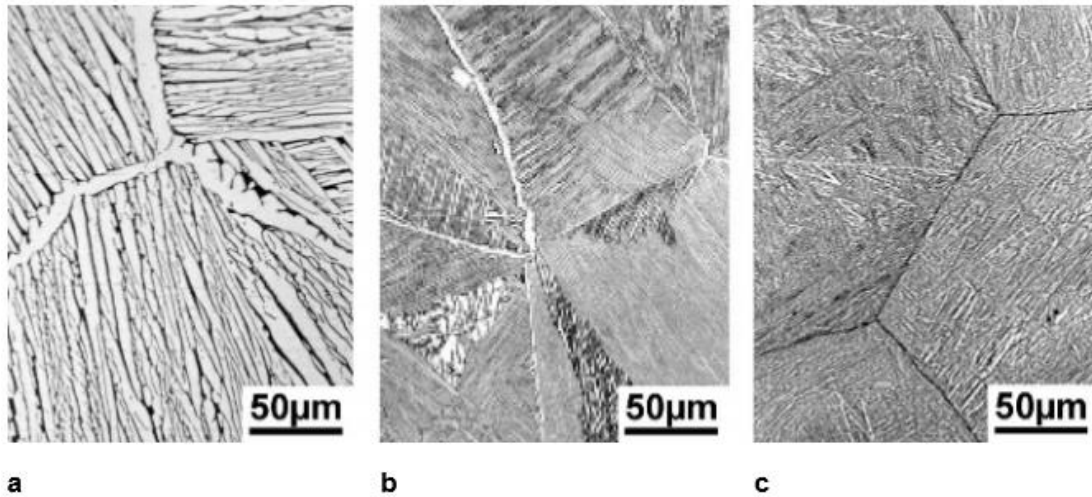


Figure 2-10 Effect of cooling rate from the β phase field on lamellar microstructures, Ti-6242, Light Microscopy: (a) $1^{\circ}\text{C}/\text{min}$ (b) $100^{\circ}\text{C}/\text{min}$ (c) $8000^{\circ}\text{C}/\text{min}$ [16].

2.4.1.2. Bi-Modal Microstructures

The temperature for the last three processes to obtain bi-modal microstructures should be set lower than β phase region as illustrated in Fig. 2-11. The cooling rate in step I homogenization is of great importance since α lamella thickness depends on it. In step II, the deformation will result in texture. Similarly, the temperature for recrystallization and cooling rate will influence β grain size and width of α lamella as shown in Fig. 2-12.

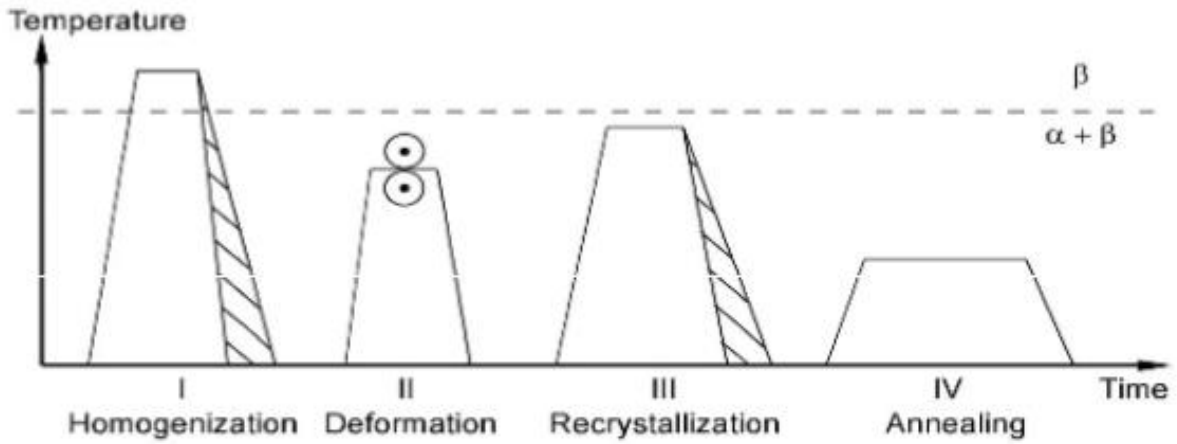


Figure 2-11 Schematic processing route for bi-modal microstructures of $\alpha + \beta$ titanium alloys [23].

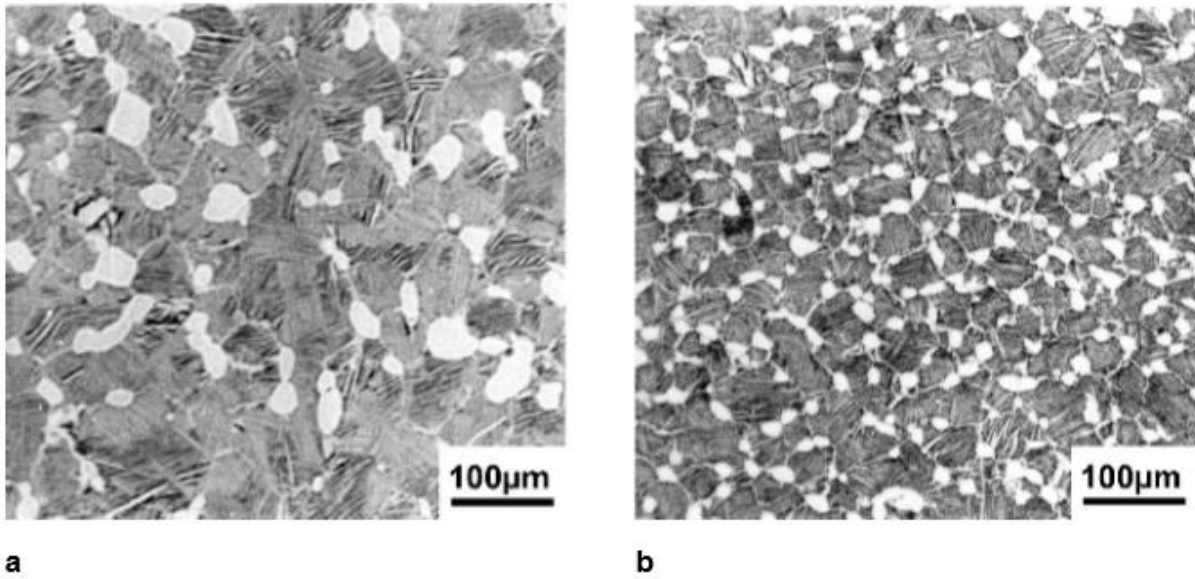


Figure 2-12 Bi-modal microstructures of the IMI 834 alloy cooled differently from the β phase field in step I of the processing route, Light Microscopy: (a) Bi-modal 1, slow cooling rate (b) Bi-modal 2, fast cooling rate [23].

2.4.1.3. Fully Equiaxed Microstructures

To achieve fully equiaxed microstructures as shown in Fig. 2-13, the process is similar to what produces bi-modal microstructures, and the low cooling rate in recrystallization will cause no lamellar α to form in β grains. Besides, low recrystallization temperature can be applied to make equilibrium α volume fraction high enough to nucleate fully equiaxed microstructures from a deformed structure.

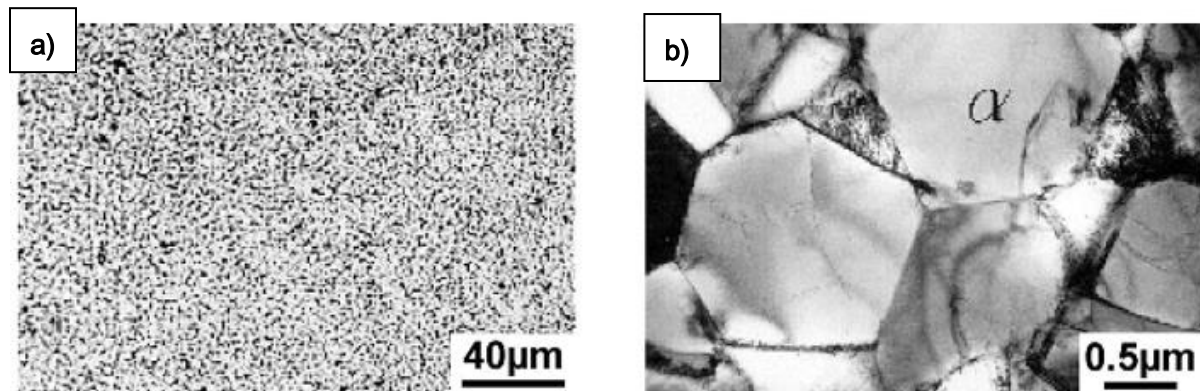


Figure 2-13 Fine grained, fully equiaxed microstructure of the Ti-6Al-4V alloy recrystallized at 800°C: (a) LM (b) TEM [16].

2.4.2. Typical Microstructures and Mechanical Properties of Selective Laser Melted Ti-6Al-4V

2.4.2.1. As-fabricated Part

Above β transus (about 980°C [9]), Ti64 will fully transform to β phase and when temperature drops into $\alpha+\beta$ region it will turn to $\alpha+\beta$ mixture. The β phase volume fraction will depend on the cooling rate from β phase region [12]. Due to rapid cooling rate in selective laser melting, martensites usually produce strong texture in prior β grains covering the whole part. Prior β grains tend to form columnar shape, since SLM will remelt the top part for each new deposited layer processing, then across deposited layers, β grains will epitaxially grow without nucleation barrier

for solidification [24]. As illustrated in Fig. 2-14 (a), acicular martensite α' take up the whole part and only grain boundaries of prior β grain remain after the temperature drops. Since Ti64 will solidify in the β phase region and heat will mostly conduct vertically away, the prior β grain boundaries can remain. The side profile micrograph shows that the columnar β grains tend to elongate along building direction of the part [25].

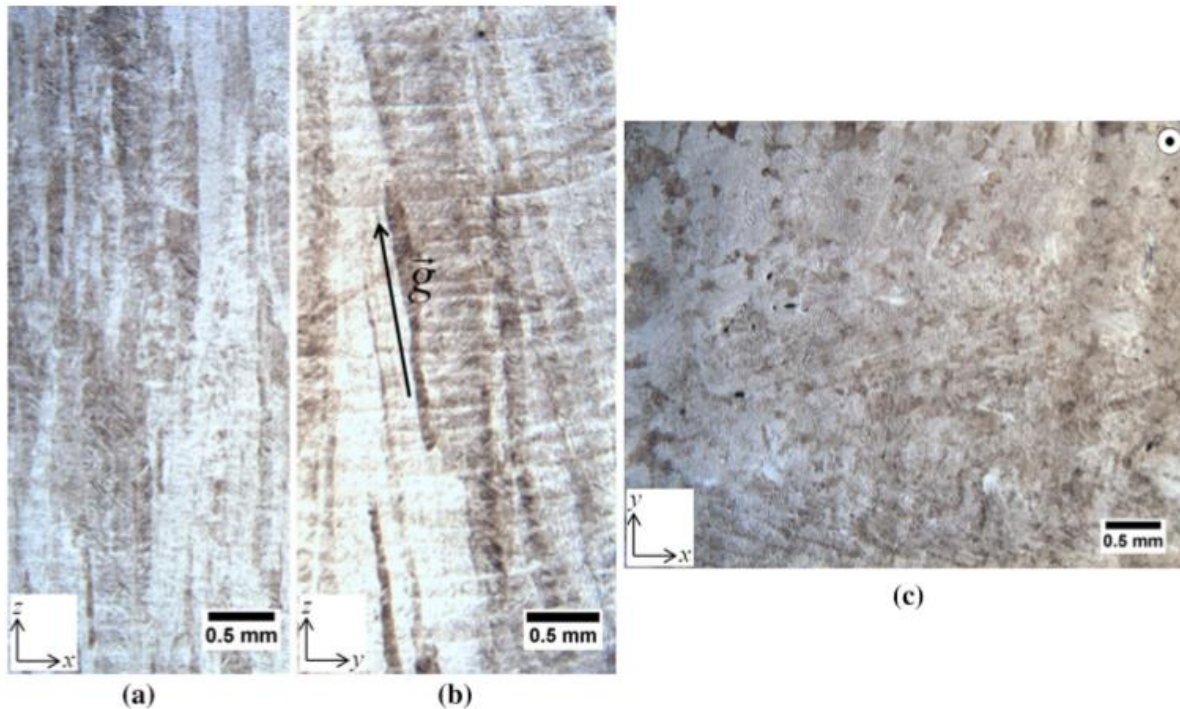


Figure 2-14 (a) Optical micrograph from the frontal xz-plane, (b) lateral yz-plane, and (c) horizontal xy-plane of an as-deposited cubic component. Prior β columnar grain boundaries and α' lath appear in the microstructure. The vector g^* shows the β grain growth direction [12].

2.4.2.2. Microstructures and Mechanical Properties in Post-treated SLMed Ti64

Table. 2-2 provides some tensile properties of as-built AMed Ti64, where high strength but strong anisotropy can be found with this type of material while Table. 2-3 summarises different microstructural compositions and corresponding tensile properties. The mechanical properties of

as-built part cannot meet the requirement of most industries; hence, post treatment will often be applied to alter the microstructure (recovery of homogeneous, isotropic and stable microstructures) to improve the performance of parts. According to literatures, the effects of heat treatment on material performance is significant for SLMed Ti64. Furthermore, a range of parameters of post treatment were investigated to reach specific microstructures and mechanical properties, for instance in Vrancken's or Vilaro's work, the temperatures were ranging for 540°C~1050°C [9, 26].

Table 2-2 Tensile results for SLM-produced and EBM-produced Ti64 alloy samples [27]

	Stress at yield (Offset 0.2%), MPa	Ultimate tensile stress, MPa	Strain at break, %
EBM (vertically built and Machined)	869 (SD: 7.2)	928 (SD: 9.8)	9.9 (SD: 1.7)
SLM (vertically built and Machined)	1143 (SD: 30)	1219 (SD: 20)	4.89 (SD: 0.6)
% Increase	31	31	-50
EBM (horizontally built and Machined)	899 (SD: 4.7)	978 (SD: 3.2)	9.5 (SD: 1.2)
SLM (horizontally built and Machined)	1195 (SD: 19)	1269 (SD: 9)	5 (SD: 0.5)
% increase	33	30	-47
ASM Handbook (Ref 15) (cast and annealed)	885	930	

Table 2-3 Summary of different procedures for rapid manufacturing of Ti-6Al-4V [6]

	Microstructure	UTS	Yield stress	Breaking elongation
Hot worked	Globular α in $\alpha + \beta$ matrix	870 ± 10	790 ± 20	18.1 ± 0.8
EBM	acicular $\alpha + \beta$	915 ± 10	830 ± 5	13.1 ± 0.4
SLM	acicular α'	$1,095 \pm 10$	990 ± 5	8.1 ± 0.3
Modified SLM	acicular α'	$1,140 \pm 10$	$1,040 \pm 10$	8.2 ± 0.3
SLM variant 1	Lamellar $\alpha + \beta$	915 ± 5	835 ± 5	10.6 ± 0.6
SLM variant 2	Lamellar $\alpha + \beta$ Globular α	990 ± 15	870 ± 15	11.0 ± 0.5

Note: Microstructure and mechanical properties

2.4.2.2.1. Low Temperature Heat Treatment

Stress relief is the essential aim of this treatment, with barely significant microstructure change. On this condition, high dimensional stability can be ensured with acceptable mechanical properties for some industries. During fast cooling in SLM, shrinkage in volume (~6.7%) of melting pool occurs during solidification from fusion isotherm to free surface, as the solid front comes to the liquid. For this material, heat treatment at the temperature of 730°C for 2 hr will relieve residual thermal stress completely, accompanied with partial martensite decomposition to stable $\alpha + \beta$ phase [9].

Due to partial decomposition of martensite α' , the strength (ultimate tensile strength and yield strength) will drop in each loading direction, while ductility will improve slightly but strong texture will still remain and result in anisotropy [28].

2.4.2.2.2. High Temperature Heat Treatment

Accompanied with solution treatment at high temperature but below β transus after SLM processing, tempering treatment will often be applied on the material of a value ranging from 700

to 950 °C [9]. This combination can effectively adjust the grain size, morphology, strengthening phase volume fraction and chemical composition of SLMed Ti64 [9].

The temperature for solution treatment is often set below β transus so as to prevent exaggerated grain coarsening. Supertransus solution treatment applied at 1050 °C for 1 hr with water quenching can also help form martensite α' [9], but the martensite is thicker than in the as-fabricated microstructure due to the relatively low cooling rate. The columnar grains will be sheared during supertransus solution treatment. Above β transus, α' will be completely dissolved, then transformed without diffusion of β phase to α' phase during water quenching. With new grain nucleated, equiaxed microstructure can be obtained, as illustrated in Fig. 2-15.

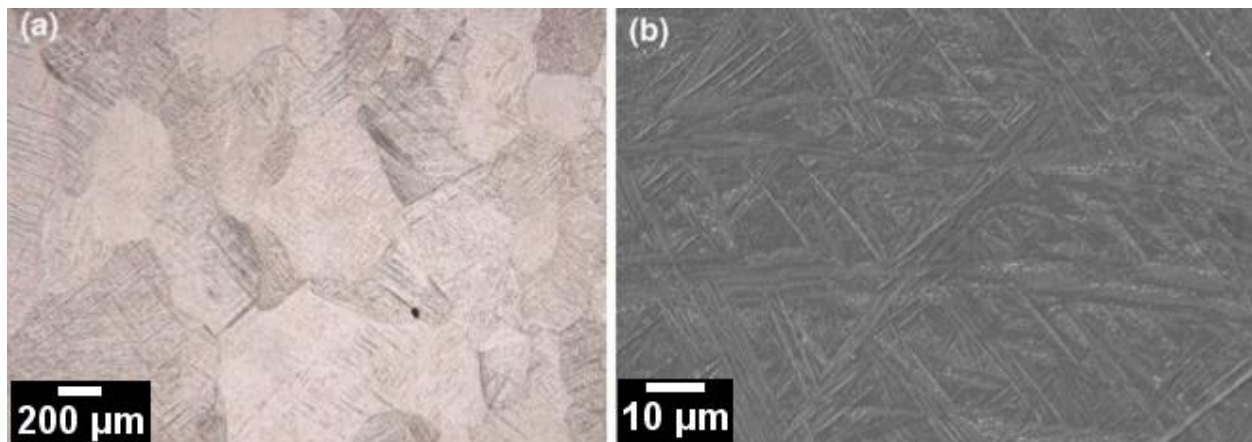


Figure 2-15 Microstructures of the supertransus solution treatment 1323 K (1050 °C/1 h WQ): (a) optical micrograph showing the grain morphology and (b) SEM micrograph in the SE mode showing the α' needles [9].

Subtransus solution treatment at 950 °C for 1 hr with water quenching will not alter the texture of grains as shown in Fig.2-16 as the temperature is not sufficient to enable fully β grain recrystallization. Essentially this treatment will cause gradual martensite α' decomposition to $\alpha+\beta$,

whereas the prior β grain boundaries as well as the texture will not disappear [9, 26].

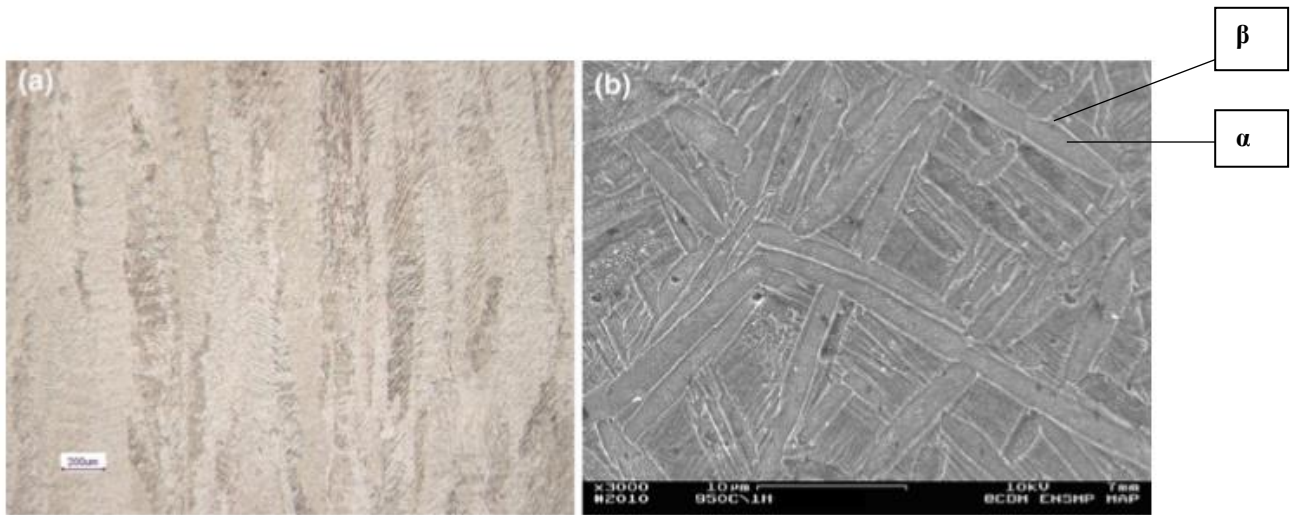


Figure 2-16 Microstructures of the subtransus solution treatment 1223 K (950°C/1 h WQ): (a) optical micrograph showing the grain morphology and (b) SEM micrograph in the SE mode showing the α , α' and β phases [9].

With supertransus treatment, due to coarsening of grains and loss of martensite, the strength of material will drop dramatically, while anisotropy can be lowered significantly. For subtransus treated part, the strength will decrease slightly and anisotropy remains almost the same because significant texture is left [9]. For both cases, the ductility will be much higher than as-built Ti64. The experimental changes in those mechanical properties were demonstrated in the table.

Table 2-4 Mechanical Properties at Room Temperature of the Different Microstructures as well as the Standard Processing Routes [9]

	As-Fabricated		High-Temperature Supersolvus		High-Temperature Subtransus		Low Temperature		As Cast	Wrought
	LD	TD	LD	TD	LD	TD	LD	TD		
σ_u (MPa)	1206 ± 8	1166 ± 25	1019 ± 11	951 ± 55	1036 ± 30	1040 ± 4	1046 ± 6	1000 ± 53	980	995
$\sigma_{0.2 \text{ pct}}$ (MPa)	1137 ± 20	962 ± 47	913 ± 7	836 ± 64	944 ± 8	925 ± 14	965 ± 16	900 ± 101	865	930
ϵ (pct)	7.6 ± 2	1.7 ± 0.3	8.9 ± 1	7.9 ± 2	8.5 ± 1	7.5 ± 2	9.5 ± 1	1.9 ± 0.8	13.5	14
E (GPa)	105 ± 5	102 ± 7	96.7 ± 5	95 ± 4	103 ± 11	98 ± 3	101 ± 4	110 ± 29	/	/

2.4.2.2.3. Hot Isostatic Pressing Treatment (HIP)

Hot isostatic pressing is an efficient way to improve the ductility and fracture toughness of SLMed Ti64. Typically HIP apparatus can be used to apply gas pressure with argon. Besides the above mentioned effects of heat treatment on microstructures and properties, high pressure is capable of helping close the residual pores insides parts. A relative density over 98% can be achieved by optimized processing parameters [28, 29, 11]. HIP treatment can minimize the porosity down to 0.001 vol%. Diminishing internal pores by HIP can reduce localized stress concentration and improve the impact energies especially for the vertically built parts and make their performance close to horizontally built parts; hence, it lowers the anisotropy [30, 31]. Fig.2-17 compares pore distribution before and after HIP treatment. Furthermore, the influence of heat treatment conditions on mechanical properties is shown in Table. 2-4.

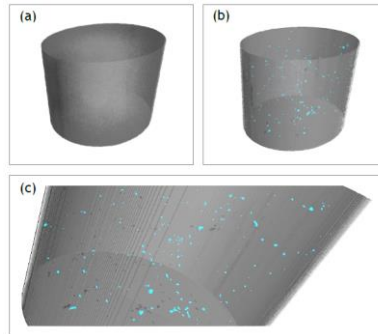


Figure 2-17 CT scan of a 3 mm diameter cylinder showing porosity (blue coloured) and distribution, where a) HIP, b) as-built. a) After the HIP process the porosity was below the resolution limit of 3 μm . c) is enlargement of b) to show the pore orientation and distribution [32].

Table 2-4 influence of heat treatment conditions on Ultimate tensile strength, 0.2% offset yield strength and elongation at failure [33]

Heat treatment	UTS (MPa)	σ_y (MPa)	ϵ_f (%)
As-built	1080	1008	1.6
800 °C	1040	962	5
1050 °C	945	798	11.6
HIPed	1005	912	8.3

Similar to heat treatments as mentioned in previous section, high temperature set in HIP can also affect the volume fraction of the binary microstructures.

2.4.2.3. Texture Evolution in SLM Ti64

Crystallographic texture analysis by Electron Beam Scattering Diffraction (EBSD) is regarded as a useful method to investigate relationship of the processing, heat conduction and microstructures of $\alpha+\beta$ alloys in order to improve the mechanical properties [34]. Usually EBSD is applied to characterize local texture of materials. As shown in Fig. 2-18 in lateral profile of as-built sample, the possibility for α' colonies growing in the same crystallographic orientation with prior β is low. Statistically in an SLMed Ti64, α' texture occurs random due to the large amount of α' variants within each prior β grain. The prior β grain can be reconstructed by calculation software via Burgers relationship and mapped to show the columnar grain penetrating multiple layers. Also, as illustrated by the pole figure in Fig.2-18, preferential $\{100\}$ growth of cubic structure during solidification makes it the dominant texture for the growth direction of prior β grain (as g^* shown). [12]

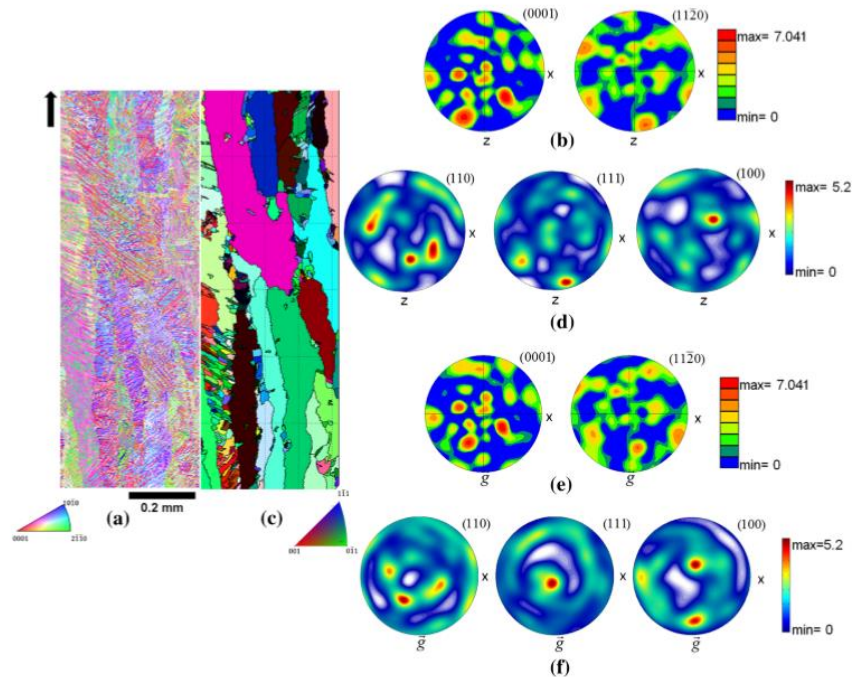


Figure 2-18 (a) EBSD α' orientation map and the corresponding color scheme of a specimen taken from the frontal xz -plane of an as-deposited component (the black arrow indicates the building direction); (b) corresponding $(0001)\alpha'$ and $(11\ 20)\ \alpha'$ contour pole figures; (c) orientation map of the reconstructed β phase. (d) the corresponding (110) , (111) , (100) contour pole figures; (e) $(0001)\alpha'$ and $(1120)\alpha'$ contour pole figures of the α' data set (f) (110) , (111) , (100) contour pole figures of the corresponding rotated β phase [12].

In the plane perpendicular to building direction, α' grains display very weakly in texture as shown in Fig. 2-19. According to the pole figure, in each prior β grain there can be 5 to 6 α' variants. It fits Burgers relationship that the $(0001)\alpha'$ plane of each α' is parallel with $(110)\beta$ set of planes in prior β grain, and one at least of $\langle 11\bar{2}0 \rangle\alpha'$ is parallel to one of $\langle 111 \rangle\beta$ set.

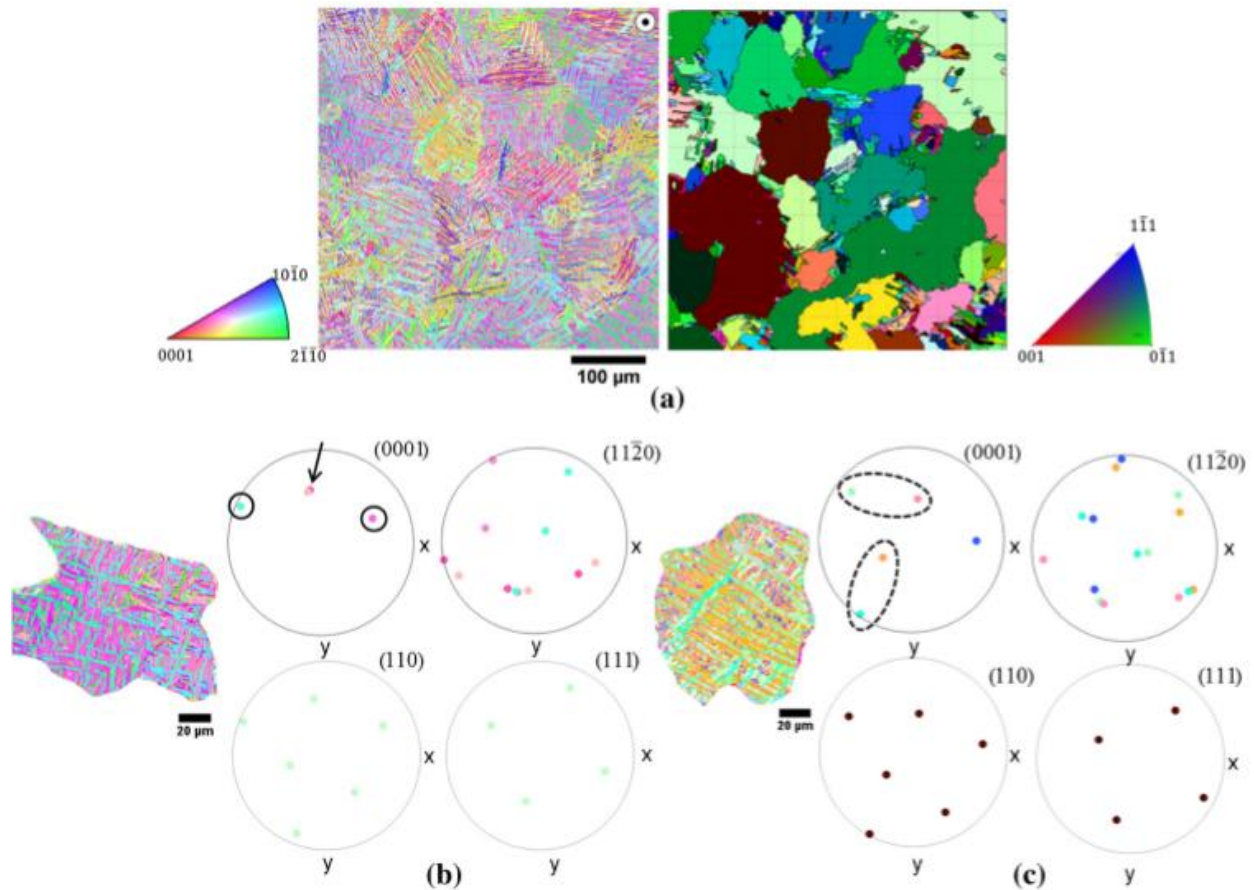


Figure 2-19 (a) α' and corresponding reconstructed β orientation maps from the horizontal xy-plane; (b) and (c) discrete pole figures of the α' variants and their parent β grain [12].

The pole figure study also revealed that within one prior β grain even through successive deposited layers, α' laths formed in similar orientations will cover most of entire prior β grain, which suggests preferred variant selection of α' should have taken place when heating up to β phase region, and then cooling down rapidly [35]. Due to remelting of the top part of a new layer deposited in SLM,

martensite will decompose to β phase which then transform to martensite again; hence, there are many kinds of possible variants. Actually, mostly $(0001)\alpha'$ within one prior β grain tends to reflect 60° misoriented to $\langle 01-10 \rangle$ axes which fit Burgers relationship [12, 36].

According to relevant studies on the change of microstructure with building direction [37, 24], the microstructures will vary along with the height of SLMed Ti64, i.e. elongated grains from the substrate, and more equiaxed grains away from the substrate. One given explanation is that due to heat conduction from melt pool, elongated grains grow epitaxially from the substrate or previous layer towards the central line of melt pool. At the same time equiaxed grains form at the moving liquid front of melt pool, but the next layer will remelt them as long as the layer thickness is smaller than the melt pool depth [37]. Elongated prior β grain plays an important role in anisotropy issue of SLMed Ti64.

2.5. Scanning Strategies and Microstructures

2.5.1. Common Scanning Strategies

Parallel scanning strategies contain unidirectional scanning strategy and zigzag scanning strategy, and their scanning track paths are illustrated respectively in Fig. 2-20. The first picture shows the zigzag scanning and the second is the unidirectional scanning (the tracks can be just along with x or y axis), the last is a more commonly used cross-hatching scanning strategy.

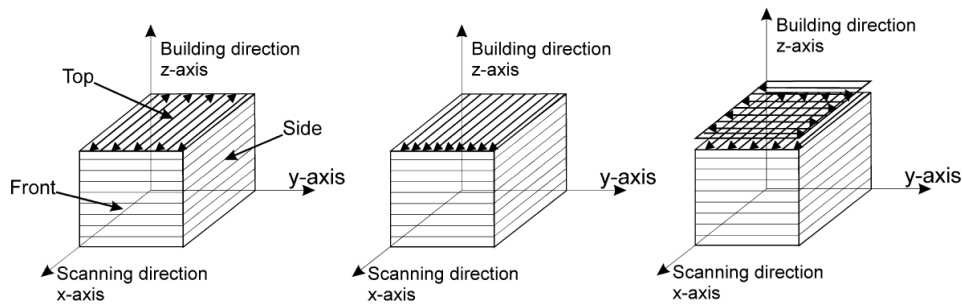


Figure 2-20 Three different scanning strategies, namely identical scanned layers using zigzag (left) or unidirectional scan vectors (centre) and the cross-hatching technique using the zigzag scan vectors (right)

[11].

The cross-hatching technique applies zigzag scanning vectors that rotates by a certain angle when scans for the next layer as shown in the right picture in Fig. 2-20, in which a rotation angle of 90° is applied. In theory, the angle can be altered to any value and in practice 90° [6] and 67° [12, 38] are two commonly used angles. This cross-scanning method can lower the anisotropy of material when compared with the parallel scanning strategies [39].

Island scanning is an evolved type of cross-hatching technique. The evolution is to separate each layer by grid net where one grid is called an “island”, and to scan parallelly within each island, then to rotate scanning direction in neighboring island, as illustrated in Fig 2-21. This method is able to further decrease the anisotropy in SLMed Ti64.

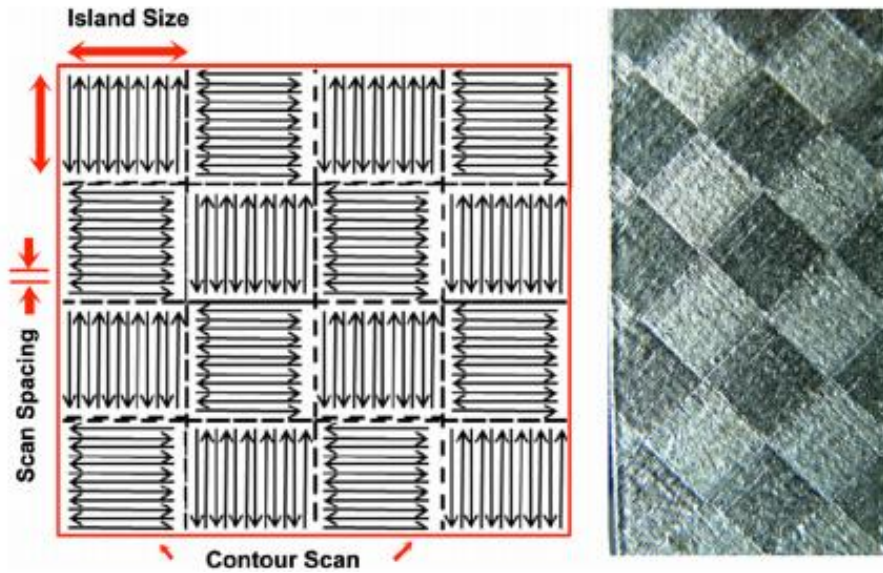


Figure 2-21 The ‘islands’ scanning strategy on the Concept Laser M2 Cusing SLM system, and the typical chessboard morphology on the surface of a Ti-64 rectangular build [29].

Fig.2-22 describes the difference between island scanning (D, E) and other scanning strategies (A, B, C) .

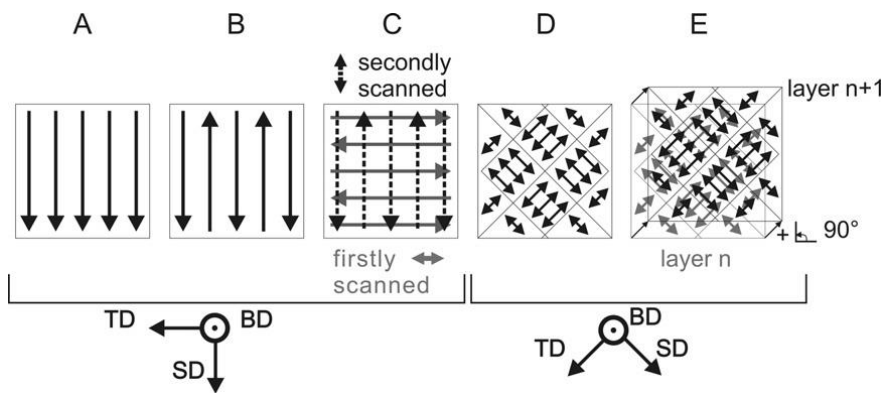


Figure 2-22 Overview of the scanning strategy used for the different samples. The building (BD), scanning (SD) and transverse direction (TD) are indicated [39].

2.5.2. Influence of Scanning Strategy on Microstructures

Usually, due to overlapping of melt pool in the vicinity of each single scanning track, part of already-solidified material will be remolten and solidified again. Hence, the microstructures within the overlapping area appear different when compared to the microstructures of matrix as observed in Fig. 2-23. In the picture below, a plane view perpendicular to the building direction can be observed with an enlarged chessboard pattern of a rotation angle of 90° , and clearly the martensite grains within overlapping area appears with different morphology to the grains within the chessboard grids matrix area. This overlapping area forms the chessboard interfacial area [10].

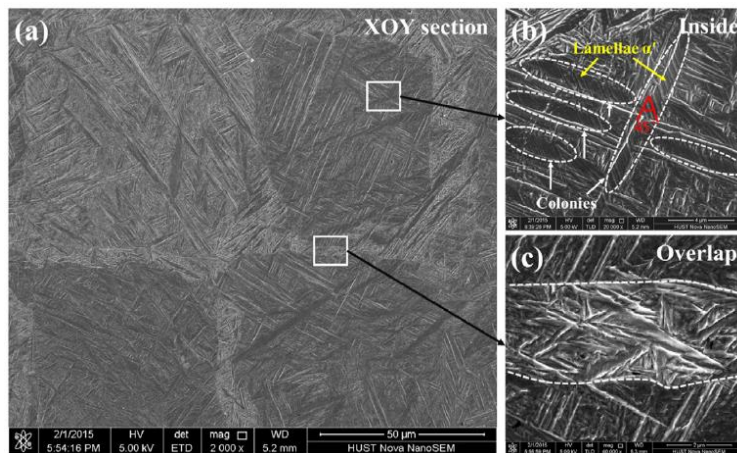


Figure 2-23 SEM images of SLMed Ti-6Al-4V cuboid samples on XOY section; (b) and (c) are the high magnification images of the areas indicated by the white boxes in (a) [10].

An illustration of these featured binary microstructures was shown in Yang's work, besides, the generation of featured binary microstructures was explained as well. However, the morphological information of the binary microstructures was not quantified.

Different scanning strategies result in various microstructures; however, the overlapping effect can always exist as long as the hatching distance is smaller than the melt pool size, which is necessary for fully melting powder raw material. Hatching distance means the distance between neighbouring laser tracks. From the SEM images of the plane perpendicular to building direction

from different scanning strategies, the geometry of “chessboard” can vary from square grid of 90° rotation to herringbone of zigzag scanning as demonstrated in Fig. 2-24.



Figure 2-24 From left to right: top-view microstructures of unidirectional scanning strategy, cross-hatching scanning strategy, zigzag scanning strategy [24].

Furthermore, more detailed local properties of the microstructures within the interfacial area such as the strength still lack of investigation. In additive manufactured Ti64, the cracks were found initiating in parallel at a certain distance, and growing along with the building direction [40, 41]. With binary microstructure taken into consideration, cracks tend to initiate at the interfacial area. As illustrated in Fig. 2-25, crack paths lay in prior β grain boundaries. However, the mechanical properties of two areas need to be investigated further to figure out the reason behind this crack paths.

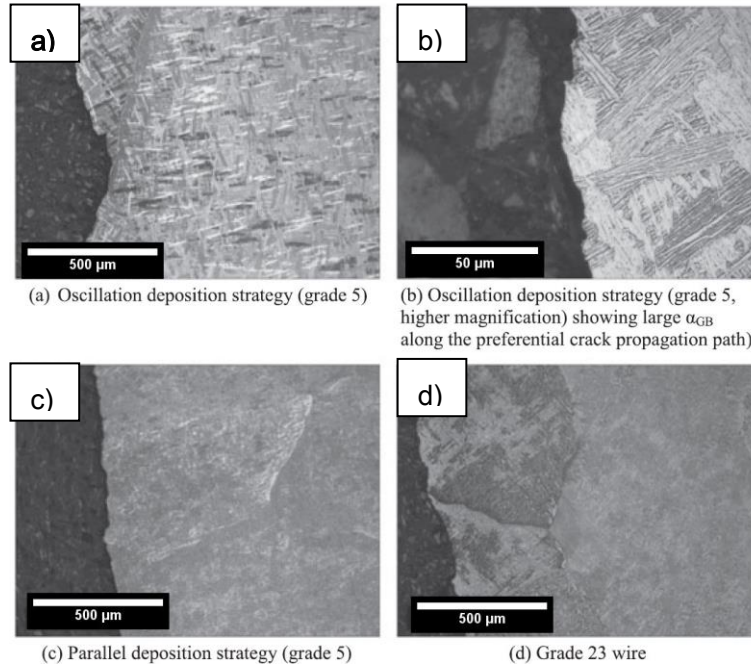


Figure 2-25 Optical microscopy images of the crack, highlighting the preferential path along the prior β grain boundaries a) Oscillation deposition strategy b) Oscillation deposition strategy higher magnification c) Parallel deposition strategy d) Grade 23 wire [42].

2.5.3. Generation of Mesostructures

Due to the pattern of parallel laser scanning at some certain distance in cross-hatch scanning strategy, the binary microstructures will occur periodically and hence form the mesostructure called “chessboard”. Recently P. Kumar et. al. [43] published their work of 3D representative microstructure of Ti64 as shown in Fig.2-26. They observed a regular texture of SLMed Ti64, as shown in Fig.2-26 (d) where prior β grains tend to grow in $\langle 001 \rangle$ due to epitaxial growth and α grains orient in $\pm 45^\circ$ to β grain orientation due to Burgers relationship [11]. In Kumar’s work, it was also illustrated that the columnar prior β grains make up the “chessboard” mesostructure in building direction and in the normal plane [43]. A schematic draft of a hatch angle of 90° was also provided to clarify this hatch angle between neighbouring successive layers as well as its influence on the “chessboard” pattern mesostructure. Dashed lines were applied to circle out the

boundaries of one grid from “chessboard” mesostructure at both planes.

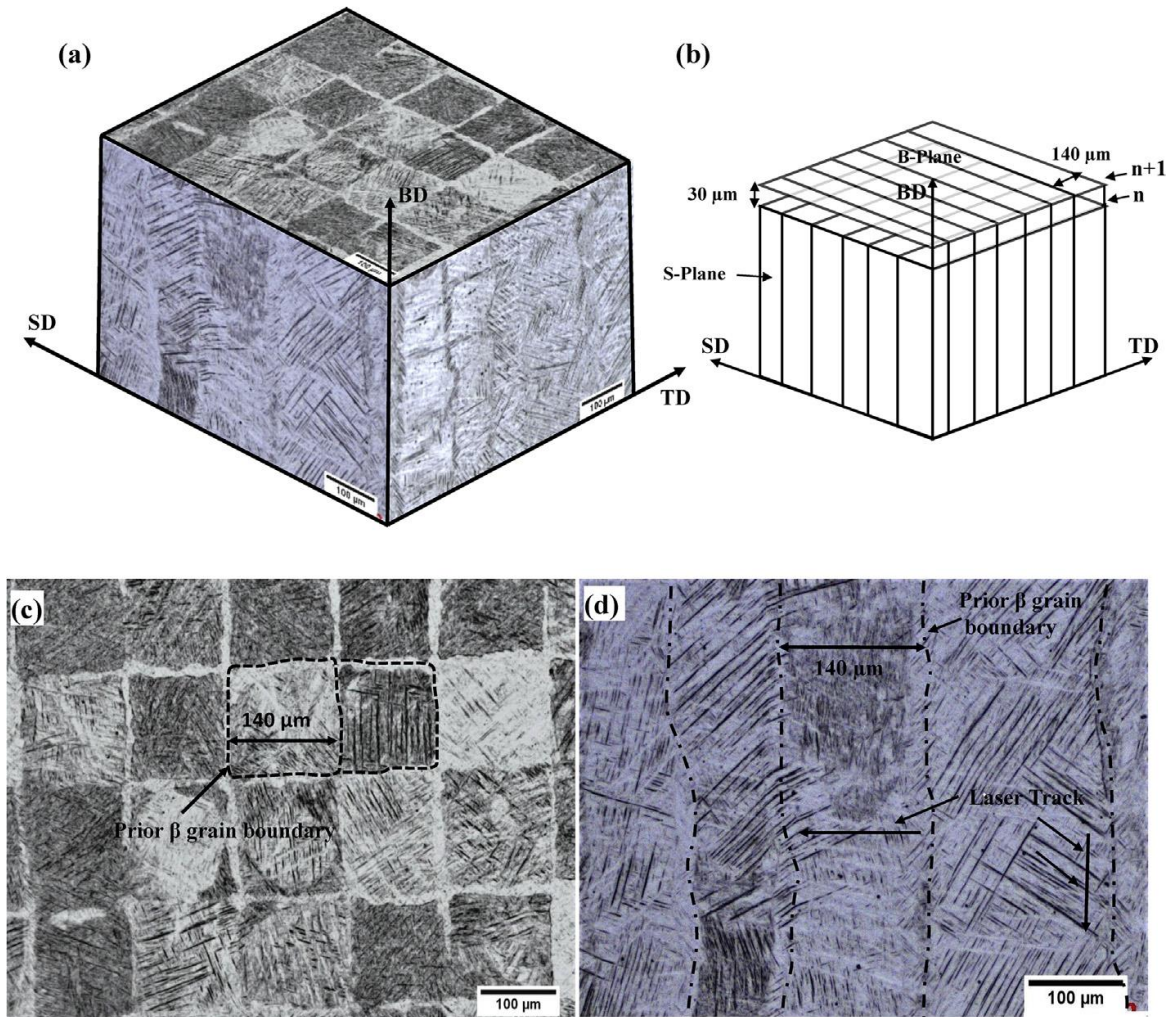


Figure 2-26 a) 3D representative microstructure of Ti64 samples. b) Schematic representation of the scan rotation of 90° between each successive layer, where B represents the plane normal to building direction, S represents the plane parallel to building direction, as shown. c) Microstructure of B-plane. d) Microstructure of S-plane [43].

Table 2-5 Summary of the mechanical properties of SLM Ti64 examined in this study, where B and S represented building direction and normal to building direction, the first two digits mean layer thickness and the last two mean hatch angles [43].

Sample	σ_Y (MPa)	σ_U (MPa)	e_f (%)	K_{Ic} (MPa \sqrt{m})	ΔK_0 (MPa \sqrt{m})	m	FS (MPa)	FS/σ_U
B3090	1161 ± 30	1237 ± 30	7.6 ± 1	52	5.6	2.53	340	0.28
S3090	1029 ± 8	1091 ± 6	7.8 ± 0.8	55	5.7	3.31		
B3067	1121 ± 42	1186 ± 42	8.1 ± 0.6	48	5.3	3.55	340	0.29
S3067	1121 ± 9	1202 ± 11	10.1 ± 0.3	54	5.7	3.08		
B6090	1151 ± 11	1222 ± 25	9.8 ± 1.1	51	5.8	2.87	453	0.37
S6090	1115 ± 18	1183 ± 22	9.7 ± 0.3	52	5.8	2.89		
B6067	1102 ± 16	1145 ± 14	12.5 ± 1.4	58	5.4	3.51	475	0.41
S6067	1063 ± 17	1137 ± 23	12.8 ± 0.9	58	5.7	3.48		

In Kumar's work, 90 ° and 67 ° cross-hatch scanning strategies were compared on both microstructures and tensile properties of the material, and some other processing parameters such as layer thickness were evaluated on the material's properties. From the table 2-5, it can be found that 67° scanned sample tends to have less strength but higher ductility. However, the local mechanical properties of interfacial area and matrix area on micron scale haven't been mentioned.

2.6. Finite Element Analysis

In previous studies, finite element analysis was applied to simulate the process of selective laser melting Ti64 [44, 45] in order to predict residual stress, strain (distortion) and temperature gradient. For instance, in Fu's work [45], a temperature gradient in material was established via thermal history simulation of the process. The geometry of melt pool also was predicted in the simulation. In his work, a temperature gradient profile in SLMed Ti64 during simulated process was captured in Fig. 2-27 (a), where the size of melt pool was measured as Fig. 2-27(b) shown.

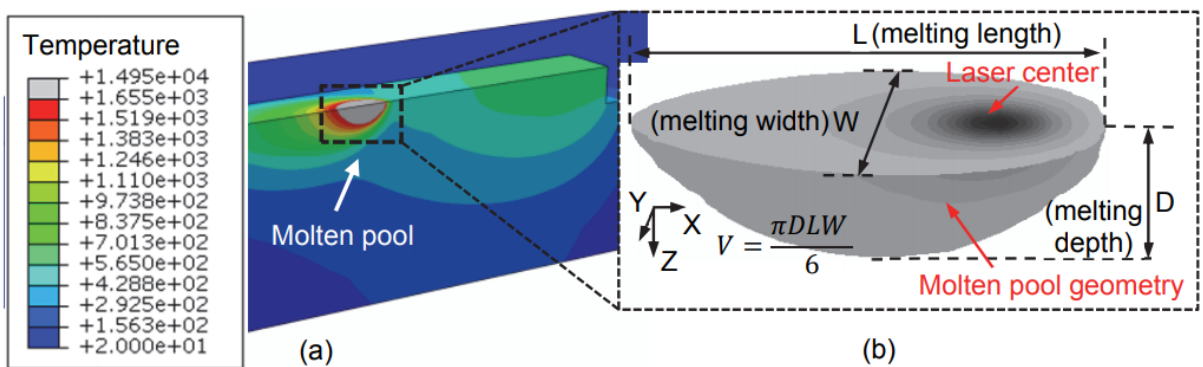


Figure 2-27 (a) Representative temperature contour and (b) melt pool geometry [45]

This simulation made it possible to predict the temperature gradient of material and melt pool size which are regarded as the factors dominating material performance and limitations under various processing parameters such as different power input. The results revealed some key issues in this material such as prediction of no balling, and different temperature gradient along the depth and width.

Also, the stress-strain behavior and prediction of mechanical properties of bi-phase Ti alloy were carried out by FEA as shown in Fig. 2-28 and 2-29 from another work by [46]. To avoid a huge amount of computing, a statistic volume element for a periodic microstructure was created as illustrated in Fig. 2-28. Binary microstructures could be simulated by this method in order to obtain

overall material properties. Different from usual FE study in SLMed Ti64 based on meshing whole part, the simulation in this study would mesh binary microstructures to carry out the analysis.

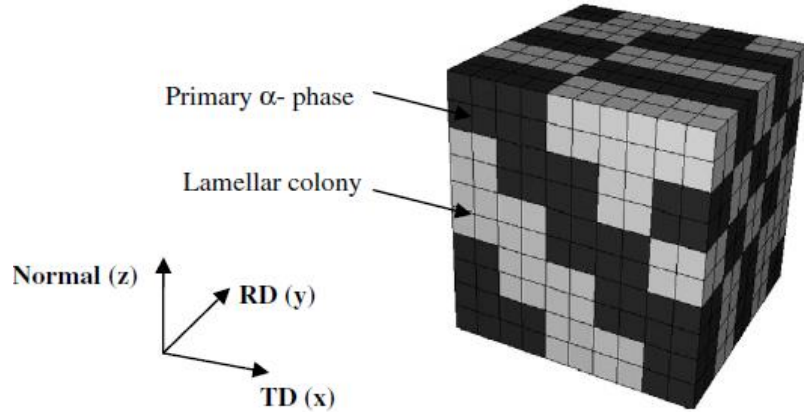


Figure 2-28 Finite element model of periodic polycrystal [46].

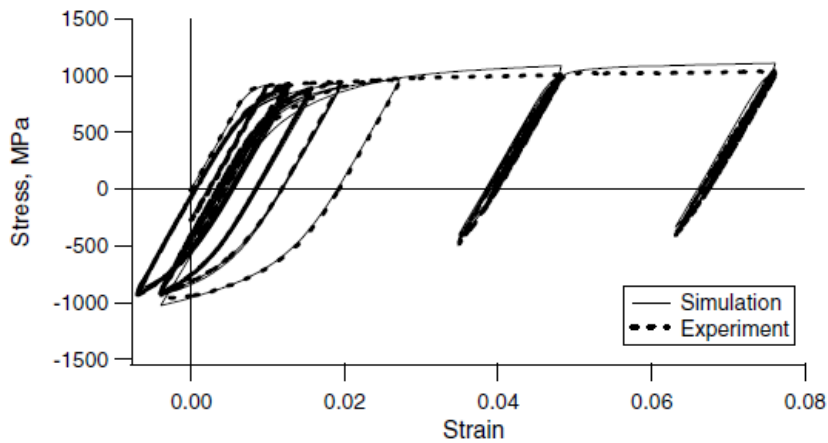


Figure 2-29 Comparison of model simulation of stress–strain curve with experimental results for Ti–6Al–4V at room temperature, for the uniaxial strain history with constant strain rate and with no hold periods [46].

These FE simulation works did investigation on Ti64 [44, 45, 46]. The SLM process was simulated mostly to predict temperature gradient, residual stress or distortion of the material. Otherwise, conventional processed Ti64 was simulated on microstructure level [46], where the method of RVE for a periodic microstructure was created.

2.7. Nanoindentation

Nanoindentation is capable of applying indentation force in millinewton scale and detect indents geometry at nanometer level. Generally, the mechanical response of a tested material with a known reference indenter tip can be quantified to derive some mechanical properties of the material which is to be tested.

According to the geometry of indenter applied as marked in Fig.2-30, with load versus displacement curve obtained from nanoindentation experiment, hardness and Young's modulus of a local specific microstructure can be calculated [47, 48] by Oliver-Pharr indentation method. With load and displacement response in the material shown in Fig.2-31, hardness and elastic modulus of the material can be calculated.

As I.M. Hutchings suggested [49], the yield strength of a material is dependent on hardness at some coefficient, such as that in steel, there is $H = 3\sigma_y$. This suggests that the yield strength of a material can also be measured in nanoindentation test. However, the hardness dependence on yield strength may vary in different materials. Regarding SLMed Ti64, there is a featured fine lamellar structure. An analogous situation can be found in Sui's study [50], where the relationship between yield strength and hardness is fitted as: $\sigma_{0.2} = 447.6 + 0.87HV$. In the present study, the instrumented nanoindentation method developed by [51] will be used to measure the mechanical properties especially hardness of two types of microstructures within SLMed Ti64.

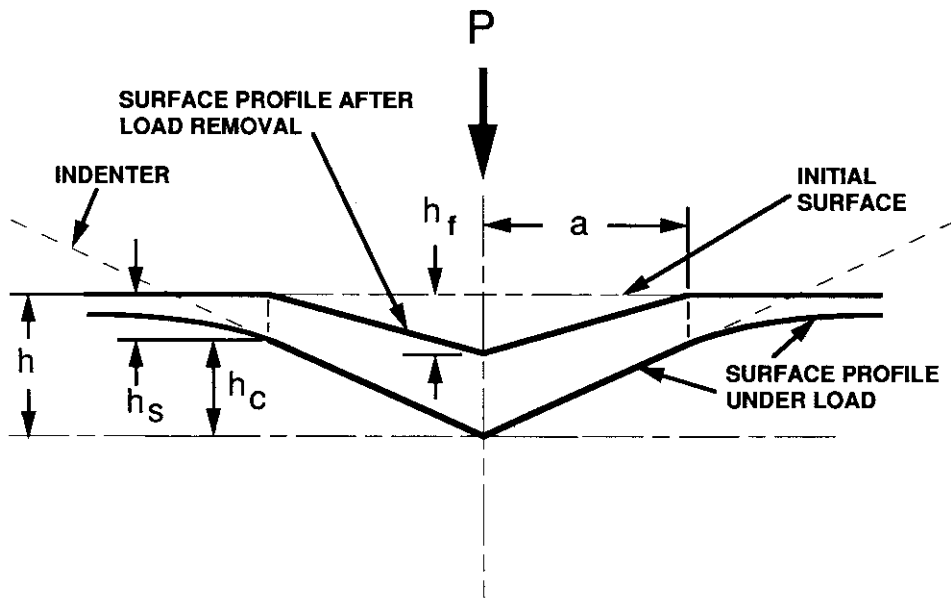


Figure 2-30 A schematic representation of a section through an indentation [47].

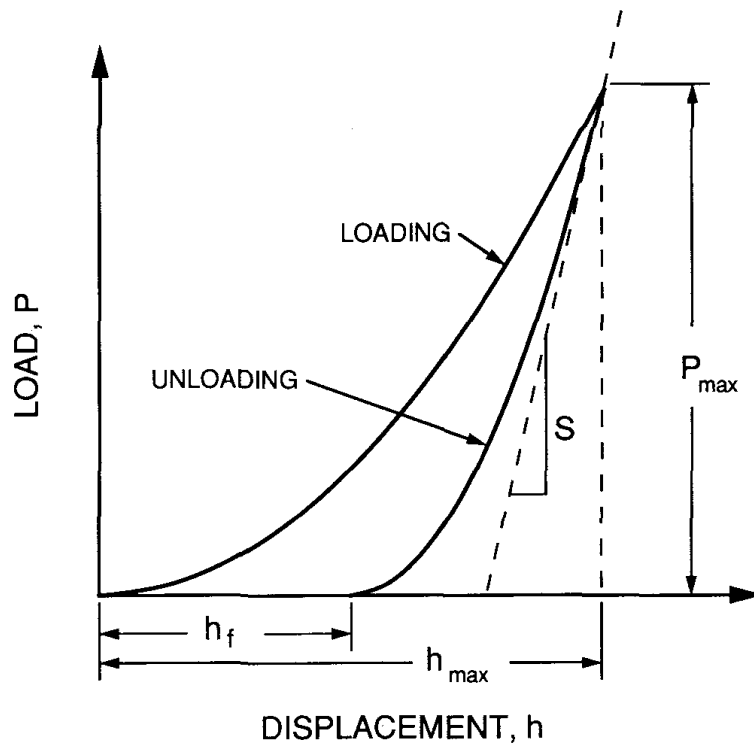


Figure 2-31 A schematic representation of load versus indenter displacement showing quantities used in the analysis as well as a graphical interpretation of the contact depth [47].

2.8 Summary

Researchers have made great efforts in studying the microstructures and the mechanical properties of SLMed Ti64, in order to achieve high quality and performance in applications. As a common phenomenon in SLMed Ti64, the binary microstructures have been found. Furthermore, the generation mechanism behind it was explained [10]; the variation in morphology under different scanning strategies was shown in microscopy [24] ; the comparison in mechanical properties of the material corresponding to difference in the “chessboard” pattern has been investigated using tensile test [43]. The featured binary microstructures are promising to be an efficient way to enhance the material performance or reduce the limitations, which requires further investigation.

In my study, more specific characterization and quantified analysis on the binary microstructures in SLMed Ti64 will be addressed. For instance, the average grain size in interfacial area and matrix area will be measured from microscopy. In addition, the influence of two microstructures’ volume fraction and geometry under different scanning strategy parameters, and mechanical properties on the material will be evaluated using FEA. At last, the local mechanical properties of interfacial area and matrix area at micron scale will be characterized using the nanoindentation test.

3. Characteristics of Microstructures in Binary Areas

3.1 Introduction

In Ti64, the conventional manufactured product microstructure is made up by α phase hexagonal close packed (HCP) and β phase body centre cubic (BCC) while selective laser melting can lead mostly to α' martensite. The morphology and composition are dominated by heat conduction history during process and post-treatment as described in many studies reviewed in Chap. 2. The microstructure is investigated to be altered properly for the purpose to investigate mechanical properties of the material.

To be specific, featured binary microstructures were studied in additive manufactured Ti64. For illustration, the prior β grain boundaries were found with composition of martensite in as built SLMed Ti64 [10] and primary α in EBMed Ti64 [52] as shown in Fig. 3-1. Besides some dominant microstructural factors such as size of grain, colony or lath, the volume fraction of different phases which were investigated in post-treatment may influence material performance in applications, the meso-structure [43] containing binary microstructures caused by laser periodic melting pattern in AM also is promising to enhance the material.

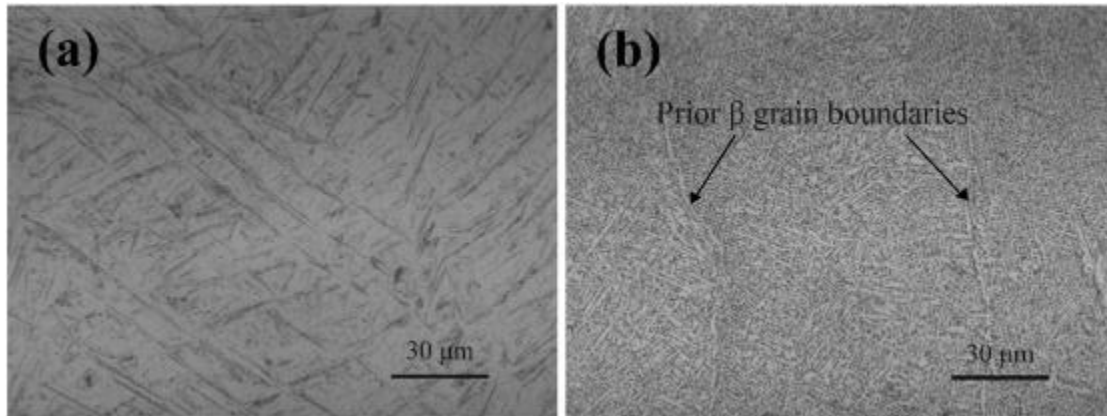


Figure 3-1 Optical microstructures of SLM (a) and EBM (b) samples produced using optimum process parameters. Note the presence of α phase (grain boundary α) on prior β grain boundaries in (b) [52].

Still, there is a lack of quantified works to evaluate the influence of the featured microstructures as discussed on the performance of SLMed Ti64. Some known issues such as anisotropy, crack initiation and growth can be related to this mesostructured. Hence, the local microstructural features and mechanical properties should be investigated in order to explain the issues. The binary microstructures and mesostructure in SLMed Ti64 were studied in this chapter mainly focusing on morphologies, volume fraction, composition and geometry under different scanning strategies.

3.2 Methodology and Materials

SLMed Ti64 was fabricated of gas atomized pre-alloyed Ti-6Al-4V powder from Falcon Tech Co., Ltd. The powders were in spherical shape with a diameter up to 63 μm . Further chemical analysis was performed on both powder and SLM samples. The chemical analysis shows O pick-up of 368 ppm from 1348 ppm in the powder to 1716 ppm O in the SLM samples. The SLM machine is Concept Laser X-Line 1000, the substrate was pre-heated to 70°C and the build chamber was maintained in Argon atmosphere. Samples were printed by using the laser power of 350W, scan speed of 770mm/s and hatch distance of 0.18mm, layer thickness was about 50 μm . The laser scan

direction altered 90° and 0° separately at each layer.

The microstructure of selective laser melted samples were studied by using GX51 Olympus microscope. Before the observation, sample surface was ground and polished down to OPS grade. Multiple images had been taken and then joint together to present the microstructures in a continuous manner.

The Microstructure of selective laser melted samples were studied by using a scanning electron microscope (SEM) JOEL 7001 and techniques including electron backscattered diffraction (EBSD), scanning electron imaging (SEI) and backscattered electron imaging (BSI). The plane of samples that were perpendicular to the building direction were scanned by using EBSD technique, and the plane of samples that were parallel to the building direction were scanned and studied by SEI and BSI. Software Channel 5 HKL was used to analyze the EBSD results.

3.3 Results and Discussion

Both optical and electron microscopies were applied to obtain a direct view of SLMed microstructures in different directions. There is a lateral view of unidirectional scanned Ti64 sample under optical microscope in Fig 3-2. The arrow pointed the direction of building direction. At this scale, columnar prior β grains length can be measured, which is at millimeter scale, as highlighted in Fig 3-2.

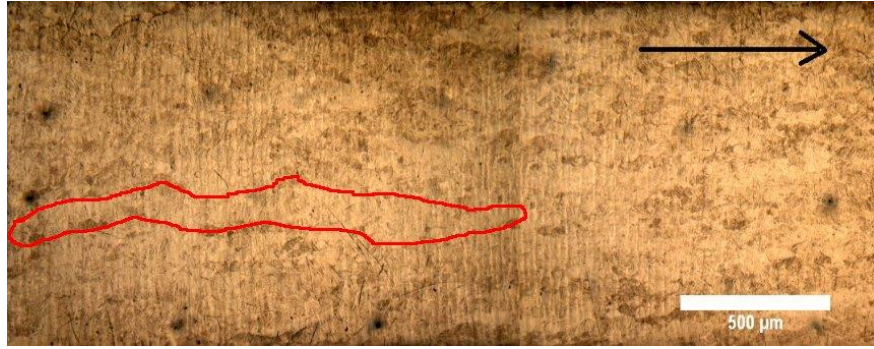


Figure 3-2 Optical microscopy of lateral view of SLMed Ti64

This phenomenon can also be observed in the BSE images in Fig. 3-3. Besides, the enlarged local microscope shows various lengths of prior β grains in different positions along with the building direction. Similarly, prior β bands were elongated for even longer than 0.5mm in this BSE image of the microstructure near the bottom region, as illustrated in Fig. 3-3. However, when the microscopy was moved to the top of the part (along with the building direction as arrow marked), prior β grains turned shorter and even became equiaxed shape.

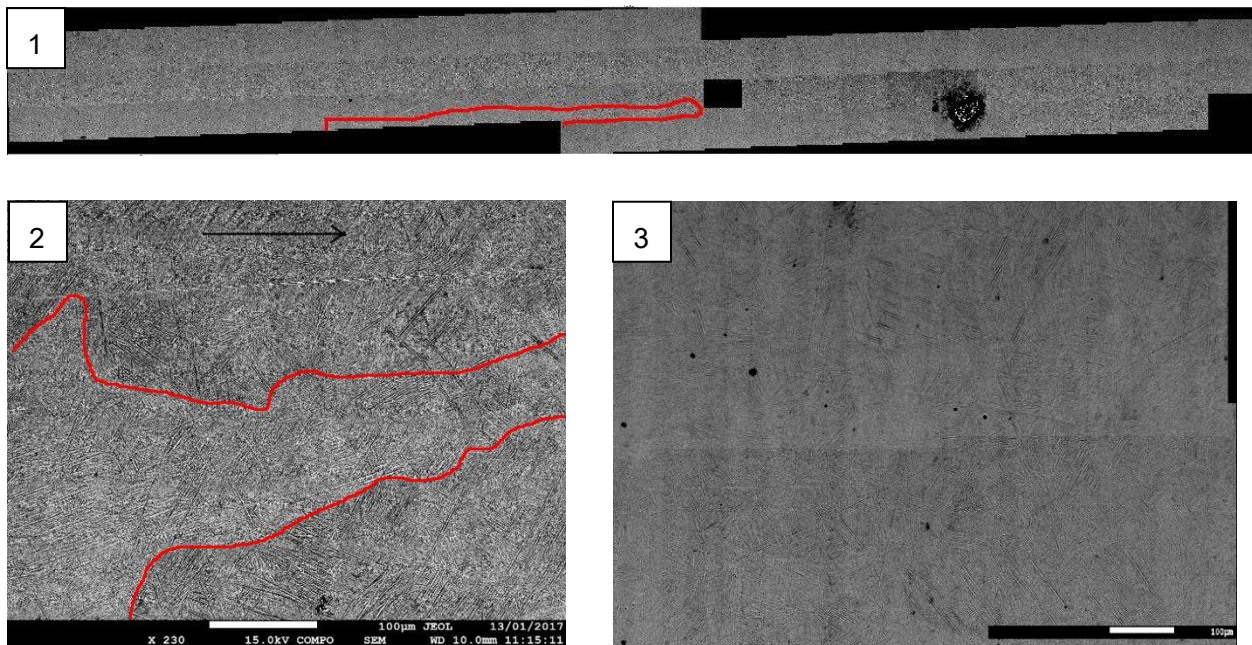


Figure 3-3 BSE images of lateral view of SLMed Ti64: 1) overall view, 2) near bottom and 3) near top. Prior β grain highlighted in red contour shape and, building direction indicated by black arrow.

Fig. 3-4 was EBSD image carried out on cross-hatching scanned Ti64 (as fabricated). Indexable grains in this map are mostly composed by ultra-fine hexagonal-Ti (α'). Furthermore, the microstructures image demonstrated that in the as-fabricated Ti64, grains are quite fine with the size to 10^{-1} μm . In the plane perpendicular to building direction, the “chessboard” pattern can be identified obviously. In addition, the length of “chessboard” grid corresponded to the hatch distance as recorded as $180\mu\text{m}$. The grains' orientations seem to have some preferential directions within one grid and are different in different grids, i.e. the martensite laths lying in the same grid (prior β grain) have the $(0001)_{\alpha'}$ reflection misorientated at 60° with the $\langle 01-10 \rangle_{\alpha'}$ of rotation while reflections $(11-20)$ do not tend to follow any precise pattern [38]. As the consequence, the overall texture among this plane appears very weak. Corresponding pole figure shows that no clear preference of growth orientation can be found.

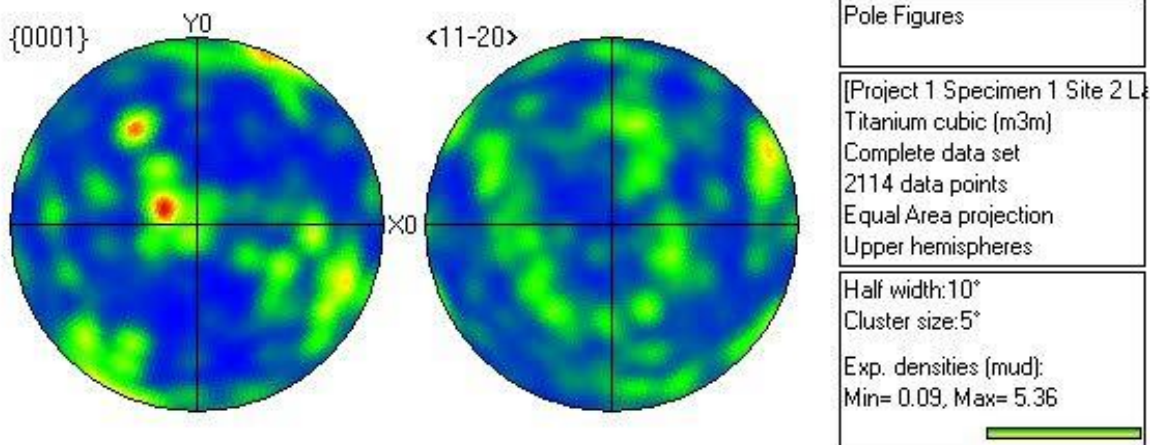
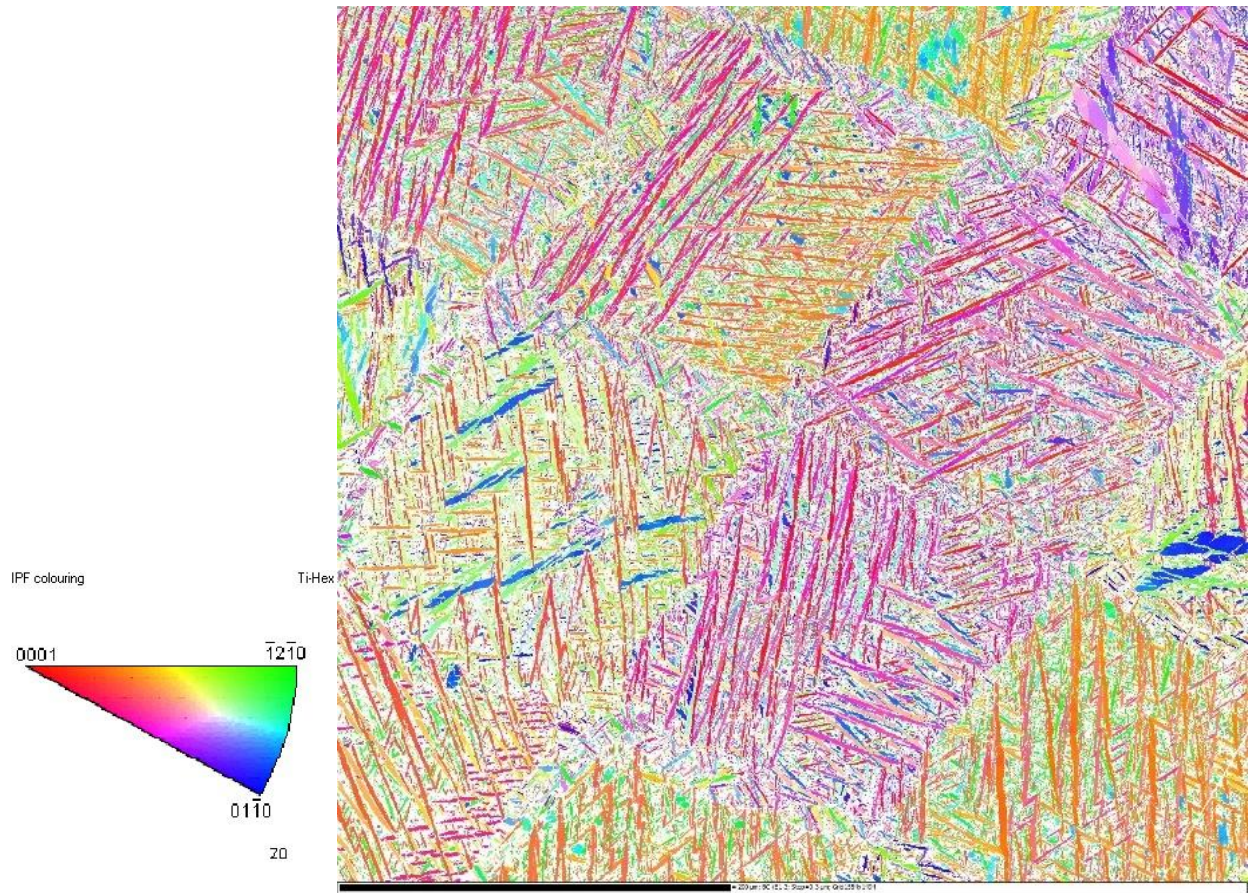


Figure 3-4 EBSD image and pole figure of top view of SLMed Ti64.

It is worth noting that the directions and grain size of the microstructures existing within the grid interface of “chessboard”, appeared quite different to those grain morphological features of the microstructures enclosed by the grid of the “chessboard”. The grains tend to be finer than the grains in the grid matrix as illustrated in the EBSD image (Relevant measurement and calculation can be found in Chap. 7). Besides, the grain orientations in this grid area are more likely to be different with neighboring area.

The generation mechanism of this “chessboard” pattern mesostructures which contain binary microstructures is illustrated in Fig. 3-5. During laser scanning along with the designed pattern, each scan track will cause a melt pool in material around itself. The laser track width is the size of melt pool in material. Furthermore, the overlapping of neighbouring melt pool will lead to remelt of local material, and, consequently, the microstructures in this grid area, named interface; hence, get finer than other area in melt pool, named matrix.

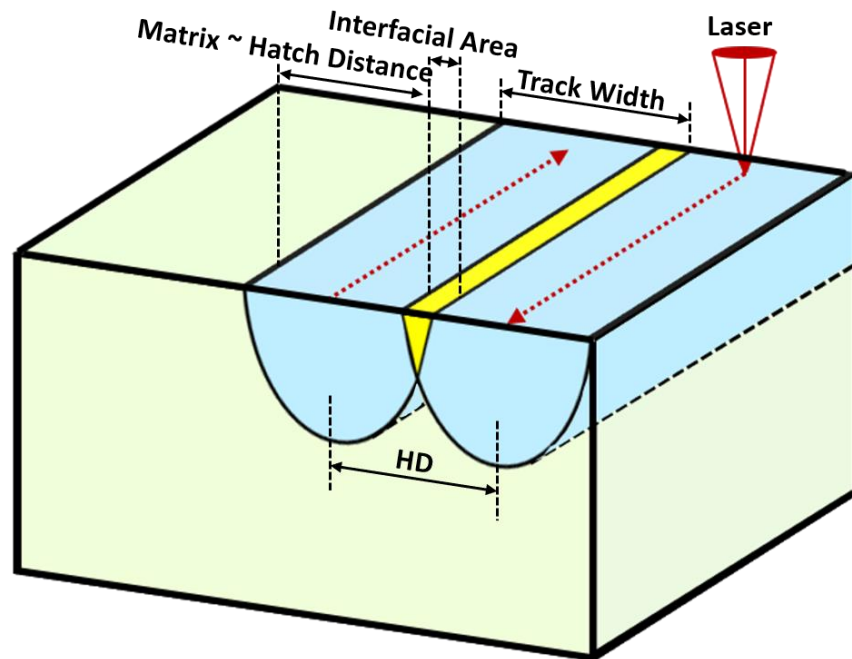


Figure 3-5 Sketch of overlaps of melt pools in the direction parallel to building direction.

The microstructure of the plane parallel to building direction was also characterized by EBSD as shown in Fig. 3-6. Similarly, the prior β grains were elongated over several millimeters. Also, there is a great number of fine martensite grains in certain preferential directions within one prior β grain region ($\pm 45^\circ$ to β grain direction), which is corresponding to the regularity within one grid of “chessboard” as discussed above. Similar to the features described in literatures [24, 12, 34], the martensite grains tend to grow in angles of about $\pm 45^\circ$ to the prior β grain growth directions.

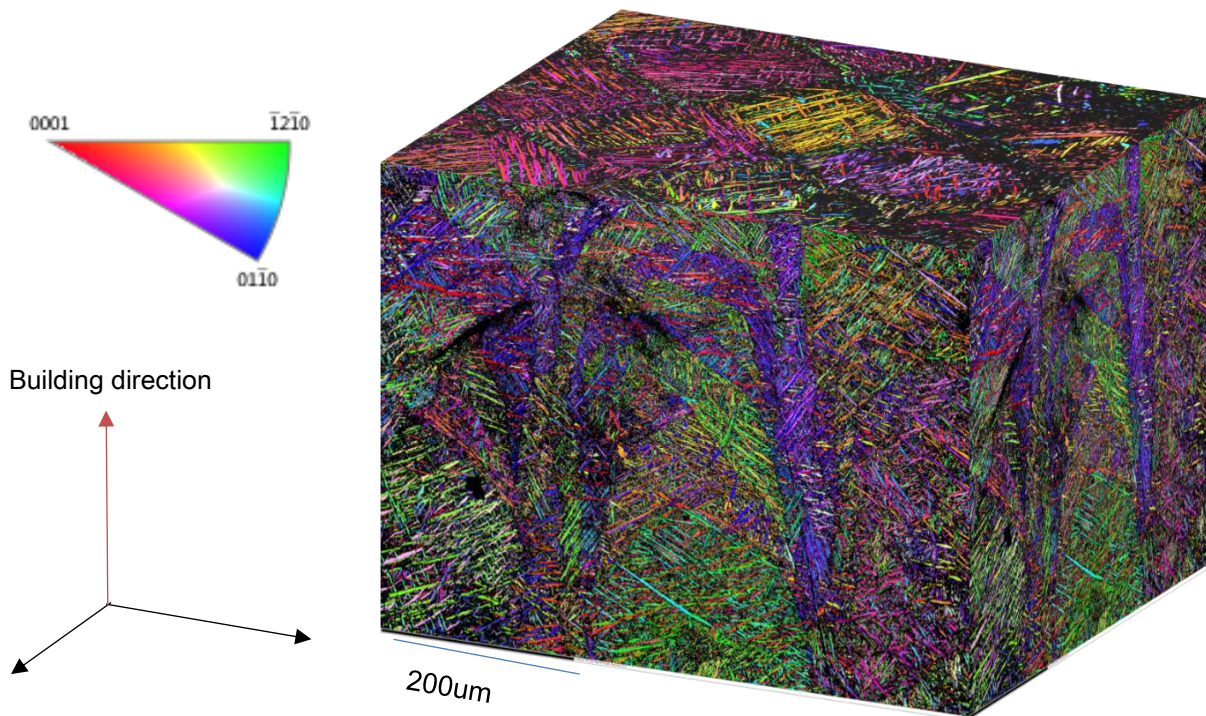


Figure 3-6 EBSD map of 3D-view of SLMed Ti64 (elongated prior β grains contained).

3.4 Summary

Microstructural characterization of selective laser melted Ti64 indicated that there are binary microstructures in periodical mesostructure “chessboard”. The illustration correlates the chessboard grid to prior β grains in SLMed Ti64 in horizontal direction as well as vertical direction. Two kinds of microstructures in different morphology but the same phase (in as-built sample, martensite mostly) lie in the mesostructure as matrix area and interfacial area. The influence of the microstructures on the material properties will be studied in the next chapter.

4. 2D Finite Element Analysis

4.1 Introduction

In order to analyse the relationship of microstructure and mechanical properties, finite element method (FEM) is an efficient way to simulate material behaviors. Many studies have applied FEM on simulation of Ti alloys, such as thermal history during machining of Ti alloy [53].

Specifically, it has been observed that there are binary microstructures in SLMed Ti64 caused by overlapping of melt pools and they may be controlled by some processing parameters [10]. Furthermore, the periodic occurrence of the binary microstructures can form a kind of mesostructure in some pattern due to the regular laser scanning pattern in process. And FEM will be utilised to create such mesostructure model and simulate the mechanical behaviors.

4.2 Methodology and Materials

All simulation in this study was conducted using Abaqus 6.14, a software suite for finite element analysis and computer-aided engineering.

4.2.1 Creation of Representative Volume Element (RVE)

Firstly, the mechanical properties were considered on 2D planar microstructures. Specifically, the “chessboard” pattern on planes perpendicular to building direction is generated by cross-hatching scanning with a hatch angle of 90° , which is a regularly geometrical and periodical mesostructure. An RVE of a quarter of one grid of “chessboard”, composed by interfacial area and matrix area was created as a simplified RVE for 2D planar microstructure, as illustrated schematically in Fig. 4-1. For as-fabricated samples, interface and matrix are mostly composed by martensite but in quite different morphologies, such as different grain size and orientations as illustrated in microstructures results.

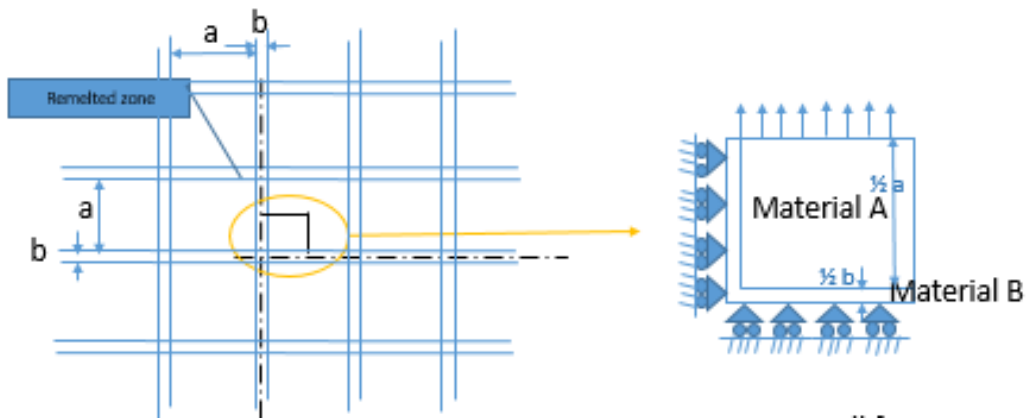


Figure 4-1 Schematic sketch of idealized periodic microstructures and RVE for FEA, where a and b represent for matrix and interfacial area size respectively.

Regarding another scanning strategy such as hatch angle of 67° , the RVE was determined from analysis of simplified (right) provided microstructure image (left) as shown below in Fig. 4-2. Parallel lines at hatch distance in one direction are periodic while there is no continuous line in other direction; hence, the geometries of “chessboard” turn mostly parallelogram and trapezoid. Based on similarities between different geometry pattern, the RVE was designed as shown in Fig. 4-3.

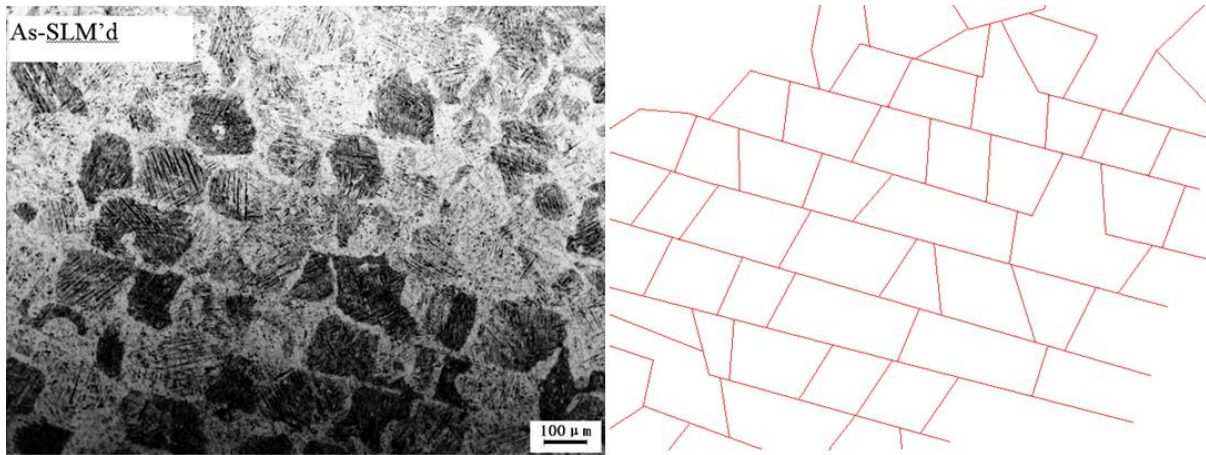


Figure 4-2 BSE image of 67° hatch angle scanned (left) and simplified outline (right).

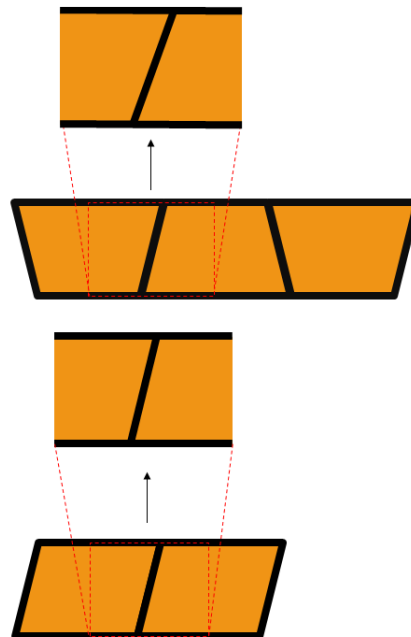


Figure 4-3 Trapezoidal and parallelogram pattern "chessboard" RVE generation.

4.2.2 Parametric Study

As shown in Fig. 4-4, in the simulation a displacement of 3 μm was applied on the upper edge of an RVE while the corresponding boundary constraints were set on both the left and bottom edges.

In an RVE, there are two components of material which represent the as-fabricated SLMed Ti64 of different microstructures within matrix and interface. The parameters a and b represent the width of inner-grid and grid-lines as marked in the schematic illustration. In 67° hatch scanned pattern, the parameters investigated include four parameters (i.e. geometry size in two directions: width and length of an RVE; thickness of interface area; the acute included angle of neighbouring two sides).

Under applied displacement the reactions which were assumed as plastic deformation without hardening in transverse directions under plane strain condition were simulated by computer. The mechanical properties were calculated in the simulation. Young's modulus and yield strength of the RVE obtained can be treated as the Young's modulus and yield strength of the alloy at macroscopic scale.

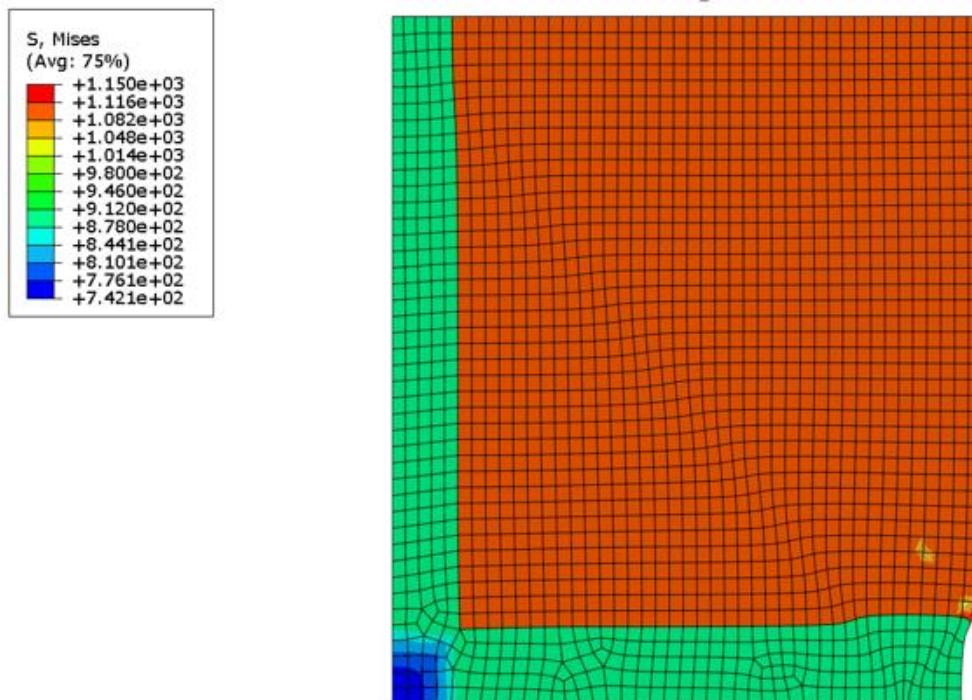


Figure 4-4 Example deformed RVE in FEA.

With the displacement of top edge and sum of reaction force of bottom edge plotted, the stress-strain curve can also be plotted. Then the elastic modulus of the RVE is calculated as follows:

Under plane strain condition,

$$\varepsilon_{zz} = 0 \quad (4-1)$$

According to Hooker's law:

$$\varepsilon_{zz} = \frac{\sigma_{zz}}{E} - \frac{\nu}{E}(\sigma_{xx} + \sigma_{yy}) \quad (4-2)$$

$$\varepsilon_{yy} = \frac{\sigma_{yy}}{E} - \frac{\nu}{E}(\sigma_{xx} + \sigma_{zz}) \quad (4-3)$$

As illustrated in RVE:

$$\sigma_{xx} = 0 \quad (4-4)$$

$$\gg E = (1 - \nu^2) \cdot \frac{\sigma_{yy}}{\varepsilon_{yy}} \quad (4-5)$$

And the yield strength was derived as for Von Mises Stress:

$$\sigma_{eq} = \left[\frac{\sigma_{yy}^2 + (1-\nu)^2 \sigma_{yy}^2 + \nu^2 \sigma_{yy}^2}{2} \right]^{1/2} \quad (4-6)$$

Then the yield stress can be derived as:

$$\sigma_y = \left[\frac{1 + (1-\nu)^2 + \nu^2}{2} \right]^{1/2} \sigma_{yy}^c = [1 - \nu + \nu^2]^{1/2} \sigma_{yy}^c = 0.89 \sigma_{yy}^c \quad (4-7)$$

In this parametric study, the mechanical properties of the RVE can be described as the function of the yield strength of Material A and Material B and the geometry a and b .

$$E, \sigma_y = f(a, b, \sigma_{ya}, \sigma_{yb}) \quad (4-8)$$

Table 4-1 Parameters range in 90° hatch scanned model.

Parameter	Min.	Max.	Nominal	Ref.
$a+b$ (μm)	140	180	160	*Experiments
b (μm)	0	50% Track Width	18	*Experiments
σ_{ya} (MPa)	938	1195	1100	[54, 27]
σ_{yb} (MPa)	862	974	900	[54, 55]

On the level of 67° hatch scanned model, a slightly different RVE underwent loading hence deformation, as illustrated in Fig. 4-5 where x and y were set as loading directions separately (left and right). In addition, geometry parameters range and nominal values were measured from provided microstructure in Table. 4-2, while material properties input was the same with the 90° hatch scanned case in Table. 4-1.

Table 4-2 Parameters range in 67° hatch scanned model.

Parameter	Min.	Max.	Nominal	Ref.
l (μm)	34.3	160.5	83.2	Fig. 4-2
w (μm)	127.1	162.4	143.0	
t (μm)	5.1	19.2	9.8	
α (°)	57.6	88.2	75.4	

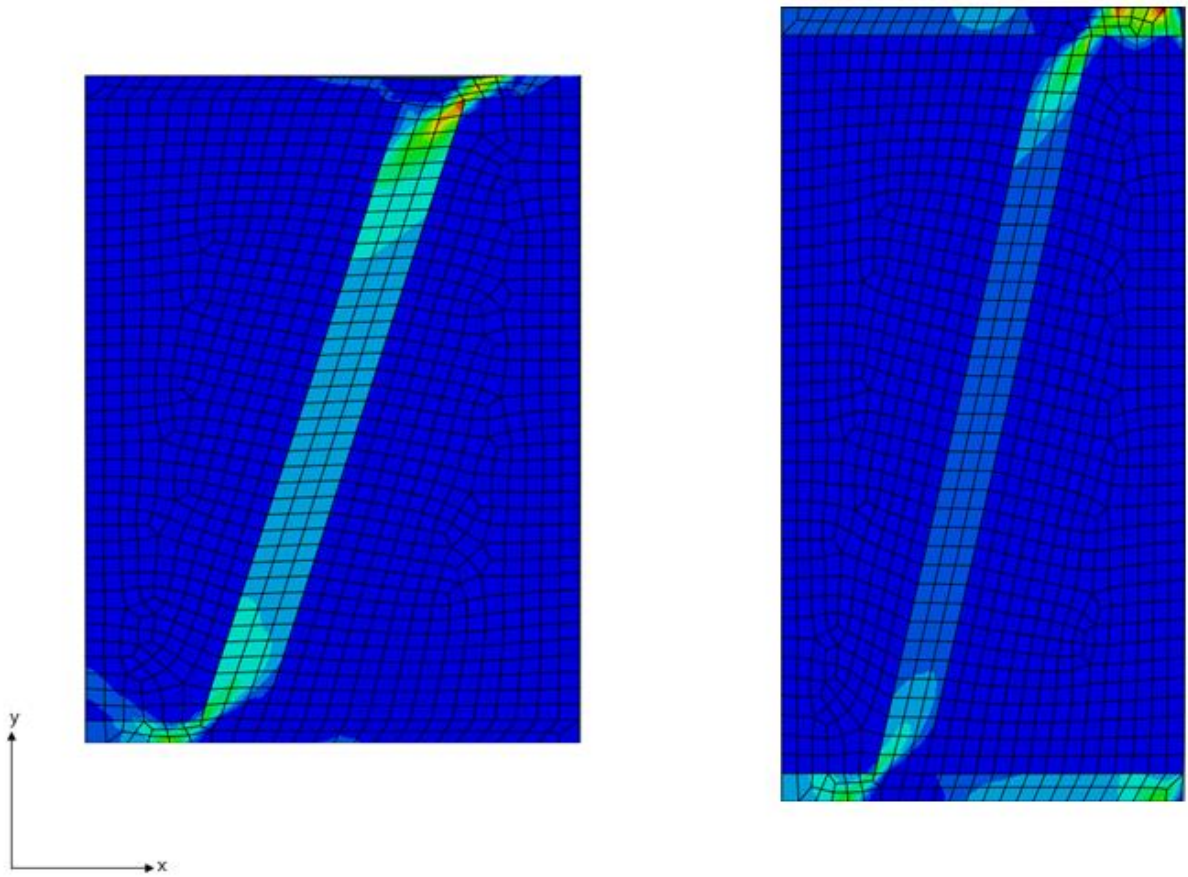


Figure 4-5 Example deformed RVE under x (left) and y (right) direction loading.

4.3 Results and Discussion

4.3.1 Influence of Interface Thickness

Firstly, the effect of parameter b (interface thickness) on the mechanical properties of the RVE was evaluated with other parameters set as nominal values. Generally, the values of the mechanical properties of the RVE material, including tensile yield strength and Young's modulus, were measured as somewhere between the two property values of two interface and matrix microstructures. The changes of Young's modulus and yield strength in the material due to the variation of the interface thickness b are simulated and plotted in Fig. 4-6 and 4-7, respectively. With fixed grid size, the yield strength of the RVE decreases linearly as interface thickness b is increased as illustrated in Fig.4-7, while Young's modulus decreases slightly about 8% as shown in Fig. 4-7. Meanwhile, the comparison of different hatch sizes ($a+b$) shows that the lower the matrix area is, the more decreasing effect will interface thickness will cause.

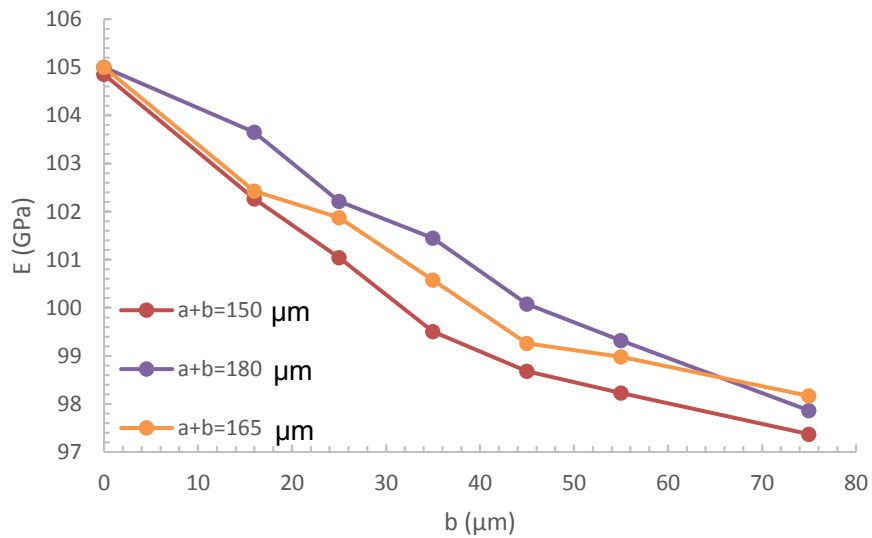


Figure 4-6 RVE's Young's modulus changes with interface thickness b (hatch angle= 90°).

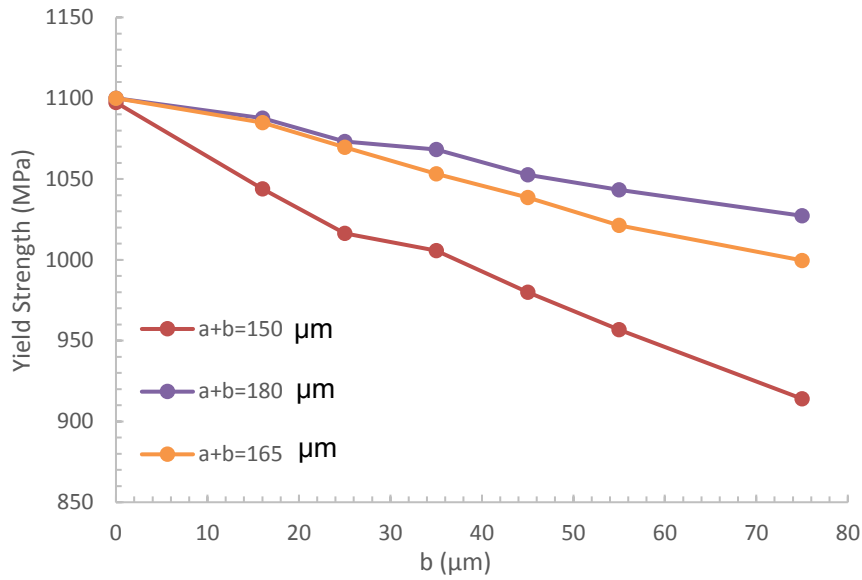


Figure 4-7 RVE's yield strength changes with interface thickness b (hatch angle $=90^\circ$).

The interfacial area thickness generated in the RVE is primarily dependent on overlapping area of neighbouring melt pools. The values for interface thickness measured from Fig. 4-2 ranged between $5.1 \mu\text{m}$ and $19.2 \mu\text{m}$. Fig. 4-8 and 4-9 show the comparison of all tested values lying between the maximum and minimum for both x-axis and y-axis loading, respectively.

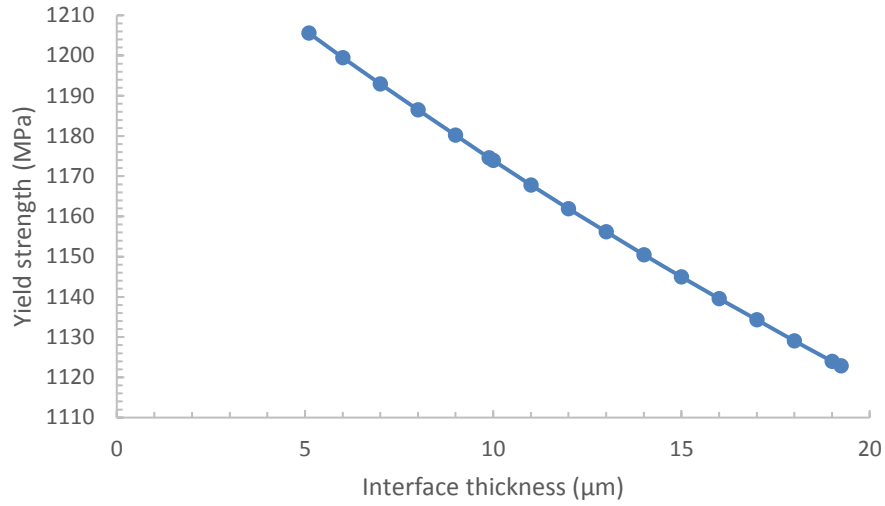


Figure 4-8 RVE's yield strength changes with interface thickness b under x-axis loading (Average RVE angle $=75.458^\circ$).

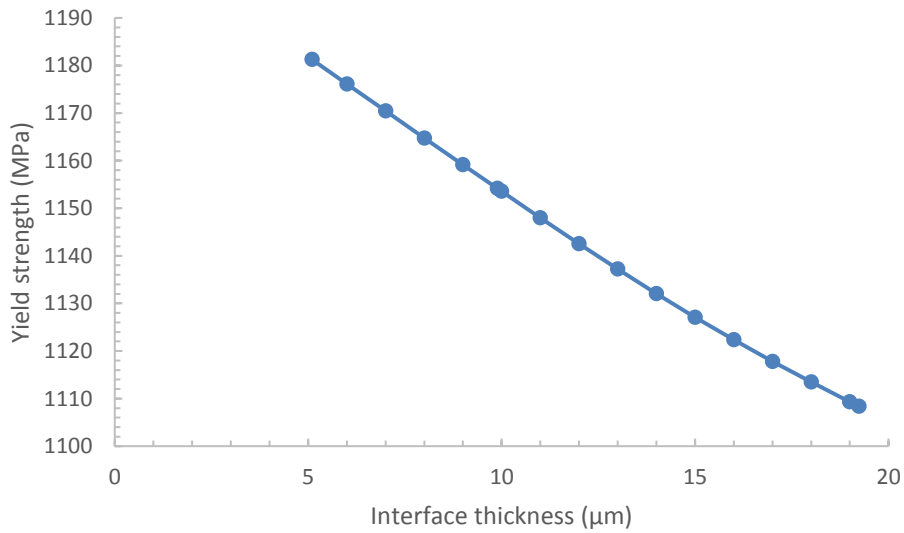


Figure 4-9 RVE's yield strength changes with interface thickness b under y-axis loading (Average RVE angle $=75.458^\circ$).

The highest point for both Fig.4-8 and 4-9 is the smallest interfacial area. It appears that the yield strength almost linearly decreases as the interface thickness is increasing as the interface

composition is set a smaller strength value. This observation shows that as the overlapping area of neighbouring melt pools decreases the SLMed strength will increase. Therefore, it may be predicted that if the interface area is to reach 0 the SLMed material will be made with the highest strength. It is unknown whether the strength will exponentially increase if a scan were to approach an overlapping area of almost 0 μm . The maximum, minimum and average values for yield stress and Young's modulus can be found in Table 4-3 and 4-4.

Table 4-3 Yield stress values due to change in interface thickness.

	Maximum	Minimum	Average
X-Axis Loading	1205.62 MPa	1122.87 MPa	1161.44MPa
Y-Axis Loading	1181.26 MPa	1108.37 MPa	1142.23MPa

Table 4-4 Young's modulus values due to change in interface thickness.

	Maximum	Minimum	Average
X-Axis Loading	111.54 GPa	103.88 GPa	107.45 GPa
Y-Axis Loading	112.63 GPa	105.68 GPa	108.92GPa

4.3.2 Influence of Matrix Area

With the size of b fixed and the nominal Young's modulus and yield strength of the two areas applied, Young's modulus of the RVE increases insignificantly as parameter a increases in Fig. 4-10, while the yield strength of the RVE appears with a more broadened increasing scope in Fig. 4-11. Still, the properties values of the RVE stay between interfacial area and matrix area properties.

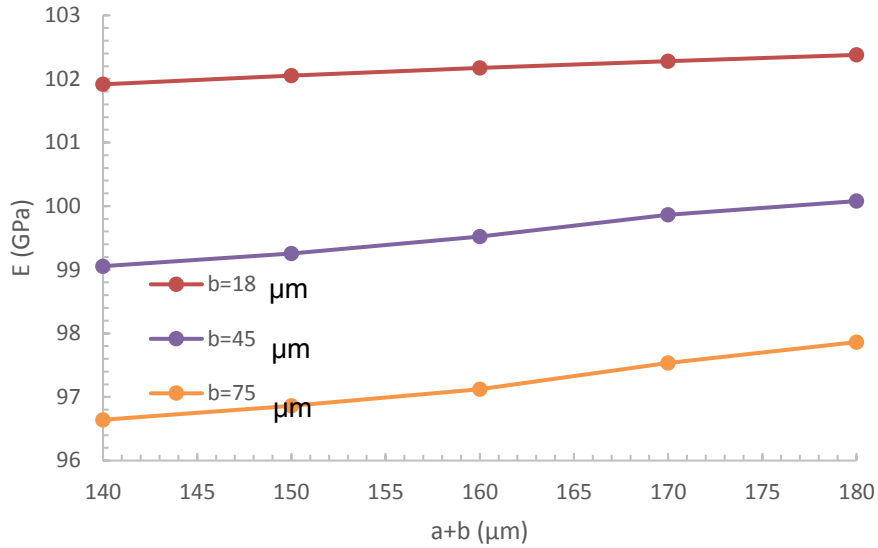


Figure 4-10 RVE's Young's modulus E changes with matrix side length a (hatch angle=90°).

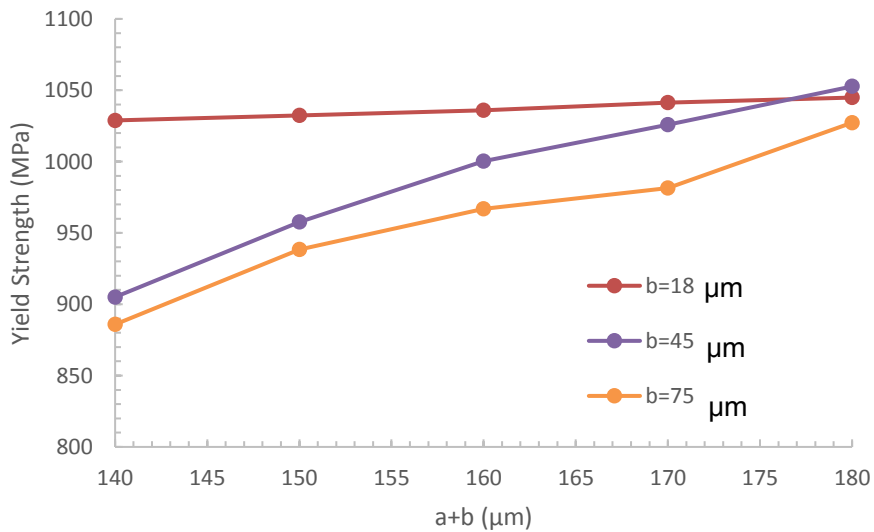


Figure 4-11 RVE's yield strength changes with matrix side length a (hatch angle =90°).

Changing width and length generated in the RVE are dependent on the hatch space, i.e. the distance between neighbouring laser beams. The values for changing width and length ranged from 127.118 μm to 162.404 μm, and 34.366 μm to 160.59 μm respectively according to the illustration of

microstructures in Fig.4-2. The Fig. 4-12, 4-13, 4-14, and 4-15 describe the strength changing along with the matrix width/length growing under x/y directions loading.

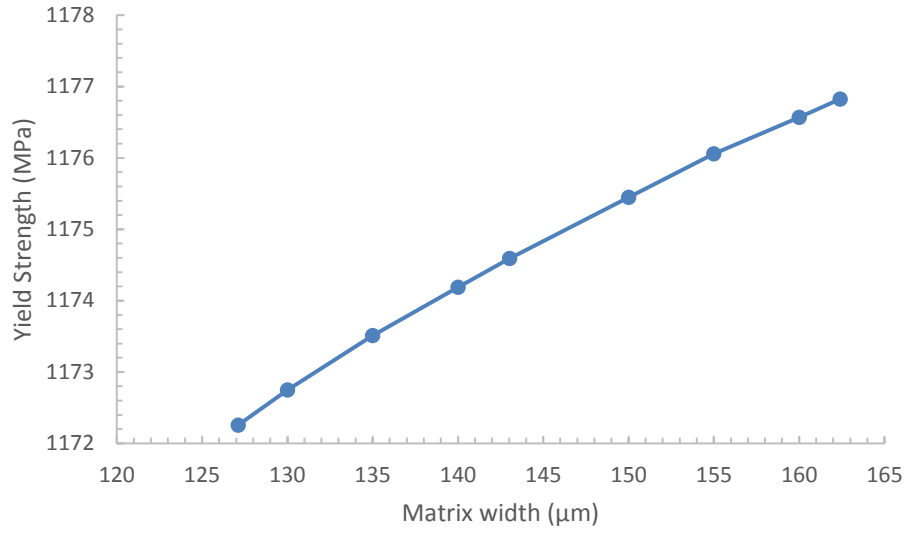


Figure 4-12 Yield stress for alternating matrix width under x-axis loading (Average RVE angle =75.458°).

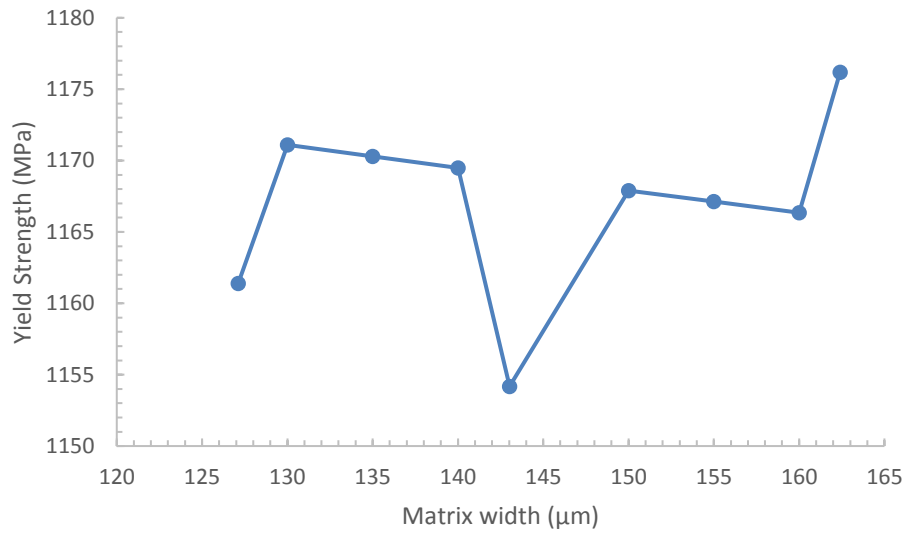


Figure 4-13 Yield stress for alternating matrix width under y-axis loading (Average RVE angle =75.458°).

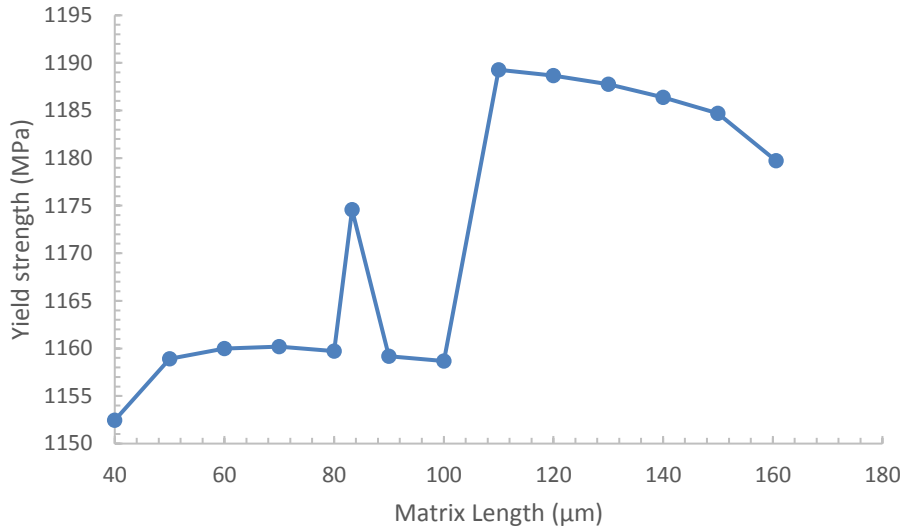


Figure 4-14 Yield strength for alternating matrix length under x-axis loading (Average RVE angle =75.458°).

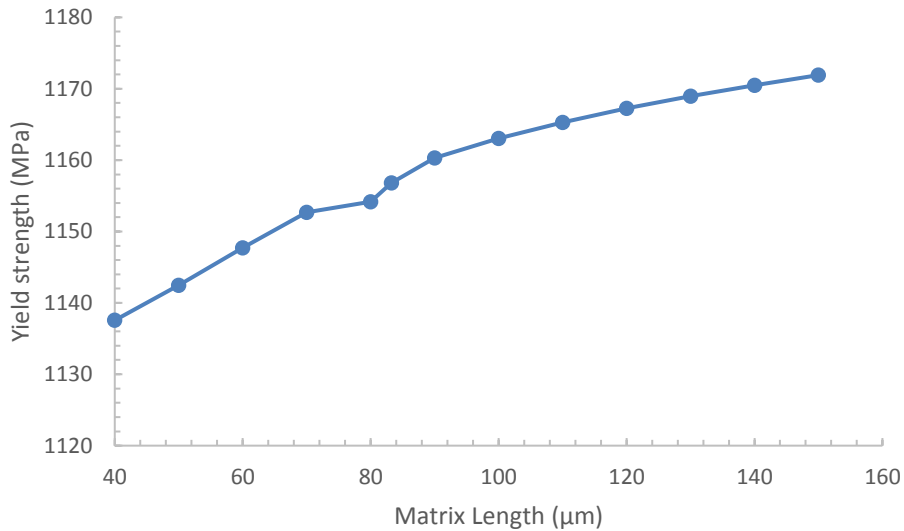


Figure 4-15 Yield strength for alternating matrix length under y-axis loading (Average RVE angle =75.458°).

The graphs show that the width of the inner matrix does not have as much of an impact on yield stress and on Young’s modulus, as compared to the length. Besides, the yield strength will also have an almost linearly increasing trend as the same direction of matrix geometry size grows. The maximum, minimum and average values of yield stress and Young’s modulus can be found in

Tables 4-5 to 4-8 below.

Table 4-5 Yield strength values due to change in width of matrix.

	Maximum	Minimum	Average
X-Axis Loading	1176.82 MPa	1172.25 MPa	1174.68 MPa
Y-Axis Loading	1176.19 MPa	1161.39 MPa	1167.11 MPa

Table 4-6 Young's modulus values due to change in width of matrix.

	Maximum	Minimum	Average
X-Axis Loading	108.87 GPa	108.45 GPa	108.67 GPa
Y-Axis Loading	96.13 GPa	125.84 GPa	109.15 GPa

Table 4-7 Yield strength values due to change in length of matrix.

	Maximum	Minimum	Average
X-Axis Loading	1189.27 MPa	1152.45 MPa	1161.49 MPa
Y-Axis Loading	1171.91 MPa	1124.92 MPa	1146.71 MPa

Table 4-8 Young's modulus values due to change in length of matrix.

	Maximum	Minimum	Average
X-Axis Loading	212.77 GPa	57.78 GPa	113.94 GPa
Y-Axis Loading	111.74 GPa	96.98 GPa	109.34 GPa

4.3.3. Influence of Material Strength

Under the consideration that the yield strength of components may vary if the parameters or source of material changed, the magnitude of yield strengths of interfacial area and matrix area were set as variables, respectively. In addition, different volume fractions of two components were simulated.

With fixed grid size and volume fraction of interfacial area and matrix area, the yield strength increases when σ_{ya} or σ_{yb} increases; when the volume fraction of matrix area is much higher than that of interfacial area, the significance of σ_{ya} is higher as compared in Fig. 4-16 and 4-17. On the other side, when the volume fraction of material B is increased much more, the influence of σ_{yb} is shown to be much higher, as illustrated in Fig. 4-18 and 4-19.

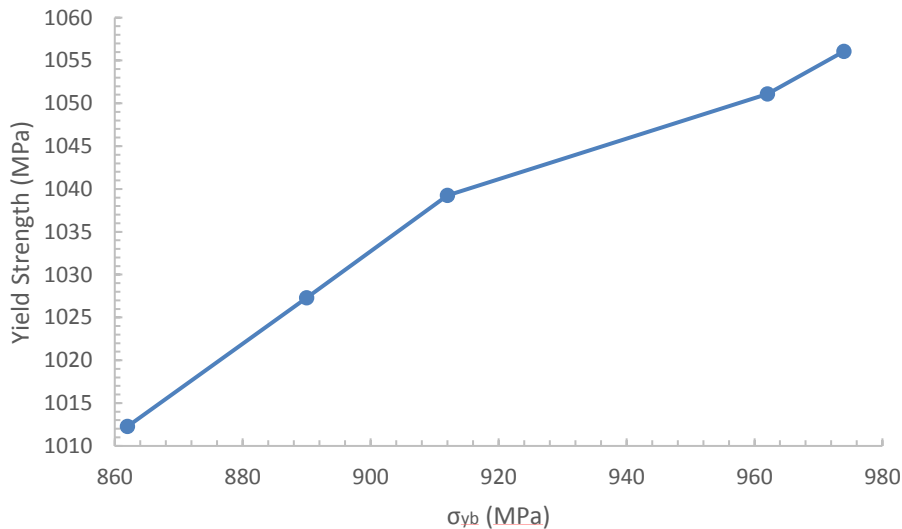


Figure 4-16 RVE's yield Strength of composites changes with yield strength of Material B when $a=150\mu\text{m}$, $b=18\mu\text{m}$.

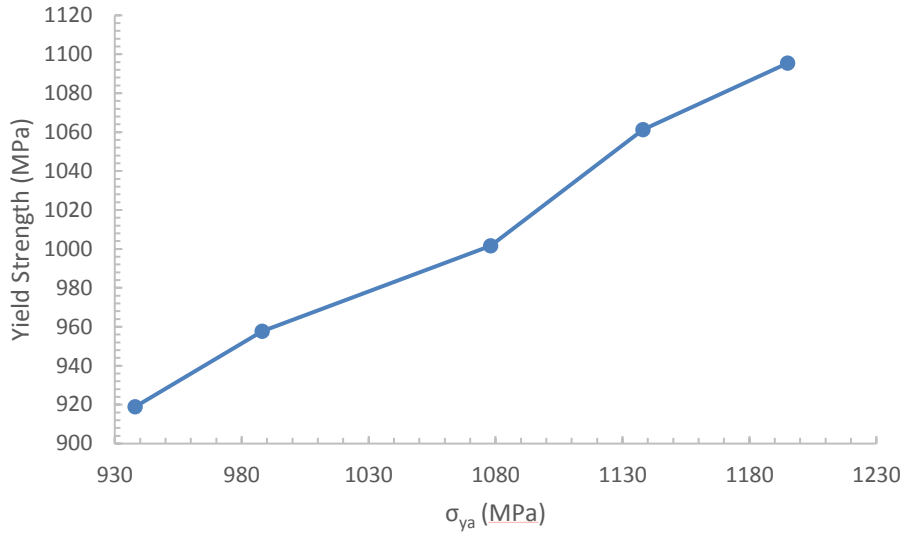


Figure 4-17 RVE's yield strength of composites changes with yield strength of Material A when $a=150\mu\text{m}$, $b=18\mu\text{m}$.

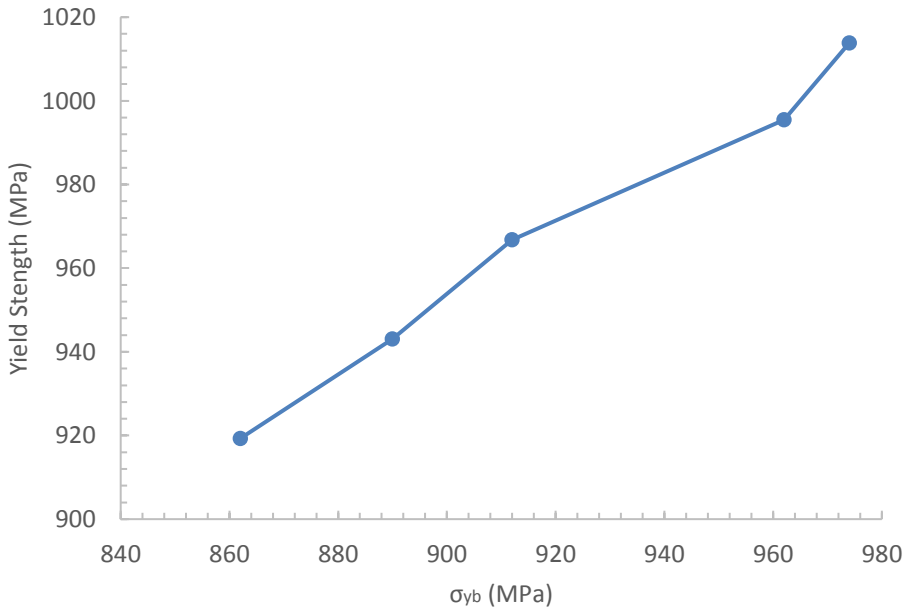


Figure 4-18 RVE's yield strength of composites changes with yield strength of Material B when $a=150\mu\text{m}$, $b=55\mu\text{m}$.

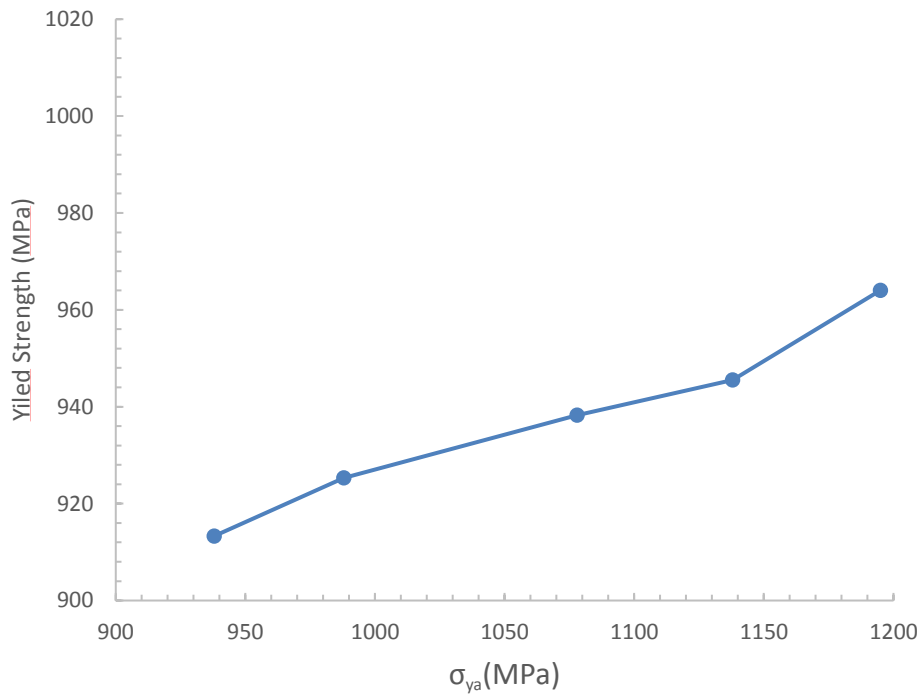


Figure 4-19 RVE's yield strength of composites changes with yield strength of Material A when $a=150\mu\text{m}$, $b=55\mu\text{m}$.

With available process parameters applied, the geometry size of interfacial area will stay within 10-20 μm . According to the results of previous studies above, the yield strength of SLMed Ti64 produced by similar conditions, for example 1115 MPa from P. Kumar's work [43], the prediction of yield strength remains on a reasonable level.

4.3.4 Influence of Hatch Angles

The angle between the interfacial area and the bottom of matrix area generated in one RVE is dependent on the hatch angle of the process parameters. The angle can range from 0° to 90° as going past 90° is providing actually the same but mirrored RVE. The angles measured from 67° hatch angled SLMed Ti64 microstructures in the feature “check” ranged from 57.6° to 88.2° . For research purposes a 0° and a 90° angles were included as the upper and lower limits in order to see the full range of possible yield strengths. Fig. 4-20 and 4-21 show the minimum and maximum angle diagrams in Abaqus along with their plastic deformation. Fig. 4-22 and 4-23 compare the effects of yield stress from the changes of angle due to both sides of axial loading.

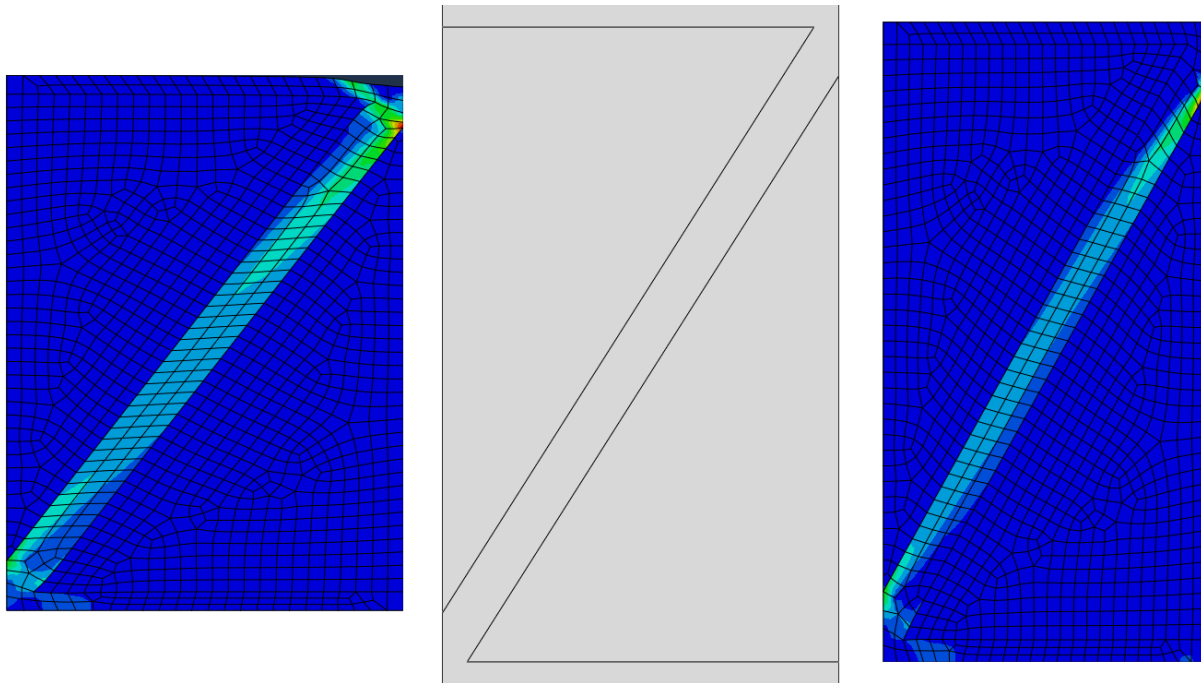


Figure 4-20 Min. angle 57.604° RVE model with x-axis (left) and y-axis (right) loading.

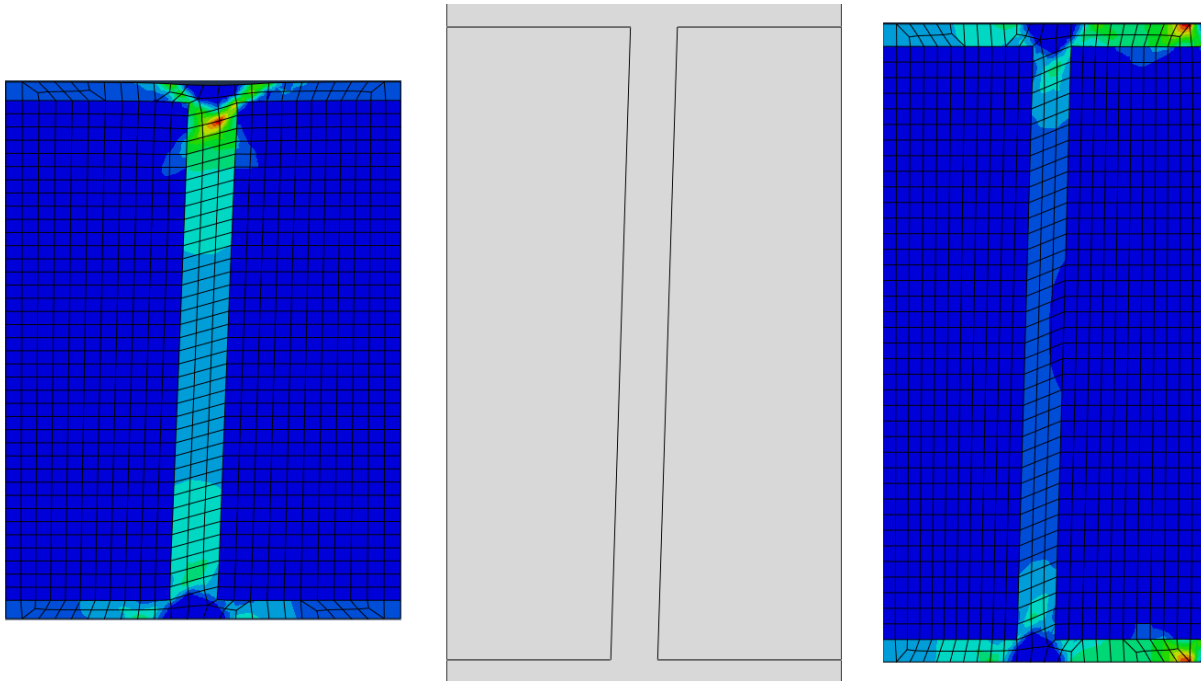


Figure 4-21 Max. angle 88.21° RVE model with x-axis (left) and y-axis (right) loading.

The above figures illustrate that the location of maximum plastic strain and deformation moves with the location where the interfacial area intersects with x-axis loading, while both stay relatively close to the top right corner and do not follow the interfacial area intersection with y-axis loading.

Fig. 4-22, and 4-23 show a clear increase in yield strength as the chessboard pattern angle changes from 0° to 90°. As the angle approaches 0° the scanning strategy approaches parallel scanning with zero rotation in neighbouring layers, meaning that the SLMed material is weaker when the scan rotates less for the next layer. The strongest possible SLMed material can be achieved at a scanning hatch angle of 90°, which means that when the scanning hatch angle is higher, the part gets stronger. It is important to note that the increase in strength due to the change in this angle is not linear, and it appears to be asymptotic as it approaches 90°.

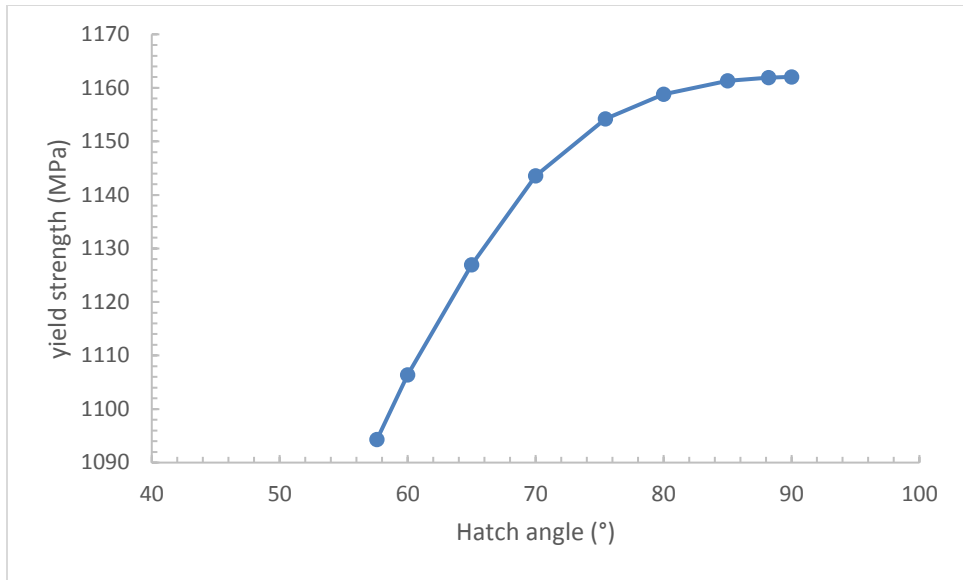


Figure 4-22 Yield strength for changing hatch angle with y-axis loading.

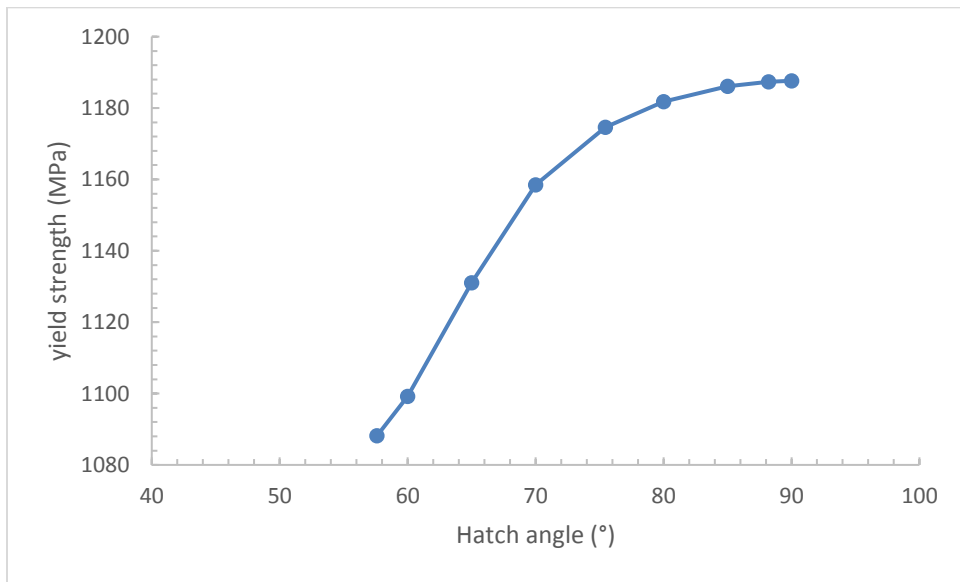


Figure 4-23 Yield strength for changing hatch angle with x-axis loading.

The maximum, minimum and average values for yield stress and Young's modulus can be found in tables below.

Table 4-8 Yield strength values due to change in angle.

	Maximum	Minimum	Average
X-Axis Loading	1187.63 MPa	1088.16 MPa	1154.93 MPa
Y-Axis Loading	1162.05 MPa	1094.32 MPa	1141.05 MPa

Table 4-9 Young's modulus values due to change in angle.

	Maximum	Minimum	Average
X-Axis Loading	109.87 GPa	100.67 GPa	106.85 GPa
Y-Axis Loading	110.80 GPa	104.34 GPa	108.80 GPa

4.4 Summary

This Chapter aimed to predict the material properties of selective laser melted Ti-6Al-4V produced with different scanning strategies. Research on the topic was conducted to provide a quantitative prediction of material properties by designing an RVE based on previous microstructural characterization. Abaqus was applied to run this FEA as there were a series of parameters to be considered. They are length/width of interface/matrix area, material properties, and “chessboard” angle. The results showed that in order to obtain an optimal SLMed Ti64, a sufficiently high hatch angle to increase the “chessboard” angle is necessary. At the maximum hatch angle, 90° is reached where the mesostructure will be mirrored. The hatch spacing also needs to be set large to allow small thickness of interface and a large size of matrix area. On the interface and matrix properties level, local mechanical characterization is required and will be studied. The results will be presented in the next Chapter.

5. Binary Microstructures Properties Measurement

5.1 Introduction

The difference in microstructural features between binary microstructures leads to the prediction of different mechanical properties within SLMed Ti64. However, a lack of relevant study made the prediction and improvement of properties based on the binary microstructures hard; hence, this characterization of the binary microstructures mechanical properties was carried out.

As observed in microscopy combined with possible formation theory, the acicular martensite is finer in the interfacial area than in the matrix area. Taken grain size strengthening theory into consideration [56], the strength of the interfacial area is supposed to be higher than that of the matrix area. In order to measure the mechanical properties in the interfacial area at a scale of 10 μm , nanoindentation is used. According to the geometry type of indenter applied, with load versus displacement curve obtained from nanoindentation experiment, hardness and Young's modulus of a local specific microstructure can be calculated [47, 48]. In this case, instrumented nanoindentation method was used to measure hardness of two types of microstructures within SLMed Ti64 [51].

In this study, binary microstructures in SLMed Ti64 were investigated in terms of morphology, and local properties such as nanohardness and elastic modulus. Residual stress influence was measured as well. Due to typical hardness measurement scale in conventional Ti64 [57] cannot realise characterisation in the binary microstructures, nanoindentation was carried out on this SLMed Ti64.

5.2 Methodology and Materials

5.2.1 Sample preparation

The sample fabrication was similar to the Chapter 3. The size of nanoindented samples were in dimension of $1 \times 1 \times 1 \text{ cm}^3$. To determine the effect of residual stress on the nanohardness, 2 samples were cut in two different orientations and stress relieved at 650°C for 1 hour and furnace cooled, followed by hardness tests at positions away from outer surface.

5.2.2 Microscopy characterisation

Characterisation of microstructures was carried out by EBSD function in a Jeol-7001F SEM. All samples surfaces were machined with a 4000-P SiC abrasive sandpapers finish and polished by $1 \mu\text{m}$ diamond suspension, following by an 85 vol% oxide polishing suspension on MD-Chem plate of polishing. The step size b EBSD function is around $0.5 \mu\text{m}$. In addition, software AZ-tec was used to analyse EBSD signal and obtain the figure and legend. For lamellar width measurement, the linear intercept method was applied (ASTM E112-12).

5.2.3 Nanoindentation test

Nanoindentation test was carried out on Keysight G200 Nanoindeter equipped with a pyramid diamond tip with triangle base (Berkovich type) [58]. Calibration of indenter tip area function was conducted on a fused silica standard sample.

On the sample in the horizontal plane, which is perpendicular to the building direction, the indent locations were manually placed under optical microscopy equipped within nanoindenter: 62 indentations in interfacial area and 50 indentations in matrix area with 1000 nm indentation depth; 50 indentations in interfacial area and 32 indentations in matrix area with 200 nm indentation depth. On the sample in the vertical plane, which is parallel to the building direction, 4 10×4 indentation matrices of 1000 nm depth and 4 small matrices of 200 nm depth were performed since the microstructures were not visible under optical microscopy in the plane along this direction. Correspondingly, large and small indents with size of $2.9 \mu\text{m}$ and $0.6 \mu\text{m}$, respectively, were

obtained from the two different indentation depths. The indentation test with 200 nm depth was designed to increase the accuracy of indentation positions on targeted area. All results were taken from stable region of the whole hardness measurement.

With Continuous Stiffness Measurement (CSM) applied and maximum depth controlled, Vickers hardness and elastic modulus were determined using the Oliver and Pharr method from the measured indentation load versus indentation depth curve [51, 59].

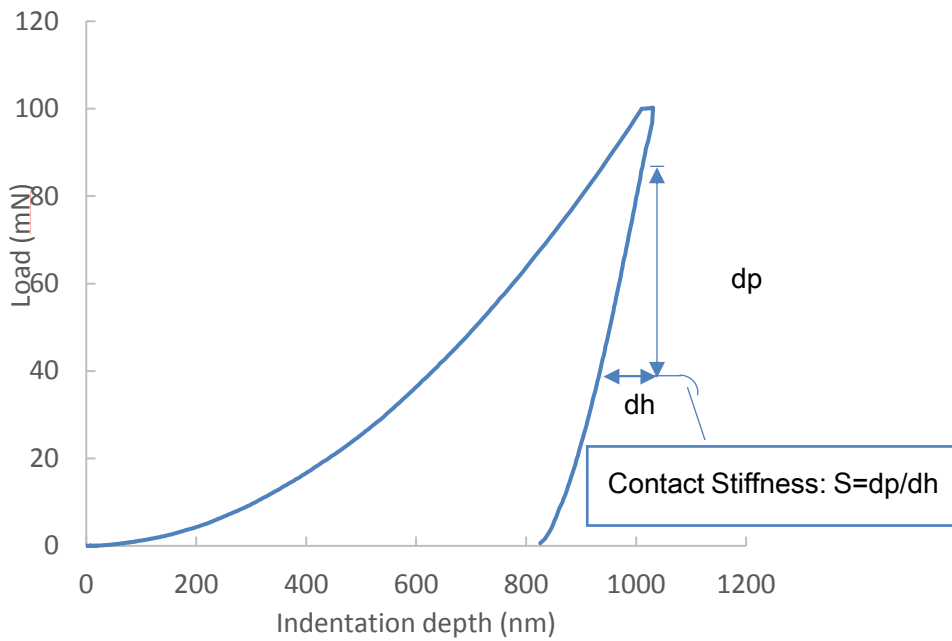


Figure 5-1 Load-Indentation depth curve in Oliver-Pharr method

The Oliver-Pharr method is briefly outlined here. This method derived from fitting the unloading curve according to power law relation as below:

$$P = B(h - h_f)^m \quad (5-1)$$

Where P represents the indentation load, h represents the displacement, B and m are the fitting parameters, and h_f is the final displacement after complete unloading calculated from curve fitting. The hardness is obtained as the maximum load divided by the projected contact area as stated:

$$H = P/A \quad (5-2)$$

The projected contact area A is defined as:

$$A = \pi(h_c \tan\theta)^2 \quad (5-3)$$

where h_c is contact depth, which is determined from the maximum indentation depth h_{max} and the contact stiffness S by:

$$h_c = h_{max} - \varepsilon \frac{P_{max}}{S} \quad (5-4)$$

where P_{max} is the maximum indentation load, and ε is a constant referring to indenter geometry, in this case, it is 0.75 for a Berkovich indenter.

The contact stiffness S can be derived from the linear section of unloading curve since the rate of load changing with displacement determines the material stiffness which is defined as the slope of the unloading curve at the maximum indentation depth:

$$S = \frac{\delta P}{\delta h} = mB(h_{max} - h_f)^{m-1} \quad (5-5)$$

Reduced elastic modulus, which is the response combined by the indenter tip and the sample material, can be calculated as:

$$E_r = \frac{\sqrt{\pi} \cdot S}{\beta \cdot 2\sqrt{A}} \quad (5-6)$$

Where β means the tip's geometric factor, for Berkovich indenter the value of β is 1.034.

With indenter properties characterized, the Young's modulus of sample can be calculated automatically from the equipment via following equation:

$$E_r = \left(\frac{1-v_s^2}{E_s} + \frac{1-v_i^2}{E_i} \right)^{-1} \quad (5-7)$$

Where v_s and v_i are Poisson's ratios of the specimen and the indenter, respectively, and E_s and E_i are the corresponding Young's modulus. [60, 61]

5.2.4 Microhardness test

The microhardness test was performed by using Duramin A300 hardness tester with 1kg loads to obtain microhardness. Each sample was indented 9 times and all indents were strictly kept near the centre point of the testing surface. The surface was ground to remove all contaminates prior to the microhardness test.

5.2.5 Nanoindents Positions

In order to illustrate nanoindentation positions on different microstructures, EBSD images were taken on nanoindented sample surface at both horizontal and vertical planes as shown in Fig.5-2, Fig.5-3, and Fig. 5-4. It can be observed that a 1000 nm depth indent may cover a number of grains in various orientations while a 200 nm depth indent may cover only a few. This may lead to slightly a higher scatter in hardness of 200 nm depth indentation.

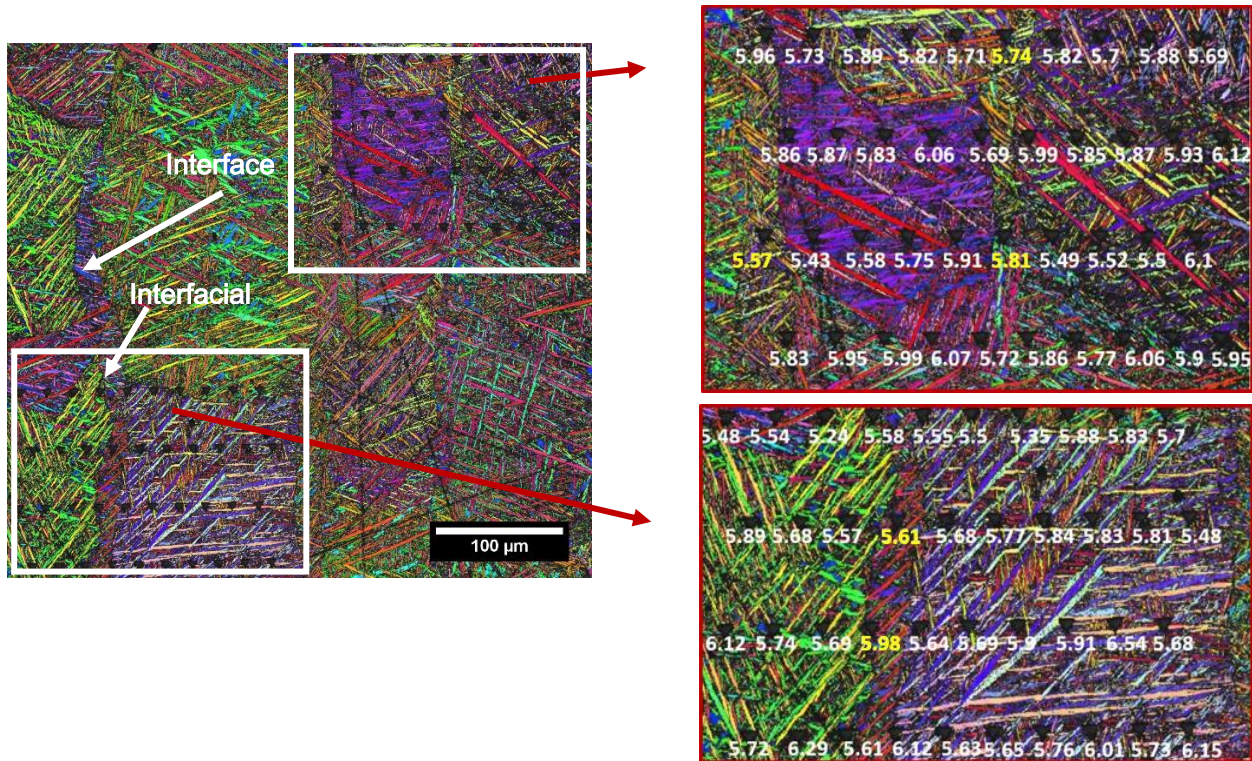


Figure 5-2 EBSD IPF-X map of 1000 nm nanoindentation on vertical sample surface (Interfacial area indicated by arrow) Magnified images of indentation areas are indicated by red arrows. (phase composition: Ti-hex 98%)

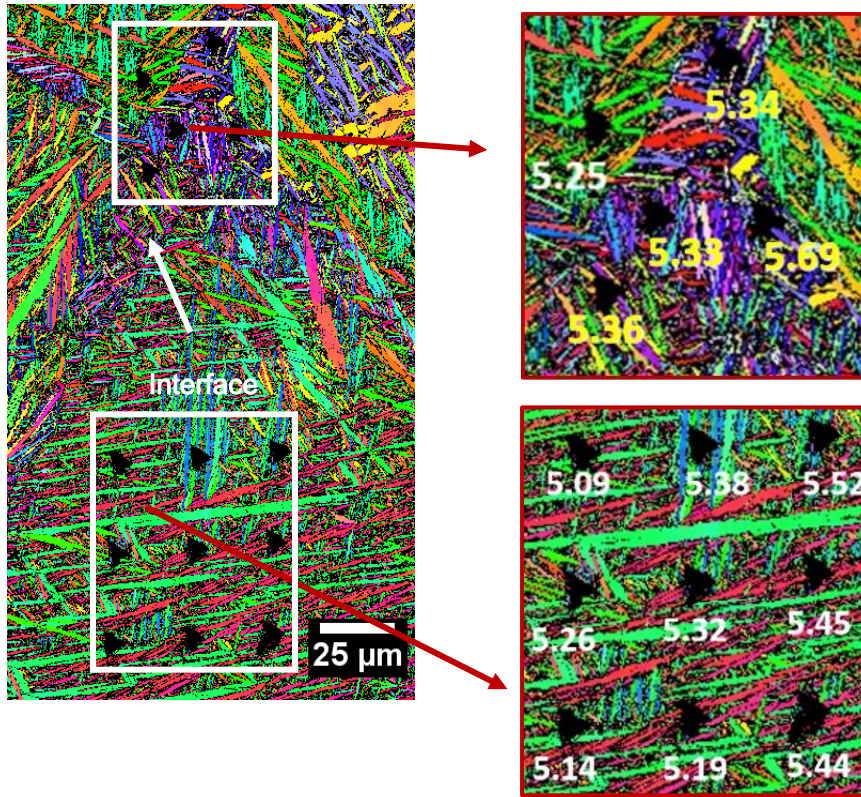


Figure 5-3 EBSD IPF-X map of 1000 nm nanoindentation on horizontal sample surface (Interfacial area is indicated right above and matrix area is shown right below) Magnified images of indentation areas are indicated by red arrows. (phase composition: Ti-hex 98%).

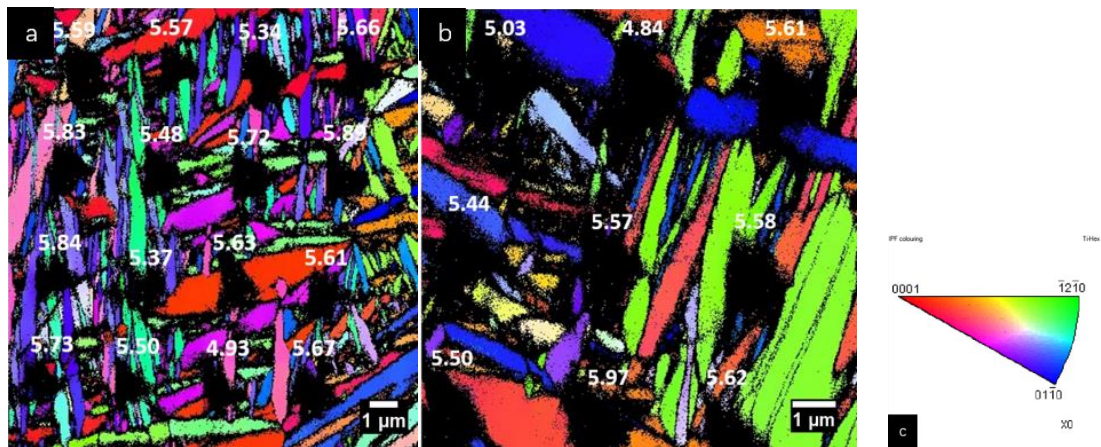


Figure 5-4 EBSD IPF-X map of 200 nm nanoindentation on horizontal sample surface in interfacial (a) and matrix (b) area; (c) legend for all EBSD IPF-X map. (phase composition: Ti-hex 95%).

Besides, the lamellar width of interfacial and matrix in horizontal plane were measured using the lineal intercept method as ASTM Standard E 112-88 described [62] of three 80 μm lines for each area and were taken into calculation: average (and standard deviation) 0.84 μm (0.2) for interfacial grains, 1.25 μm (0.3) for matrix grains.

The EBSD image of the binary microstructures in stress relieved samples as shown in Fig.5-5 showed similar result in morphology, lamellar width as well as phase composition. This indicated that the heat treatment applied is suitable to keep the microstructures features unchanged.

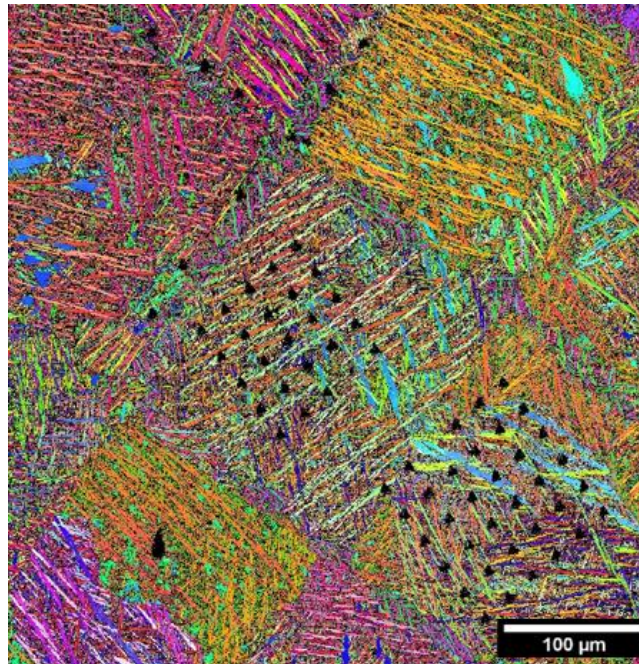


Figure 5-5 EBSD image of EBSD IPF-X map of 1000 nm nanoindentation on horizontal stress relieved sample surface. (Phase composition: Ti-hex 98%)

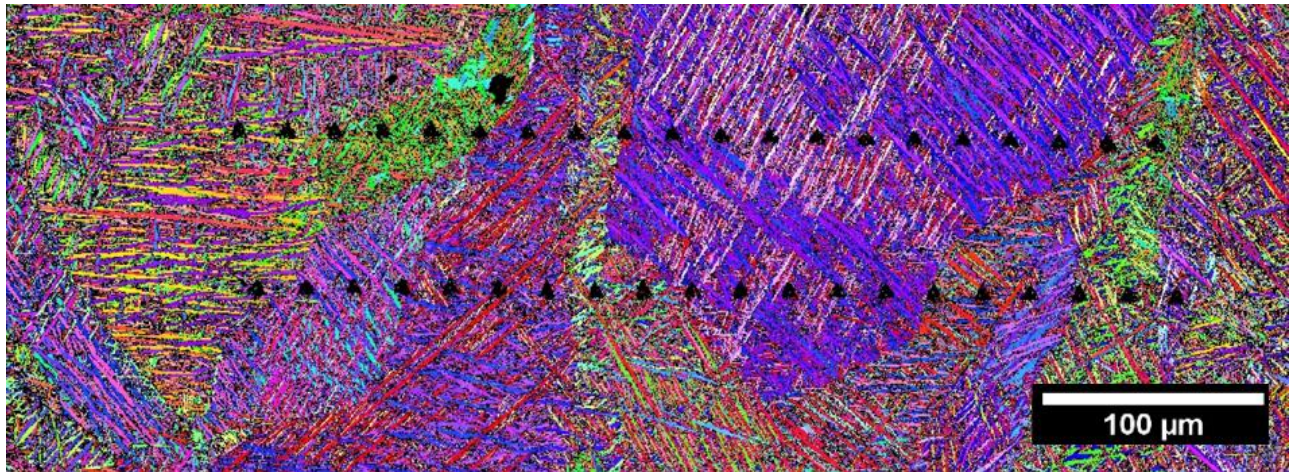


Figure 5-6 EBSD IPF-X map of 1000 nm nanoindentation on stress relieved vertical sample surface. (phase composition: Ti-hex 97%)

5.3 Modulus and Hardness Results

The elastic modulus of SLMed Ti64 from nanoindentation are average 133 GPa in 1000 nm depth, and 135 GPa in 200 nm depth. There is negligible difference between interfacial area and matrix area. Elastic modulus measurement on as-built specimens and stress relieved specimens is listed in Table 5-1

Table 5-1 Elastic modulus calculated from nanoindentation using Olive-Pharr model (AB: as-built; SR: stress relieved)

Specimens	AB-in horizontal (GPa)		AB-in vertical (GPa)	
	Interface	Matrix	Interface	Matrix
1000	133.05(2.32)	134.63(3.61)	133.61(1.68)	132.56(2.13)
200	135.74 (3.17)	134.37(2.89)	NA	135.04(2.34)

Specimens	SR-in horizontal (GPa)		SR-in vertical (GPa)	
	Interface	Matrix	Interface	Matrix
1000	138.3 (2.52)	137.47(1.80)	137.44(2.82)	136.27(1.61)
200	136.08 (2.20)	138.5(3.4)	137.03(3.41)	136.9(1.00)

As shown above, the elastic modulus shows little difference in between of interfacial area and matrix area, since in as fabricated SLMed Ti64 these two areas are mainly consisting of martensite α' Ti phase [11]. The average modulus of 130 GPa is a reasonable high value when compared to modulus of SLMed Ti64 as literature tensile data noted [14].

As listed in Table 5-2, for 1000 nm indentation depth, in horizontal plane as-built SLMed Ti64 nanohardness was measured as about 5.2 GPa in both areas, while in the other plane the value was about 5.8 GPa in both area. For 200 nm indentation depth, the nanohardness increase up to 5.6 GPa and 5.4 GPa for interfacial area and matrix area in horizontal plane, while in vertical plane only matrix nanohardness value was obtained as 6.1 GPa.

Table 5-2 Hardness calculated from nanoindentation using Olive-Pharr model (AB: as-built; SR: stress relieved)

Specimens	AB-horizontal (GPa)		AB-vertical (GPa)	
	Interface	Matrix	Interface	Matrix
1000	5.24(0.22)	5.20(0.25)	5.80(0.20)	5.76(0.21)
200	5.56(0.30)	5.42(0.29)	NA	6.09(0.28)

Specimens	SR-horizontal (GPa)		SR-vertical (GPa)	
	Interface	Matrix	Interface	Matrix
1000	5.61(0.16)	5.44(0.17)	5.60(0.23)	5.55(0.15)
200	5.6(0.29)	5.8(0.32)	5.99(0.42)	5.78(0.45)

Stress relief treatment caused about 0.2-0.4 GPa increased in horizontal direction, 0.2 GPa decreased in vertical direction. Similar trend is found in small indentation size test as well. The difference between interface and matrix keeps negligible.

Regarding hardness results, initially typical anisotropy of SLMed Ti64 can be found in the difference between vertical and horizontal plane: in vertical plane hardness was higher than in horizontal plane due to preferred orientation growth of α' grains [11].

Meantime, as mentioned in Method (Chap. 4), hardness result of 200 nm depth indents is higher than 1000 nm depth as illustrated in Fig.5-7, after 100 nm depth the hardness come stabilized. Moreover, a deep indent might cover more grains hence the hardness result may be closer to microhardness value.

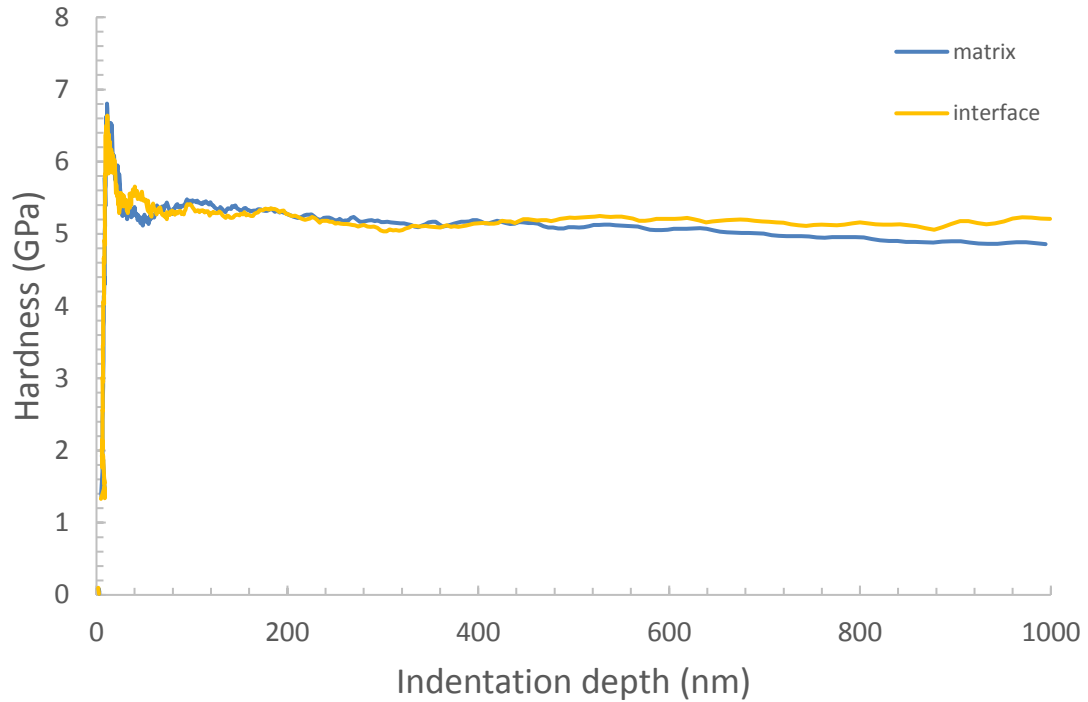


Figure 5-7 hardness-displacement curve for two indents in different area.

On the other side, the hardness of interfacial area at both planes is slightly higher than matrix area, however, with standard deviation taken into consideration, the difference is little. A deep nanoindentation size may contain the property to be tested from the area around, however, this negligible difference as shown above indicates that the 1000 nm indentation depth is sufficient for the binary microstructures characterization.

5.4 Microhardness

For purpose of detecting residual stress effect, typical indentation was carried out on stress relieved sample and as-fabricated sample at horizontal and vertical plane separately. With location of indentation centered in cubic specimen, average microhardness in GPa were calculated and listed in Table 5-3 below with standard deviation in blanket.

As summarized in Wenyi's work [63], one of the hardness result deviation from nanohardness is that SLMed Ti64 is a hexagonal material with strong texture of ultra-fine martensite as mentioned. Another possible reason is that the deformation occurred in nanoindentation tends to occur in pile-up way as compared with typical sink-in way of Oliver-Pharr method and led to a higher value than microhardness measurement with consideration of the hardness derivation as noted in methodology section.

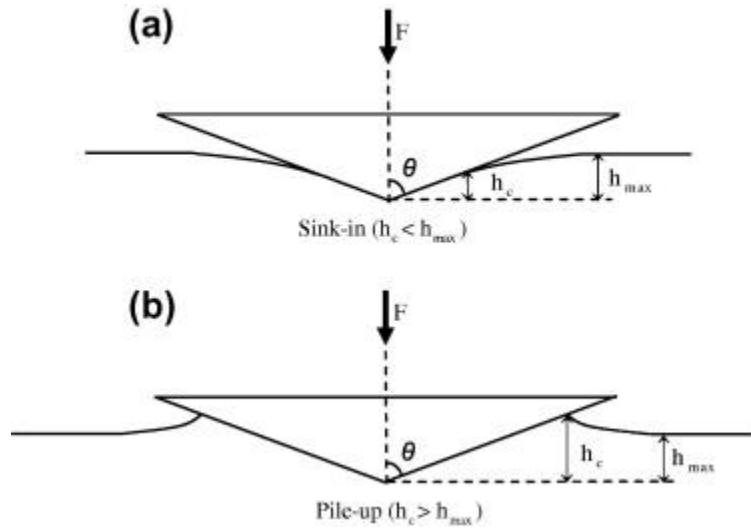


Figure 5-8 Schematics of sink-in (a) and pile-up (b). [63]

Table 5-3 Comparison of average microhardness at different plane with/without stress relief treatment

Residual stress in plane:	Horizontal	Horizontal_SR	Vertical	Vertical_SR
Microhardness(GPa)	4.45(0.06)	4.31(0.09)	4.39(0.08)	4.35(0.06)

5.5 Influence of Lamellar Width, Indentation Depth and Residual Stress

In results of nanohardness measurement, negligible difference can be found in interfacial area and matrix area. The reasons were analysed in following possible factors contributing to hardness: lamellar width of martensite, indentation depth applied in nanoindentation, and residual stress effect on hardness measurement.

5.5.1 Lamellar width effect

Hardness level relates to material strength. As Hall-Petch equation stated, yield strength depends on lamellar width as [64, 65]:

$$\sigma_y = \sigma_0 + k_1 D_{GB}^{\frac{1}{2}} \quad (5-8)$$

where σ_0 and k_1 are constants, Equation 5-9 can be used to explain the slight difference in hardness of different microstructures. In SLMed Ti64, this equation has been fitted as following [66] :

$$\sigma_y (MPa) = 664.27 + 278.04 \cdot (\text{lamellar width})^{-0.5} \quad (5-9)$$

With measured lamellar α' size of 0.8 μm and 1.3 μm applied, the yield strength can be derived as 967.64 MPa and 912.96 MPa in the interfacial and matrix area respectively, which means the difference of strength is only 5.7%. Some researchers [61] used the typical relationship $HV \approx 3\sigma_y$

to estimate yield strength from nanohardness for materials such as steel [67]. However, for materials with lamellar microstructures, such as SLMed Ti64, the hardness and yield strength rely on lamellar width at various factors and this 3-fold relationship cannot be applied. For a rough estimation, the yield strength depends on hardness as such a relationship. Sui et al [50] proposed the following relationship for similar lamellar microstructure of ($\alpha+\beta$) Ti64 (made by vacuum induction melt technology):

$$\sigma_y = 447.63 + 0.87HV \quad (5-10)$$

Using Eq. 5-10 combined with Eq. 5-9, hardness values are estimated as 597.71 HV (5.86 GPa) and 534.86 HV (5.25 GPa) for the interfacial and matrix area, respectively. Based on the calculation above, the lamellar width made slight significance on strength of this material. Also, hardness does not vary significantly according to Hall-Petch effect.

5.5.2 Indentation depth effect

With various grain orientations taken into consideration, a deep indent can give mechanical response of more grains, and different orientations will make the angle between the crystalline slip plane and applied load direction varied, which caused less fluctuation in hardness results in 1000 nm depth. In addition, as shown in Fig.5-7, the results of 200 nm and 1000 nm depth, the hardness value becomes stable at depth of 100 nm but slightly decreases and gets close to real hardness value.

As shown in result section, the hardness levels are actually very close when stabilized in deep displacement. A deeper indentation size may cover the material around more. However, this result showed the material in vicinity caused little influence the material under nanoindenter tip test region.

5.5.3 Residual stress effect

Compared with as-built specimen hardness, stress-relieved samples have about 0.2 GPa higher horizontal hardness and 0.2 GPa lower vertical value at similar positions within each sample. At this chosen centre position, residual stress hence may be different in directions at horizontal plane and vertical plane.

Moreover, the residual stress may vary from site to site in SLMed Ti64 due to local heat conduction history [68]. The overall changes of hardness caused by residual stress in both directions and areas are still quite slight due to the small geometry size in this experiment. The stress relieved samples also showed negligible difference in interfacial area and matrix area, which indicated that Hall-Petch effect is still the key factor.

Compared with nanohardness results, the overall microhardness is reasonably higher (10%-30%) due to nanoindentation using projected contact area at peak load other than typical indentation used residual projected area while former is always larger [69]. Furthermore, after stress relief, in horizontal plane SLMed Ti64 hardness slightly dropped, while in hardness of vertical plane minor change occurred, which indicated that the residual stress should be uneven at different plane and overall have small influence on hardness test due to the small geometry size of sample.

To balance, the Hall-Petch effect is the dominate factor which leads to the similar hardness level among binary areas, with proper indentation depth and few residual stress influence. Similarly, other lamellar width square related properties such as yield strength should also keep close in binary areas according to Hall-Petch effect. Besides, as phase composition in both areas provided in microscopy, the Youngs modulus stays the same. In general, nanoindentation confirmed strength similarity between interface and matrix due to Hall-Petch effect.

5.6 Summary

As measured under microscope, the lamellar width in the interfacial area is 0.84 μm , which is 33% smaller than 1.25 μm in the matrix area. However, the hardness measured by nanoindentation tests in both areas has negligible difference and stabilized at 5.6 GPa and 5.5 GPa in horizontal and vertical plane respectively (without residual stress effect). Young's modulus also was found in average of 135 GPa in both horizontal and vertical planes. According to Hall-Petch equation and the relationship between strength and hardness, the difference in lamellar width could only cause the yield strength difference of 5.6% in these two microstructural areas. This estimation by Hall-Petch equation explained the negligible difference in hardness measured by nanoindentation. Residual stress made only 3% difference on hardness result but opposite direction in horizontal and vertical plane, the overall influence is still much weaker than Hall-Petch effect.

6. Conclusion

This study focused on the featured binary microstructures in SLMed Ti64, figured out local properties of two kinds of microstructures, also investigated the influence on material properties. The results can help to determine the scanning strategy and hatch distance on the material's strength stage, which is capable to promote the material performance. Besides, they make it possible to provide useful morphological and mechanical properties of the binary microstructures, which can be investigated further to reduce limitations of the material.

Based on the mechanism of the binary microstructures occurrence in literatures, a prediction that two kinds of microstructures may be different in morphology and properties was raised. FEA job proved that the dominate microstructure will contribute more to the material on strength and elastic modulus. Microscopy demonstrated the morphology of the binary microstructure, as well as the average grain sizes of two microstructures. The nanoindentation test measured the nanohardness and elastic modulus of two microstructures which can be explained by Hall-Petch equation.

Key Findings of the thesis are listed below:

- The binary microstructures were observed under microscopy to occur periodically as interfacial/matrix area, which can form a “chessboard” mesostructure under cross-hatch scanning strategy.
- The size of a repeatable mesostructured feature in normal to building direction is equal to the hatch distance, while an interfacial area width takes only $< 20 \mu\text{m}$.
- The illustration correlates the chessboard grid to prior β grains in SLMed Ti64 in horizontal direction as well as vertical direction.
- The yield strength and elastic modulus of SLMed Ti64 depends on the corresponding mechanical properties of both areas. If the yield strength of one area remains, the yield

strength of the material will go with the yield strength of the other. This influence will be significant when the area size dominates.

- The yield strength of SLMed Ti64 can be increased by a higher hatch angle. Theoretically the maximum strength can be reached at the hatch angle of 90° .
- The average lamellar widths of martensites are $1.25\ \mu\text{m}$ and $0.84\ \mu\text{m}$ in matrix and interfacial area respectively.
- Hardness from nanoindentation test was measured as 5.6 GPa and 5.5 GPa respectively in horizontal and vertical plane and the results show negligible difference ($\sim 1\%$) between the interfacial area and the matrix area of the binary microstructures.
- Young's modulus from nanoindentation test was found about 133 GPa in both planes and microstructures.
- The lamellar width difference in the interfacial and the matrix areas could only affect the yield strength difference by 5.6% based on Hall-Petch relationship.
- Experimental results show that residual stress made only 3% difference in hardness results in horizontal plane and vertical plane.

References

- [1] M. Vaezi, "The international Journal of Advanced Manufacturing Technology," in *The international journal of advanced manufacturing technology*, vol. 67, 2013, p. 1721.
- [2] M. K. Thompson, G. Moroni, T. Vaneker, G. Fadel, R. I. Campbell, I. Gibson, A. Bernard, J. Schulz, G. Patricia, B. Ahuja and F. Martina, "Design for Additive Manufacturing: Trends, opportunities, considerations, and constraints," *CIRP Annals - Manufacturing Technology*, vol. 65, no. 2, pp. 737-760, 2016.
- [3] H. W. Kang, S. J. Lee, I. K. Ko, C. Kengla, J. J. Yoo and A. Atala, "Nature biotechnology," *Nature biotechnology*, vol. 34, p. 312, 2016.
- [4] B. Vandenbroucke and J.-P. Kruth, "Selective laser melting of biocompatible metals for rapid manufacturing of medical parts," *Rapid Prototyping Journal*, vol. 13, no. 4, pp. 196-203, 2007.
- [5] S. Bremen, a. Diatlov and w. meiners, "Selective Laser MeltingA manufacturing technology for the future?," *Laser Technik Journal*, vol. 9, no. 2, pp. 33-38, 2012.
- [6] L. Facchini, E. Magalini, P. Robotti, A. Molinari, S. Hoges and K. Wissenbach, "Ductility of a Ti-6Al-4V alloy produced by selective laser melting of prealloyed powders," *Rapid Prototyping Journal*, vol. 16, no. 6, pp. 450-459, 2010.
- [7] I. Yadroitsev, M. Pavlov, P. Bertrand and I. Smurov, "Mechanical properties of samples fabricated by selective laser melting," in *14èmes Assises Européennes du Prototypages & Fabrication Rapide*, Paris, 2009.
- [8] E. Yasa, J. Deckers, J. P. Kruth, M. Rombouts and J. Luyten, "Experimental investigation of Charpy impact tests on metallic SLM parts," in *Proceedings of 4th International Conference on Advanced Research in Virtual and Rapid Prototyping*, Leiria, Portugal, 2009.
- [9] T. Vilaro, C. Colin and J. D. Bartout, "As-Fabricated and Heat-Treated Microstructures of the Ti-6Al-4V Alloy Processed by Selective Laser Melting," *METALLURGICAL AND MATERIALS TRANSACTIONS A*, vol. 42a, pp. 3190-3199, 2011.
- [10] J. Yang, H. Yu, J. Yin, M. Gao, Z. Wang and X. Zeng, "Formation and control of martensite in Ti-6Al-4V alloy produced by," *Materials and Design*, no. 108, pp. 308-318, 2016.
- [11] L. Thijs, F. Verhaeghe, T. Craeghs, J. V. Humbeeck and J.-P. Kruth, "A study of the microstructural evolution during selective laser melting of Ti-6Al-4V," *Acta Materialia*, vol. 58, no. 9, pp. 3303-3312,

2010.

- [12] M. Simonelli, Y. Y. Tse and C. Tuck, "On the Texture Formation of Selective Laser Melted Ti-6Al-4V," *METALLURGICAL AND MATERIALS TRANSACTIONS A*, vol. 45a, pp. 2863-2872, 2014.
- [13] I. Gibson, D. Rosen and B. Stucker, *Additive manufacturing technologies : 3D printing, rapid prototyping, and direct digital manufacturing*, Second edition ed., New York, NY : Springer, 2015.
- [14] J. J. Lewandowski and M. Seifi, "Metal Additive Manufacturing: A Review of Mechanical Properties," *Annual Review of Materials Research*, pp. 151-186, 2016.
- [15] H. Schlegelbaum, W. Meiners, K. Wissenbach and C. Hinke, "Individualized production by means of high power selective laser melting," *CIRP Journal of Manufacturing Science and Technology*, vol. 2, no. 3, pp. 161-169, 2010.
- [16] G. Lutjering and J. C. Williams, *Titanium*, 2nd ed., Berlin Heidelberg New York: Springer , 2007.
- [17] Granta Material intelligence, "CES EduPack," 2015.
- [18] Z. A and L. F. R, *The Science, Technology and Application of Titanium*, Oxford: Pergamon Press, 2004.
- [19] P. P. G, "The crystallography and deformation modes of hexagonal close-packed metals," *Metallurgical Reviews*, vol. 12, no. 1, p. 169, 1967.
- [20] M. H. Yoo, "Slip, twinning, and fracture in hexagonal close-packed metals," *Metallurgical Transactions A*, vol. 12, pp. 409-418, 1981.
- [21] O. H. M, *The Science, Technology and Application of Titanium*, Oxford: Pergamon Press, 1970.
- [22] P. M. and L. C., *Titan und Titanlegierungen*, Weinheim: Wiley-VCH, 2002.
- [23] L. G., H. D. and D. M, *Fatigue*, Warley,: EMAS, 1993.
- [24] L. Thijs, F. Verhaeghe, T. Craeghs, J. V. Humbeeck and J.-P. Kruth, "A study of the microstructural evolution during selective laser melting of Ti-6Al-4V," *Acta Materialia*, vol. 58, no. 9, pp. 3303-3312, 2010.
- [25] I. A. Roberts, C. J. Wang, R. Esterlein, M. Stanford and D. J. Mynors, "A three-dimensional finite element analysis of the temperature field during laser melting of metal powders in additive layer manufacturing," *International Journal of Machine Tools and Manufacture*, vol. 49, no. 12-13, pp. 916-923, 2009.
- [26] B. Vrancken, L. Thijs, J.-P. Kruth and J. V. Humbeeck, "Heat treatment of Ti6Al4V produced by Selective Laser Melting: Microstructure," *Journal of Alloys and Compounds*, no. 541, pp. 177-185, 2012.
- [27] H. K. Rafi, N. V. Karthik, H. Gong, T. L. Starr and B. E. Stucker, "Microstructures and Mechanical Properties of Ti6Al4V Parts Fabricated by Selective Laser Melting and Electron Beam Melting," *Journal*

- of Materials Engineering and Performance*, vol. 22, no. 12, pp. 3872-3883, 2013.
- [28] W. Xu, M. Brandt, S. Sun, J. Elambasseril, Q. Liu, K. Latham, K. Xia and M. Qian, "Additive manufacturing of strong and ductile Ti-6Al-4V by selective laser," *Acta Materialia*, no. 85, pp. 74-84, 2015.
- [29] C. Qiu, N. J. Adkins and M. M. Attallah, "Microstructure and tensile properties of selectively laser-melted and of HIPed laser-melted Ti-6Al-4V," *Material Science & Engineering A*, no. 578, pp. 230-239, 2013.
- [30] M.-W. Wu and P.-H. Lai, "The positive effect of hot isostatic pressing on improving the anisotropies of bending and impact properties in selective laser melting Ti-6Al-4V alloy," *Materials Science & Engineering A*, no. 658, pp. 429-438, 2016.
- [31] S. Leuders, M. Thone, A. Riemer, T. Niendorf, T. Troster, H. A. Richard and H. J. Maier, "On the mechanical behaviour of titanium alloy TiAl6V4 manufactured by selective laser melting: Fatigue resistance and crack growth performance," *International Journal of Fatigue*, vol. 48, pp. 300-307, 2013.
- [32] T. H. Becker, M. Beck and C. Scheffer, "MICROSTRUCTURE AND MECHANICAL PROPERTIES OF DIRECT METAL LASER SINTERED TI-6AL-4V," in *South African Journal of Industrial Engineering*, South Africa, 2013.
- [33] M. Thone, S. Leuders, A. Riemer and R. H. Troster, "Influence of heat-treatment on selective laser melting products – e.g. Ti6Al4V," in *Solid freeform fabrication symposium SFF*, Austin, 2012.
- [34] P. A. Kobryn and S. L. Semiatin, "Microstructure and texture evolution during solidification processing of Ti-6Al-4V," *Journal of Materials Processing Technology*, vol. 135, no. 2-3, pp. 330-339, 2003.
- [35] M. R. Daymond, R. A. Holt, S. Cal, P. Mosbrucker and S. C. Vogel, "Texture inheritance and variant selection through an hcp-bcc-hcp phase transformation," *Acta Materialia*, vol. 58, no. 11, pp. 4053-4066, 2010.
- [36] N. Stanford and P. S. Bate, "Crystallographic variant selection," *Acta Materialia*, no. 52, pp. 5215-5224, 2004.
- [37] A. A. Antonyamy, J. Meyer and P. B. Prangnell, "Effect of build geometry on the β -grain structure and texture in additive manufacture of Ti-6Al-4V by selective electron beam melting," *Materials Characterisation*, pp. 153-168, 2013.
- [38] M. Simonelli, Y. Y. Tse and C. Tuck, "FURTHER UNDESTANDING OF Ti-6Al-4V SELECTIVE LASER MELTING USING TEXTURE ANALYSIS," in *Proceedings of 23rd Annual International Solid Freeform Fabrication Symposium*, Austin, 2012.
- [39] L. Thijs, K. Kempen, J. P. Kruth and J. V. Humbeeck, "Fine-structured aluminium products with controllable texture by selective laser melting of pre-alloyed AlSi10Mg powder," *Acta Materialia*, vol. 5, no. 61, pp. 1809-1819, 2013.

- [40] M. Shunmugavel, "Machinability studies of selective laser melted titanium alloy Ti-6Al-4V," School of Engineering, Deakin University, Melbourne, 2017.
- [41] J. Zhang, X. Zhang, X. Wang, J. Ding, Y. Traore, S. Paddea and S. Williams, "Crack Path Selection at the Interface of Wrought and Wire + Arc Additive Manufactured," *Material and Design*, vol. 104, pp. 365-375, 2016.
- [42] X. Zhang, F. Martina, J. Ding, X. Wang and S. Williams, "Fracture toughness and fatigue crack growth rate properties in wire," *Fatigue & Fracture of Engineering Materials & Structures*, vol. 40, pp. 790-803, 2016.
- [43] P. Kumar, O. Prakash and U. Ramamurty, "Micro-and meso-structures and their influence on mechanical properties of selectively laser melted Ti-6Al-4V," *Acta Materialia*, vol. 154, pp. 246-260, 2018.
- [44] M. Matsumoto, M. Shiomi, K. Osakada and F. Abe, "Finite element analysis of single layer forming on metallic powder bed in rapid prototyping by selective laser processing," *International Journal of Machine Tools and Manufacture*, vol. 42, no. 1, pp. 61-67, 2002.
- [45] C. H. Fu and Y. B. Guo, "3-Dimensional finite element modeling of selective laser melting Ti-6Al-4V alloy," *Journal of Manufacturing Science and Engineering*, vol. 136, no. 6, p. 061004, 2014.
- [46] M. Zhang, J. Zhang and D. L. McDowell, "Microstructure-based crystal plasticity modeling of cyclic deformation of Ti-6Al-4V," *International Journal of Plasticity*, no. 23, pp. 1328-1348, 2007.
- [47] W. C. Oliver and G. M. Pharr, "An improved technique for determining hardness and elastic modulus using load and displacement sensing indentation experiments," *Journal of Materials Research*, vol. 7, no. 6, pp. 1564-1583, 1992.
- [48] G. M. Pharr, "Measurement of mechanical properties by ultra-low load indentation," *Materials Science and Engineering: A*, vol. 23, no. 1-2, pp. 151-19, 1998.
- [49] I. M. Hutchings, "The contributions of David Tabor to the science of indentation hardness," *Journal of Materials Research*, vol. 24, no. 3, pp. 581-589, 2008.
- [50] Y.-w. Sui, A.-h. Liu, B.-s. Li and J.-j. Guo, "Relationship between thickness of lamellar $\alpha+\beta$ phase and mechanical properties of Titanium alloy," *Advanced Materials Research*, Vols. 311-313, pp. 1916-1919, 2011.
- [51] W. C. Oliver and G. M. Pharr, "Measurement of hardness and elastic modulus by instrumented indentation: Advances in understanding and refinements to methodology," *Journal of Material Research*, vol. 19, no. 1, pp. 3-20, 2004.
- [52] H. Gong, K. Rafi, H. Gu, G. J. Ram, T. Starr and B. Stucker, "Influence of defects on mechanical properties of Ti-6Al-4 V components produced by selective laser melting and electron beam melting," *Materials & Design*, vol. 86, pp. 545-554, 2015.

- [53] D. Umbrello, "Finite element simulation of conventional and high speed machining of Ti6Al4V alloy," *Journal of Materials Processing Technology*, vol. 196, no. 1-3, pp. 79-87, 2007.
- [54] K. D. Rekedal and D. Liu, "Fatigue life of selective laser melted and hot isostatically pressed Ti-6Al-4V absent of surface machining," in *AIAA/ASCE/AHS/ASC Structures, Structural Dynamics, and Materials Conference, 56th*, 2015.
- [55] M. Simonelli, Y. Y. Tse and C. Tuck, "Effect of the build orientation on the mechanical properties and fracture modes of SLM Ti-6Al-4V," *Materials Science and Engineering: A*, vol. 616, no. 10, pp. 1-11, 2004.
- [56] N. Hansen, "Hall–Petch relation and boundary strengthening," *Scripta Materialia*, vol. 51, no. 8, pp. 801-806, 2004.
- [57] R. Reda, A. Nofal and A.-H. Hussein, "Effect of Single and Duplex Stage Heat Treatment on the Microstructure and Mechanical Properties of Cast Ti–6Al–4V Alloy," *Metallography, Microstructure, and Analysis*, vol. 2, no. 6, pp. 388-393, 2013.
- [58] Agilent Technologies, Inc, "How to Select the Correct Indenter Tip," 2009.
- [59] X. Li and B. Bhushan, "A review of nanoindentation continuous stiffness measurement technique and its applications," *Materials Characterisation*, vol. 48, no. 1, pp. 11-36, 2002.
- [60] Agilent Technologies, Inc., "Agilent NanoSuite Training Manual," 2009.
- [61] N. Hutasoit, W. Yan and R. Cottam, "Evaluation of microstructure and mechanical properties," *Metallography, Microstructure, and Analysis*, vol. 2, no. 5, pp. 328-336, 2013.
- [62] ASTM International, "Standard Test Methods for Determining Grain Size," in *ASTM Standard E112-88*, West Conshohocken, PA: ASTM International, 2003.
- [63] W. Yan, C. L. Pun and G. P. Simon, "Conditions of applying Oliver–Pharr method to the nanoindentation of particles in composites," *Composites Science and Technology*, vol. 72, no. 10, pp. 1147-1152, 2012.
- [64] E. O. Hall, "The Deformation and Ageing of Mild Steel: III Discussion of Results," *Proceedings of the Physical Society. Section B*, vol. 64, p. 747, 1951.
- [65] N. J. Petch, "The Cleavage Strength of Polycrystals," *Journal of the Iron and Steel Institute*, vol. 174, pp. 25-28, 1953.
- [66] S. Cao, R. Chu, X. Zhou, K. Yang, Q. Jia, C. V. S. Lim, A. Huang and X. Wu, "Role of martensite decomposition in tensile properties of selective laser melted Ti-6Al-4V," *Journal of Alloys and Compounds*, vol. 744, pp. 357-363, 2018.
- [67] I. M. Hutchings, "The contributions of David Tabor to the science of indentation hardness," *Journal of Materials Research*, vol. 24, no. 3, pp. 581-589, 2009.

- [68] H. Ali, H. Ghadbeigi and K. Mumtaz, "Residual stress development in selective laser-melted Ti6Al4V: a parametric thermal modelling approach," *The International Journal of Advanced Manufacturing Technology*, vol. 97, no. 5-8, pp. 2621-2633, 2018.
- [69] L. Qian, M. Li, Z. Zhou, H. Yang and X. Shi, "Comparison of nanoindentation hardness to microhardness," *Surfaces & Coating Technology*, vol. 195, pp. 264-271, 2005.
- [70] X. Wu, J. Liang, J. Mei, C. Mitchell, P. S. Goodwin and W. Voice, "Microstructures of laser-deposited Ti-6Al-4V," *Materials & Design*, vol. 25, no. 2, pp. 137-144, 2004.
- [71] R. Hill, "Elastic properties of reinforced solids: Some theoretical principles," *Journal of the Mechanics and Physics of Solids*, vol. 11, no. 5, pp. 357-372, 1963.
- [72] L. T. Harper, C. Qian, T. A. Turner, S. Li and N. A. Warrior, "Representative volume elements for discontinuous carbon fibre composites – Part 1: Boundary conditions," *Composites Science and Technology*, vol. 72, no. 2, pp. 225-234, 2012.
- [73] L. T. Harper, C. Qian, T. A. Turner, S. Li and N. A. Warrior, "Representative volume elements for discontinuous carbon fibre composites–Part 2: Determining the critical size," *Composites Science and Technology*, vol. 72, no. 2, pp. 204-210, 2012.
- [74] L. Mullen, R. C. Stamp, W. K. Brooks, E. Jones and C. J. Sutcliffe, "Selective laser melting: a regular unit cell approach for the manufacture of porous, titanium, bone in-growth constructs, suitable for orthopedic applications," *Journal of Biomedical Materials Research Part B: Applied Biomaterials*, no. 89B, pp. 325-334, 2008.
- [75] Y.-J. Kim, K. Son, I.-C. Choi, I.-S. Choi, W. I. Park and J.-i. Jang, "Exploring Nanomechanical Behavior of Silicon Nanowires: AFM Bending Versus Nanoindentation," *Advanced Functional Materials*, vol. 21, no. 2, pp. 279-286, 2010.

